Dynamics of beam diagnostics

A. Hofmann
CERN, Geneva, Switzerland

Abstract

The subject of beam dynamics is treated with the emphasis on beam observations and experiments. The electromagnetic fields used for beam observations are discussed. Nearly all instruments are based on the so-called 'near field' which is attached to the particles and is basically just the Lorentz-transformed Coulomb field. The 'far field', or radiation field, is used for diagnostics mostly as synchrotron radiation. Since this application was covered in the CAS in 2003, only a short summary is given here.

For transverse beam dynamics a particle is followed around the ring, this is described by a transport matrix; its position and angle are measured at each revolution. This approach is close to that of some beam experiments. It serves as a base to develop most relations which are important for understanding the transverse beam behaviour and for designing and interpreting measurements. The beam experiments are covered in order of increasing sophistication, starting with static beam conditions, going to oscillations and phase-space observations.

The longitudinal dynamics is based on the relation between deviations in energy and revolution time and the longitudinal focusing provided by the RF system. Dispersion, energy loss, and bunch pattern are the static conditions to be observed. The excitation of synchrotron oscillations opens the way for measurements of chromatic effects and energy calibration.

Many measurements done in storage rings are related to intensity limitations. A review of different instabilities is based on a generalization of the Robinson instability leading to conditions for the impedance at the synchrotron and betatron sidebands and the chromaticity.

As illustrations of the different topics a few measurement examples are given with emphasis on showing raw data before any analysis. Only cases of bunched beams are covered, leaving out special methods used for coasting beams such as transfer functions.

1 Electromagnetic fields used for beam diagnostics

1.1 Introduction

Beam diagnostics is mostly based on the electromagnetic fields $\vec{E}$ and $\vec{B}$ created by charged particles. We distinguish between the 'near field' which is attached to the charges and the 'far field' or radiation field which propagates.

1.1.1 The 'near field'

The near field is a Lorentz-transformed Coulomb field now containing a magnetic component. The electric field of a relativistic point charge is concentrated in the transverse direction and induces on the chamber wall a very localized image charge q'. A bunch $I(t)$ induces therefore a wall current $I_{\mathrm{w}}(t)$ of nearly the same form, Fig. 1. Usually the observed signal is filtered $\omega < \omega_{\text{cut-off}}$ and not sensitive to propagating fields. We therefore measure the beam properties at the location of the monitor.

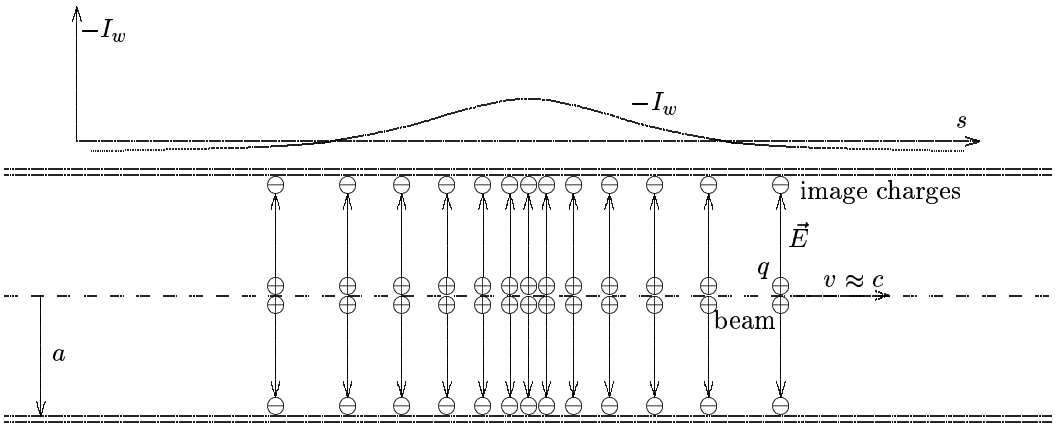

Fig. 1: Charges and current induced by the beam at the wall

1.1.2 The 'far field'

The 'far' or radiation field is created by accelerated charges. Field propagation in a conducting chamber is only possible above the cut-off frequency, which for a circular chamber of radius a is

$$\omega_{\text{cut-off}} \geq \frac{2.405c}{a} \,. \tag{1}$$

The most common such field used for diagnostics is synchrotron radiation, Fig. 2. It is emitted by the particles in a magnet owing to the transverse acceleration, extracted through a window in the vacuum chamber, and observed at some distance by a detector which measures the beam properties at the location of the source.

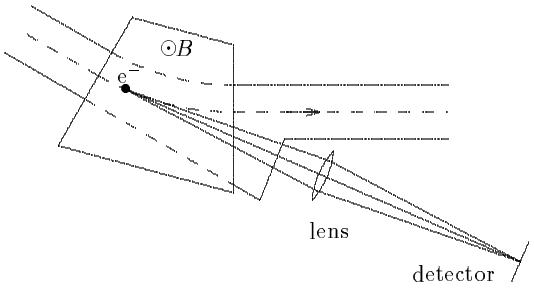

Fig. 2: Imaging beam with synchrotron radiation

1.2 The 'near field'

1.2.1 Properties

The particles of a beam move with relativistic velocity $\vec{v} = \vec{\beta}c$ having $\beta \approx 1$ and the Lorentz factor $\gamma = 1/\sqrt{1-\beta^2} \gg 1$. In this case the electric and magnetic fields $\vec{E}$ and $\vec{B}$ created by a point charge are concentrated within a small angle around the transverse direction and have in free space the form

$$\vec{E} = \frac{q}{4\pi\epsilon_0 r^2\gamma^2}\frac{\vec{r}}{r}\frac{\gamma}{(1-\beta^2\sin^2\theta)^{3/2}} \,, \quad \vec{B} = \frac{[\vec{\beta}\times\vec{E}]}{c}$$

as illustrated in Fig. 3 for a charge in free space.

A beam in an accelerator is in the centre of a conducting vacuum chamber which imposes $\vec{E}_{\|} = 0$ as boundary condition. This determines the field which is relatively complicated [1] and shown in Fig. 4 for a point charge in a circular chamber of radius a.

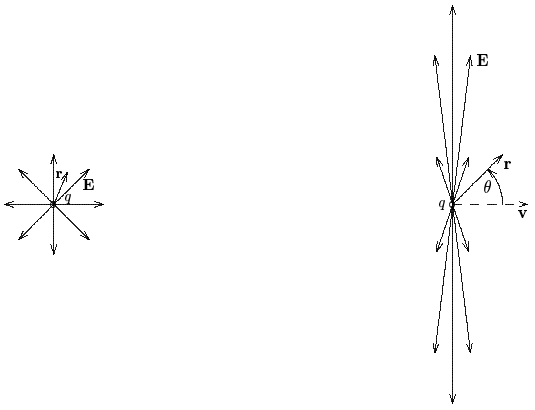

Fig. 3: Electric field of a static and a moving charge ($\gamma = 4$) in free space

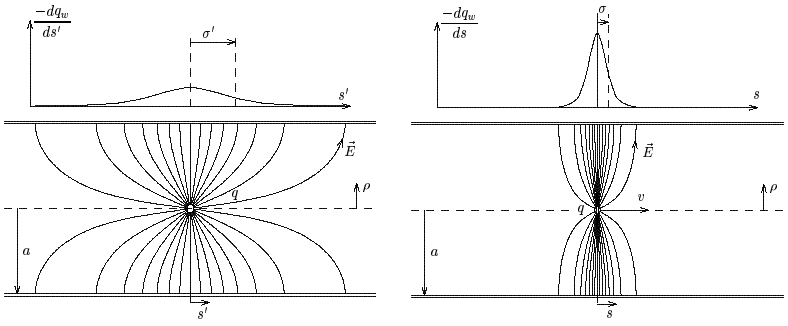

Fig. 4: Electric field of a static and a moving charge ($\gamma = 4$) in a circular cylindrical chamber

Of particular interest for diagnostics is the surface charge density $\sigma' = -\epsilon_0 E_\perp$, induced by the perpendicular field at the vacuum chamber, and after integrating it over the azimuthal direction, the induced charge per unit length $\Lambda'(s) = \mathrm{d}q'/ds = 2\pi a\sigma'$, shown on top of the figure, and a total charge being equal to the original one but of opposite sign $q' = -q$. The longitudinal distribution $\Lambda'(s)$ of the induced charge is complicated and given by a Fourier–Bessel series, but its RMS value σ_s has a simple form [2, 3]

$$\sigma_s = \frac{a}{\sqrt{2}\gamma} \, .$$

A beam containing many distributed particles of charge q represents a line charge density $\Lambda(s)$. Each of these particles induces a surface charge $-q$ on the wall resulting in an induced line charge density $\Lambda'(s)$ on the wall. For $\gamma \gg 1$ the length σ' is small and the induced charge distribution relates to the particle distribution by $\Lambda'(s) \approx -\Lambda(s)$.

The particles in the beam move with velocity $v = \beta c$ and represent a beam current $I = \Lambda\beta c$. The corresponding induced current I_w is not simply equal to $-I$ but does not contain the average beam current. For a completely uniform beam the perpendicular field $E_\perp$ is constant and therefore also the induced surface charge density $\sigma' = -\epsilon_0 E_\perp$ which does not have to move to satisfy the boundary condition $E_\parallel = 0$. Only a longitudinal variation of the line charge density and not its average value produces a wall current. As a result we have

$$I_\mathrm{w}(t) = -(I(t) - \langle I \rangle)$$

as shown in Fig. 1.

1.2.2 Application

Charges and currents induced on the wall by the 'near field' of the beam are used by monitors to measure its current $I(t)$ or its dipole moments $Ix(t)$.

– Button monitor, Fig. 5: It is used mainly for short bunches in electron machines. To avoid electron emission by synchrotron radiation photons in the median plane, the buttons are placed at $\pm 45°$. Adding and subtracting the signals of each button gives the total current I and its two dipole moments Ix and Iy.

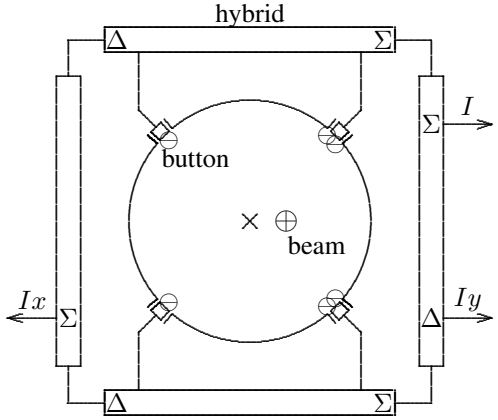

Fig. 5: Button monitor

– Loop monitor, Fig. 6: The magnetic field of the beam induces a voltage in the loop. If the strips forming the loop are wide, there is also a surface charge induced by the electric field. The coupling to the beam is inductive for a thin loop and capacitive for a wide one. With the two balanced it is called 'strip line monitor'.

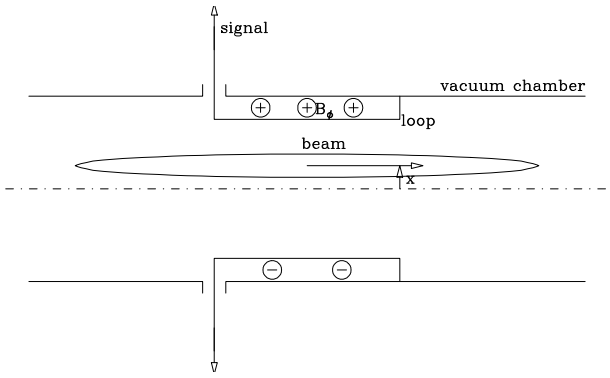

Fig. 6: Loop monitor

– Cavity monitor, Fig. 7: A cavity gets excited by a passing bunch and oscillates. It can be used to measure the beam with high sensitivity. The cavity can have a monopole resonance ($m = 0$), shown on the left, which is not sensitive to the transverse position of the exciting bunch. A dipole resonance ($m = 1$), shown on the right, will be excited proportionally to the dipole moment Iy and can give transverse beam position information.

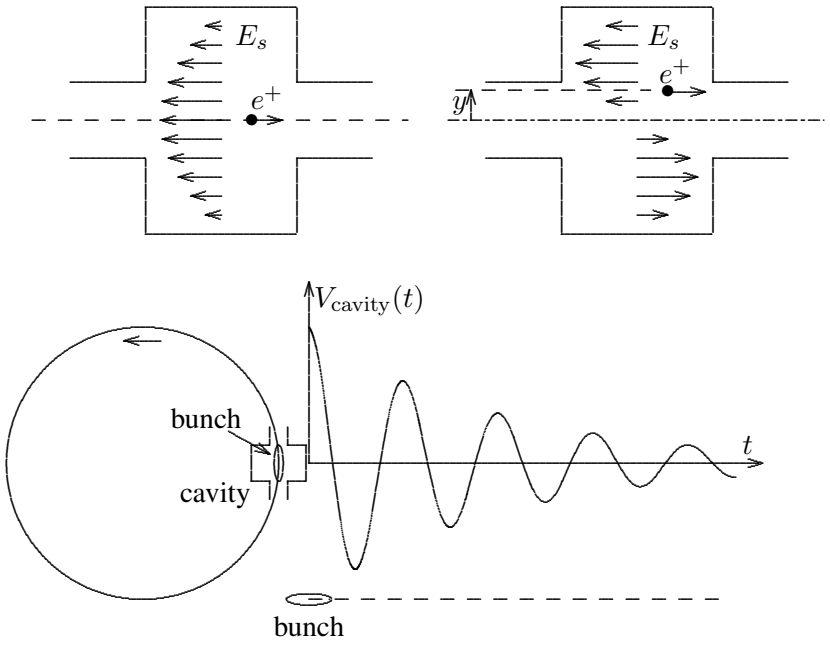

Fig. 7: Cavity monitor

1.2.3 Measure average current

The beam-induced wall current does not contain the DC part. However, it can be estimated from the monitor reading between the widely spaced bunches shown in Fig. 8.

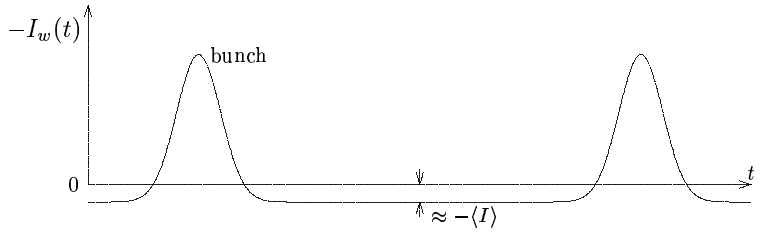

Fig. 8: Getting average current from monitor reading between widely spaced bunches

The magnetic field created by the DC part of the beam penetrates the chamber wall and can be observed outside, Fig. 9.

1.2.4 Protection of monitors from the radiation field

We assumed that monitors use the near field. Synchrotron radiation emitted in upstream magnets and diffraction radiation created at an aperture change can reach a monitor, Fig. 10. They can only propagate inside a conducting chamber for frequencies above $\omega_{\text{cut-off}}$, which are usually filtered out from the monitor signals and should not influence the measurement.

1.3 Bandwidth and readout

The information we can obtain from an intensity or position monitor depends on its bandwidth and that of the signal processing as illustrated in Fig. 11.

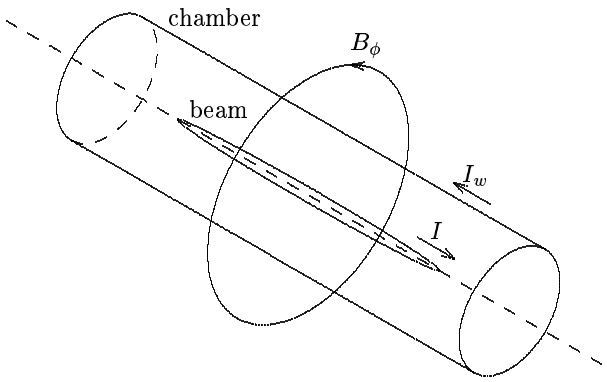

Fig. 9: Getting average current from the magnetic field

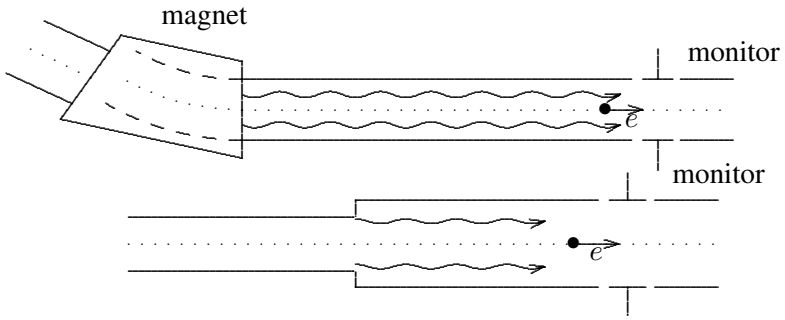

Fig. 10: Synchrotron or diffraction radiation might reach a monitor

1.4 Instruments

1.4.1 Oscilloscopes

An oscilloscope, often just called 'scope', displays the signal $I(t)$ from an intensity monitor, or $yI(t)$ from a position monitor directly as a function of time either from a single or multiple traversal: the time scale is chosen by the sweep speed. To observe a slow development of a fast signal one displaces the vertical position of the horizontal trace either after every sweep or after several sweeps. This so-called mountain-range display allows one, to see the details of a bunch form on a fast scale t and its development on a slower scale T. This will be shown later as an example of an instability measurement (Fig. 84).

1.4.2 Fourier transform — spectrum and network analysers

Since in circular storage rings the particles rotate with a certain revolution frequency ω_0, many beam signals are quasi-periodic and observing them in frequency domain helps to understand them.

– The Fourier Transform converts a signal $f(t)$ given as a function of time t into a signal $F(\omega)$ given in frequency ω:

$$F(\omega) = \mathcal{F}[f(t)] = \frac{1}{\sqrt{2\pi}} \int_{-\infty}^{\infty} f(t) \mathrm{e}^{-i\omega t} \mathrm{d}t$$
$$= \frac{1}{\sqrt{2\pi}} \int f(t) \left[\cos(\omega t) - i \sin(\omega t)\right] \mathrm{d}t = F_\mathrm{r}(\omega) + iF_\mathrm{i}(\omega) \; .$$

The cosine and sine transforms F_r and F_i, called also real and imaginary part or resistive and reactive part, can also be expressed as an amplitude A and phase ϕ with

$$A^2(\omega) = |F_\mathrm{r}(\omega)|^2 + |F_\mathrm{i}(\omega)|^2 \; , \;\; \tan\phi = \frac{F_\mathrm{i}(\omega)}{F_\mathrm{r}(\omega)} \; .$$

Intensity monitors, readout and signal processor have limited bandwidth. They integrate/differentiate or distort the signals and might only give $I_b = \langle I(t) \rangle$, but over limited bandwidth the original signal $I(t)$ may be restored.

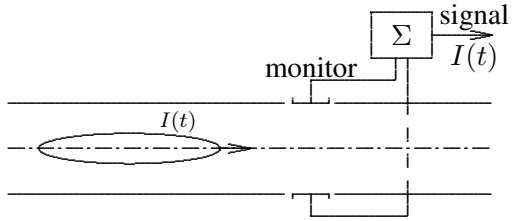

A position monitor with low bandwidth measures just the average dipole moment of the bunch $y_b I_b = \langle y(t) I(t) \rangle$.

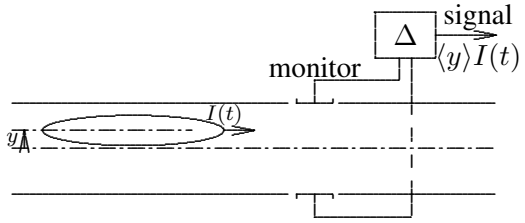

For larger bandwidth the bunch length can be resolved $y_b I_b(t)$, and for long bunches or a very large bandwidth the position variation along the bunch can also be observed (head–tail modes).

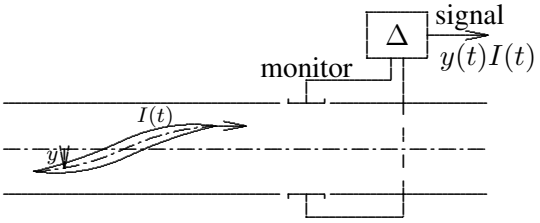

Fig. 11: Information from monitors for different bandwidths

The amplitude square A^2 is proportional to the power spectrum.
The inverse transform is

$$f(t) = \mathcal{F}^{-1}[F(\omega)] = \frac{1}{\sqrt{2\pi}} \int_{-\infty}^{\infty} F(\omega) \mathrm{e}^{i\omega t} \mathrm{d}\omega \; .$$

Periodic functions are developed in a series:

$$f(t) = a_0 + 2 \sum_{1}^{\infty} \left(a_p \cos(p\omega_0 t) + b_p \sin(p\omega_0 t) \right)$$

$$a_p = \frac{1}{T_0} \int_0^{T_0} f(t) \cos(p\omega_0 t) \mathrm{d}t \; , \quad b_p = \frac{1}{T_0} \int_0^{T_0} f(t) \sin(p\omega_0 t) \mathrm{d}t \; .$$

– A spectrum analyser Fourier-transforms a time signal $f(t)$ but with a limited integration range and without phase information since no absolute time is involved, Fig. 12. It gives in effect the power spectrum of a signal. Most analysers use a swept frequency, i.e., at any moment only one frequency with finite bandwidth $\delta\omega$ is measured. The sweep speed is limited by the desired frequency resolution. Some spectrum analysers store the signal $f(t)$ over a certain time span and make a Fast Fourier Transform (FFT) while the next time sample is arriving and a certain spectral range of interest is observed all the time.
– Network analysers measure the beam response in amplitude A and phase ϕ, or in real $F_\mathrm{r}(\omega)$ and imaginary $F_\mathrm{i}(\omega)$ part, to a harmonic excitation, called **transfer function**, Fig. 13. Most use a swept frequency, some have a double channel FFT analyser with noise excitation. It can also compare amplitude and phase response of two monitors to a beam excitation giving relative beta functions and phases (Fig. 42). Spectrum analysers often provide the sweeping frequency signal as output, called tracking generator. It can give the amplitude part of a transfer function.

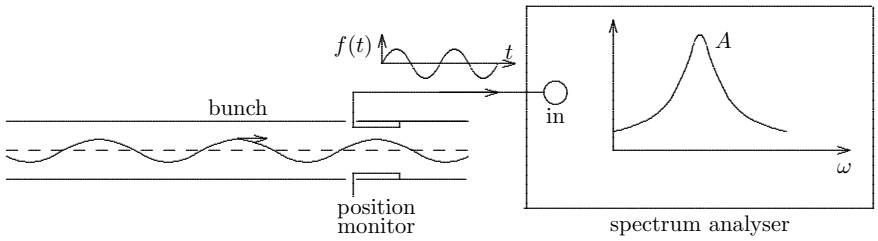

Fig. 12: Spectrum analyser

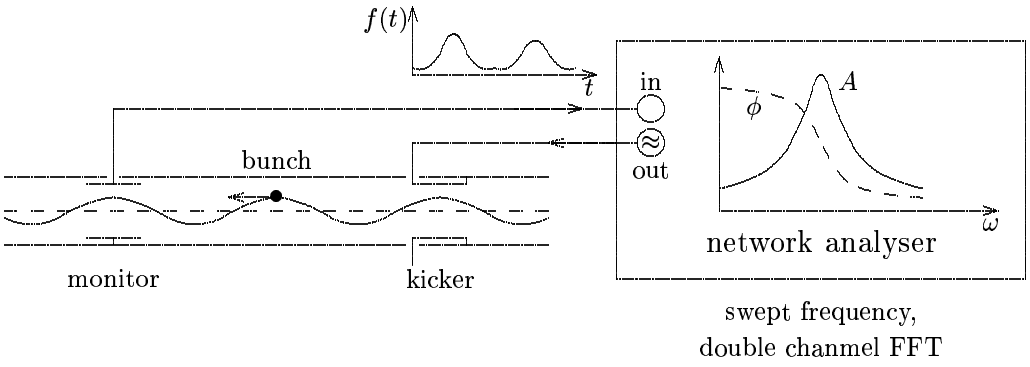

Fig. 13: Network analyser

– Digital signal processing provides many tools to obtain sophisticated information from the measured data [4]. The control system of an accelerator can store all the measured data, manipulate them, and deduce the relevant results.

1.5 Active elements

1.5.1 Deflectors

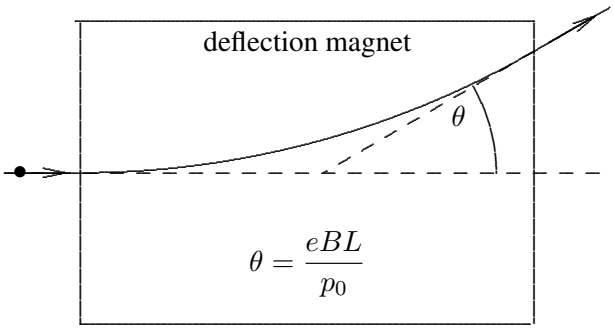

Fig. 14: Deflector

Storage rings have many deflecting magnets for orbit correction which can also be used for beam measurements, Fig. 14. Depending on the type of deflector, different measurements can be done.

– Slow deflection is provided by the corrector magnets and gives an adiabatic change of the closed orbit. It can be used to measure lattice functions.
– Fast deflection is provided by the injection kickers and other special devices. If the rise time is comparable to the revolution time, betatron oscillation can be excited. These devices can be driven by a pulse or a harmonic excitation.

– Feed-back systems damp betatron oscillations. They can also be used to excite modes of oscillations in a controlled manner to measure beam stability.

1.5.2 Changing machine parameters

– Quadrupole strength: The close orbit, tunes, beta functions and phase advance can be modified by changing a single or a group of quadrupoles. This can be used to determine the orbit distance from the quadrupole axis and to measure the local beta function.
– Sextupole strength: Changing the sextupoles varies the chromaticity and affects the transverse beam stability. It also changes the tunes if the beam is not centred.
– Bending magnets: A change of the dipole magnets changes the energy of the bunches while the focusing is still set for the original energy. The tune change gives in this case the natural chromaticity.
– RF system: An RF frequency variation changes the energy. Observing the orbit and the tunes at the same time gives the dispersion and the corrected chromaticity. Modulating the RF voltage can excite dipole and quadrupole mode synchrotron oscillations.

1.6 The 'far field' — synchrotron radiation

The 'far field' is a radiation field which transports energy. For beam diagnostics we use nearly exclusively synchrotron radiation emitted by relativistic electrons undergoing a transverse acceleration in a deflecting magnet. This radiation is characterized by its small opening angle of order $1/\gamma$. The measurements carried out with this radiation give the particle beam properties at the location of emission. Since the topic of this kind of beam diagnostics was treated in an earlier CAS [5], we give only a short summary here.

We distinguish three types of measurements with synchrotron radiation:

– Imaging the beam cross-section: The radiation emitted in a deflecting magnet is focused by a lens giving an image of the particle beam cross-section, Fig.15. The small opening angle of the radiation makes its extraction from the vacuum chamber easy. However, it also makes diffraction effects important and limits the resolution of the beam dimension measurement.

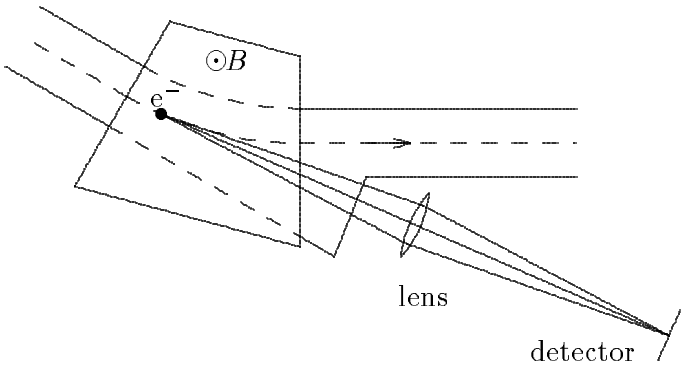

Fig. 15: Imaging beam with synchrotron radiation

– Angular particle distribution from a direct synchrotron radiation observation: The synchrotron radiation is emitted mainly in the direction of the particle velocity with a small opening angle of order $1/\gamma$. This allows one to obtain the angular distribution of the particles (Fig.16). The accuracy of this measurement is limited by the finite opening angle of the radiation.

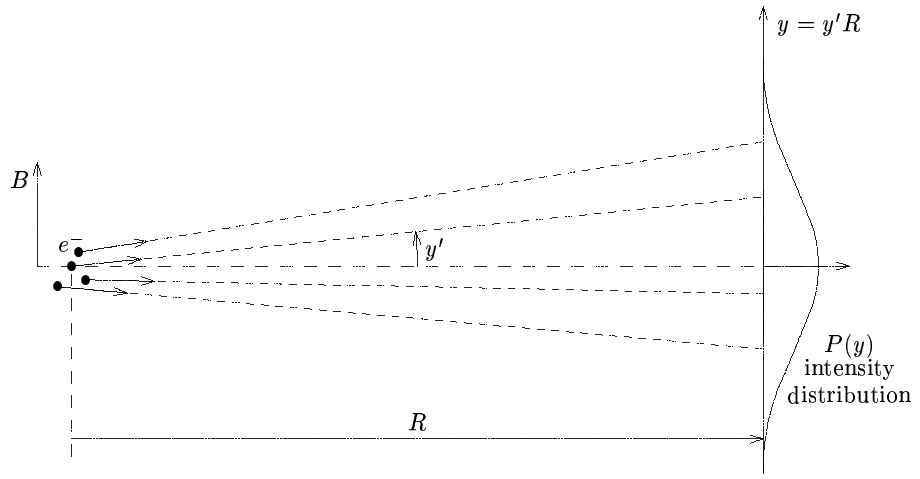

Fig. 16: Direct observation of synchrotron radiation

– Time structure of synchrotron radiation and particles: Since the synchrotron radiation emitted by a single particle consists of a very short light pulse, we obtain from a measurement of the time structure information about the longitudinal particle distribution in the beam, in particular the bunch length, Fig. 17.

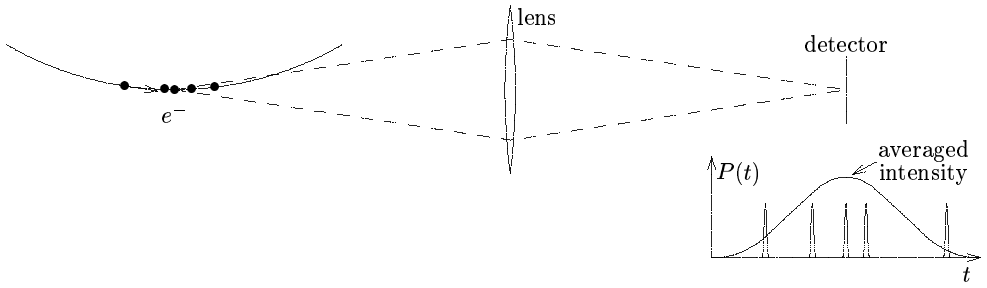

Fig. 17: Time structure of particles and synchrotron radiation

Synchrotron radiation has an effect on the electron beam. The energy loss due to the emission of synchrotron radiation is replaced by the RF system. This leads to damping of betatron and synchrotron oscillations. The radiation is emitted in energy quanta of $\epsilon_\gamma = \hbar\omega$, involving Planck's number divided by 2π and the radiation frequency. This noise excitation of betatron and synchrotron oscillations, together with the radiation damping, results in finite horizontal and vertical beam dimensions and an energy spread with Gaussian distributions of RMS values σ_x, σ_y, σ_E.

2 Transverse beam dynamics

2.1 Storage rings

– A storage has bending dipole and focusing quadrupole magnets, arranged in a lattice, which defines a nominal equilibrium orbit as shown in Fig. 18. A particle launched with nominal position, angle, and momentum p circulates on this orbit with revolution frequency ω_0. Particles with spatial or angular deviations x/y and x'/y' are focused by the quadrupoles and execute betatron oscillations around the closed orbit. Their maximum amplitude is a measure of the local focusing strength, given by the so-called beta functions $\beta_{x/y}$. The number of betatron oscillations per revolution $Q_{x/y}$, called tunes, measures the global focusing strength.

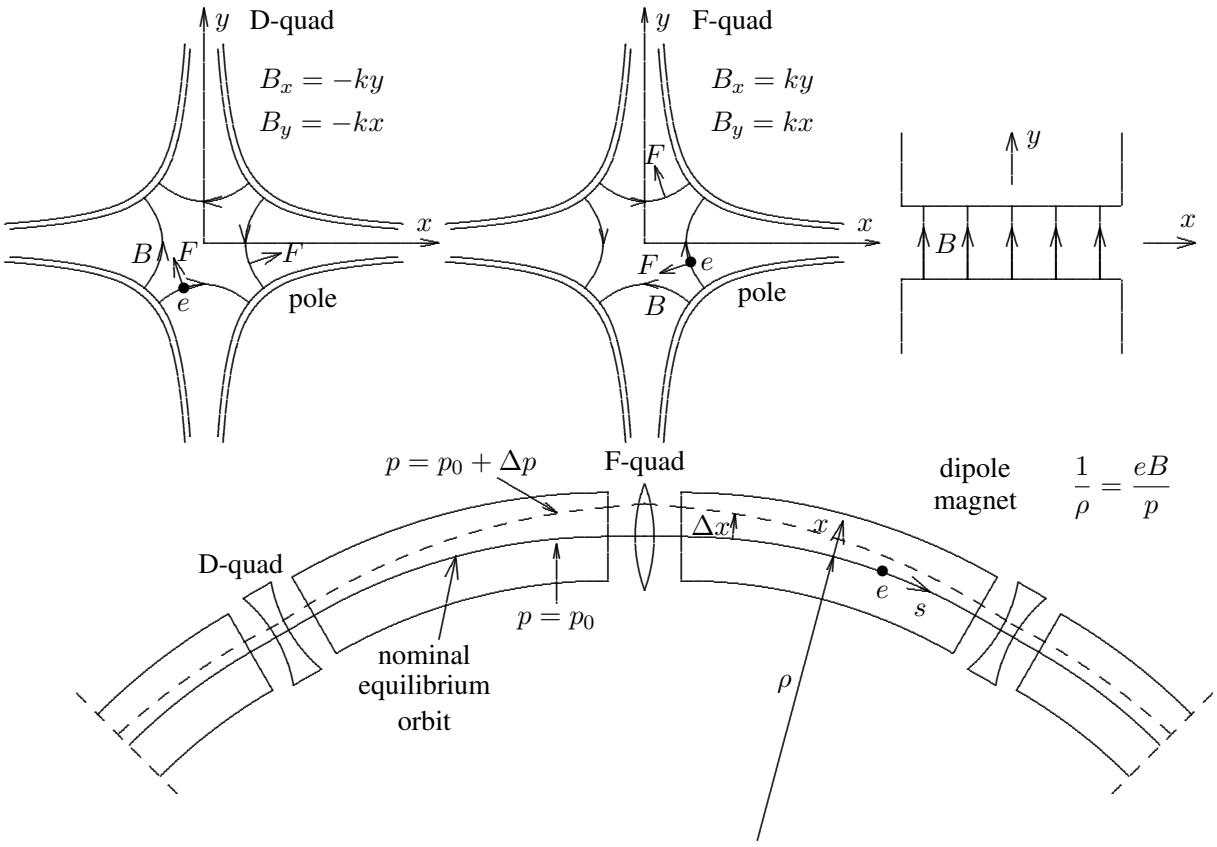

Fig. 18: Storage ring and its elements

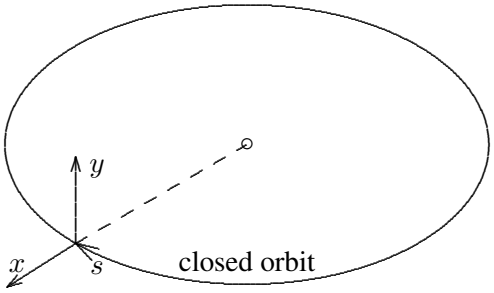

Fig. 19: Coordinates

- The beam dynamics in a storage ring is usually described in a coordinate system which follows the central equilibrium orbit, Fig. 19. The longitudinal coordinate s is the path length along this orbit. As transverse coordinates, x is used in the horizontal direction pointing to the outside of the ring and y for the vertical direction pointing upward.
  The derivatives with respect to s are indicated with a 'prime', e.g., the vertical angle of the trajectory is y'. Sometimes also the change with respect to relative momentum is indicated in the same way, e.g., $Q'_{x/y} = \Delta Q_{x/y}/(\mathrm{d}\Delta p/p)$.
- Particles with momentum deviation Δp are bent differently by the dipoles and have a different equilibrium orbit, displaced from the nominal one by $\Delta x = D_x \Delta p/p$ where D_x is called the dispersion. This off-energy orbit has a different circumference C_b which deviates from that of the nominal orbit by $\Delta C/C_c = \alpha_c \Delta p/p$ with α_c being called momentum compaction. Related to this is the relative change of revolution frequency $\Delta\omega_0/\omega_0 = -(\alpha_c - 1/\gamma^2)(\Delta p/p) = -\eta_c(\Delta p/p)$.

– A storage ring has RF cavities oscillating with a frequency $\omega_{\rm RF} = h\omega_0$, being a harmonic h of the revolution frequency, and a voltage $V_{\rm RF}$ providing a longitudinal field to a particle. This RF voltage replaces on average the energy lost due to synchrotron radiation, and through its dependence on arrival time, provides longitudinal focusing which collects the particles in bunches.
– The change of global focusing due to a momentum deviation is called chromaticity defined as the related tune change $Q'_{x/y} = \Delta Q_{x/y}/(\Delta p/p)$.
– We assume small relative deviations and consider in most cases linear terms only. Furthermore, we make ultra-relativistic approximations

$$\frac{x}{\rho} \ll 1\,,\quad x' = \frac{{\rm d}x}{{\rm d}s} \ll 1 \;\text{ and }\; \frac{y}{\rho} \ll 1\,,\quad y' = \frac{{\rm d}y}{{\rm d}s} \ll 1,\; \text{as well as } \frac{\Delta p}{p} \ll 1\,,$$
$$\gamma = \frac{1}{\sqrt{1-\beta^2}} = \frac{E}{m_0c^2} \gg 1\,,\quad \beta \approx 1\,,\quad \frac{\Delta p}{p} = \frac{1}{\beta^2}\frac{\Delta E}{E} \approx \frac{\Delta E}{E}\,.$$

Where horizontal and vertical motions are equivalent, we give in the following only one of the two dimensions.

2.2 Optical elements

2.2.1 Straight section

It is impossible to get a simple closed expression for a general trajectory in a storage ring with many elements. However, we can get this for individual elements. Combining these leads to a matrix expression which gives position and angle of a particle after one turn from its initial values.

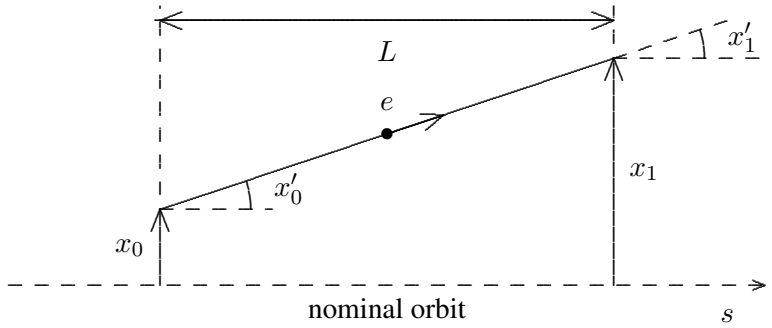

Fig. 20: Straight section – drift space

A straight section, often also called drift space, has a length L and contains no deflecting or focusing elements. The trajectory position and angle (x_1, x'_1) at the end are simply obtained from the initial values (x_0, x'_0) by

$$\begin{array}{rcccl} x_1 & = & x_0 & + & Lx'_0 \\ x'_1 & = & & & x'_0 \end{array} \text{ or in matrix form } \begin{pmatrix} x_1 \\ x'_1 \end{pmatrix} = \begin{pmatrix} 1 & L \\ 0 & 1 \end{pmatrix} \begin{pmatrix} x_0 \\ x'_0 \end{pmatrix}$$

as is evident from Fig. 20. The optical behaviour of a straight section can be described by the transport matrix M.

$$M = \begin{pmatrix} m_{11} & m_{12} \\ m_{21} & m_{22} \end{pmatrix} = \begin{pmatrix} 1 & L \\ 0 & 1 \end{pmatrix}$$

We have such a matrix for the horizontal and vertical plane. In the case of a straight section the two are the same $M_x = M_y$.

2.2.2 Dipole bending magnet

This magnet has a homogeneous magnetic field $\vec{B} = [0,\, B_y,\, 0]$ being perpendicular to the median plane which contains the nominal orbit. It applies a Lorentz force $\vec{F}$ on a particle moving with velocity $\vec{v} = \vec{\beta}c = [\dot{x},\, 0,\, \dot{z}]$ in this plane resulting in a curvature $1/\rho$ of its trajectory:

$$F_v = e[\vec{v} \times \vec{B}] = eB_y[-\dot{z},\, 0, \dot{x}]\ ,\quad \frac{1}{\rho} = \frac{eB_y}{p} = \frac{eB_y}{m_0\gamma\beta c}\ .$$

This force of the dipole magnet determines the closed orbit. Since we describe the particle trajectory with respect to this, the dipole magnet often appears only as a drift of length L in the transverse dynamics calculations. However, this is no longer the case if we consider particles with a momentum deviation Δp which have a different curvature in this magnet. Furthermore, there is so-called edge focusing, caused at the magnetic end fields which we neglect here.

Apart from this dipole magnet there exist magnets having a dipole and a quadrupole component, called combined function magnets, which provide bending and focusing. We shall also not consider them here.

2.2.3 Quadrupole magnet

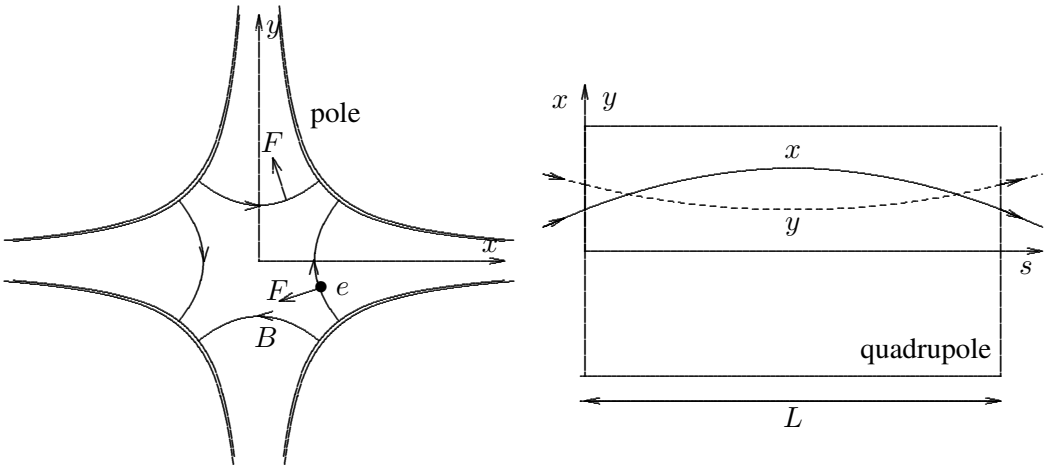

Fig. 21: Quadrupole magnet with its trajectory

The focusing in a storage ring is provided by quadrupole magnets, often called just quads, shown in Fig. 21. They have a field perpendicular to the nominal particle trajectory with linear gradients in the x and y direction of the form

$$\vec{B} = \vec{B}(x,\, y) = [B_x,\, B_y,\, 0]\ ,\quad \mathrm{curl}\,\vec{B} = \left[0,\, 0,\, \frac{\partial B_y}{\partial x} - \frac{\partial B_x}{\partial y}\right] = 0$$

$$B_x = \frac{\partial B_x}{\partial y}y = ky\ ,\quad B_y = \frac{\partial B_y}{\partial x}x = kx\ ,\quad B^2 = k^2(x^2+y^2)\ ,\quad k = \frac{\partial B_x}{\partial y} = \frac{\partial B_y}{\partial x}\ .$$

The Lorentz force on the particle is

$$\vec{F} = e[\vec{v} \times \vec{B}] = e[-\dot{z}B_y,\, \dot{z}B_x,\, \dot{x}B_y - \dot{y}B_x]\ .$$

We make the paraxial approximation assuming transverse velocities much smaller than the longitudinal one

$$x' = \frac{\dot{x}}{\dot{z}} \approx \frac{\dot{x}}{\beta c} \ll 1\ ,\quad y' = \frac{\dot{y}}{\dot{z}} \approx \frac{\dot{y}}{\beta c} \ll 1\ ,$$

and neglect the z component of the force, giving

$$\vec{F} = m_0\gamma[\ddot{x},\, \ddot{y}] = e\beta c[-B_y,\, B_x] = e\beta ck[-x,\, y]\ .$$

We use $\ddot{x} = \beta^2c^2x''$ and the momentum $p = m_0\gamma\beta c$ and get the two differential equations

$$x'' = -\frac{ek}{m_0\gamma\beta c}x = \frac{ek}{p}x = -Kx\ ,\quad y'' = Ky\ .$$

Here we introduced the focusing parameter K which has the dimension m^{-2}:

$$K = \frac{e}{p}\frac{\partial B_y}{\partial x} = \frac{e}{p}\frac{\partial B_x}{\partial y} = \frac{ek}{p}\ .$$

Its sign definition is not uniform in the literature. We have now the differential equations and their solutions in the focusing horizontal and defocusing vertical plane, Fig. 21.

$$\begin{aligned} x'' + Kx = 0\ ,&\quad x = A\cos(\sqrt{|K|}s) + B\sin(\sqrt{|K|}s)\ ,\\ y'' - Ky = 0\ ,&\quad y = C\cosh(\sqrt{|K|}s) + D\sinh(\sqrt{|K|}s)\ . \end{aligned}$$

At the entrance $s = 0$ we have $x(0) = x_0 = A,\quad x'(0) = x_0' = B\sqrt{|K|}$ which can be used to express the integration constants. Of particular interest are the exit parameters of the trajectory at the end of the quadrupole of length L as a function of the input values

$$\begin{aligned} x_1 = x(L) &= x_0\cos(\sqrt{|K|}L) + \frac{x_0'}{\sqrt{|K|}}\sin(\sqrt{|K|}L)\\ x_1' = x'(L) &= -x_0\sqrt{|K|}\sin(\sqrt{|K|}L) + x_0'\cos(\sqrt{|K|}L) \end{aligned}$$

$$\begin{aligned} y_1 = y(L) &= y_0\cosh(\sqrt{|K|}L) + \frac{y_0'}{\sqrt{|K|}}\sinh(\sqrt{|K|}L)\\ y_1' = y(L) &= y_0\sqrt{|K|}\sinh(\sqrt{|K|}L) + y_0'\cosh(\sqrt{|K|}L) \end{aligned}$$

giving the transport matrices

$$M_x = \begin{pmatrix} \cos(\sqrt{|K|}L) & \frac{1}{\sqrt{|K|}}\sin(\sqrt{|K|}L)\\ -\sqrt{|K|}\sin(\sqrt{|K|}L) & \cos(\sqrt{|K|}L) \end{pmatrix}$$

$$M_y = \begin{pmatrix} \cosh(\sqrt{|K|}L) & \frac{1}{\sqrt{|K|}}\sinh(\sqrt{|K|}L)\\ \sqrt{|K|}\sinh(\sqrt{|K|}L) & \cosh(\sqrt{|K|}L) \end{pmatrix}\ .$$

2.2.4 Short lens

A quadrupole magnet with focusing parameter K and length L is often approximated by a short lens of vanishing length and focal strength $1/f = KL$, Fig. 22.

2.3 Transfer matrices

Each of the discussed optical elements can be described by a matrix having some general common properties:

$$M = \begin{pmatrix} m_{11} & m_{12}\\ m_{21} & m_{22} \end{pmatrix}\ .$$

$$x_1 = x_0\ ,\quad x_1' = -x_0\frac{1}{|f|} + x_0'$$
$$y_1 = y_0\ ,\quad y_1' = y_0\frac{1}{|f|} + y_0'$$
$$M_x = \begin{pmatrix} 1 & 0 \\ -1/|f| & 1 \end{pmatrix}\ ,\quad M_y = \begin{pmatrix} 1 & 0 \\ 1/|f| & 1 \end{pmatrix}$$

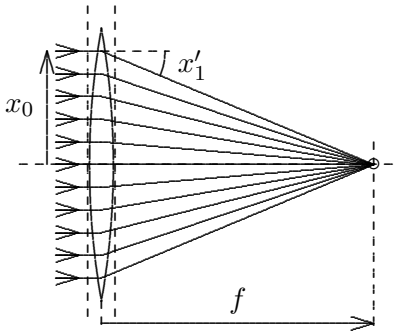

Fig. 22: Short lens; transport equations and matrices

- The determinant is unity $|M| = m_{11}m_{22} - m_{12}m_{21} = 1$, which indicates that the particle does not gain or lose energy.
- The element m_{12} gives an indication for the element length.
- The element m_{21} gives the dependence of the deflection on the initial displacement which is characteristic for focusing: $m_{21} > 0 \rightarrow$ defocusing, $m_{21} < 0 \rightarrow$ focusing.

Going from s_0 to s_1 is described by the matrix M

$$\begin{array}{rcl} x_1 &=& m_{11}x_0 + m_{12}x_0' \\ x_1' &=& m_{21}x_0 + m_{22}x_0' \end{array} \rightarrow \begin{pmatrix} x_1 \\ x_1' \end{pmatrix} = \begin{pmatrix} m_{11} & m_{12} \\ m_{21} & m_{22} \end{pmatrix} \begin{pmatrix} x_0 \\ x_0' \end{pmatrix}$$

and going back from s_1 to s_0 by the inverse matrix

$$\begin{array}{rcl} x_0 &=& m_{22}x_1 - m_{12}x_1' \\ x_0' &=& -m_{21}x_1 + m_{11}x_1' \end{array} \rightarrow \begin{pmatrix} x_0 \\ x_0' \end{pmatrix} = \begin{pmatrix} m_{22} & -m_{12} \\ -m_{21} & m_{11} \end{pmatrix} \begin{pmatrix} x_1 \\ x_1' \end{pmatrix}$$

$$\begin{pmatrix} x_0 \\ x_0' \end{pmatrix} = M^{-1} \begin{pmatrix} x_1 \\ x_1' \end{pmatrix}\ .$$

2.4 Combining elements

2.4.1 Matrix multiplication

Going first through element M and then through element N having the transfers

$$\begin{array}{rcl} x_1 &=& m_{11}x_0 + m_{12}x_0' \\ x_1' &=& m_{21}x_0 + m_{22}x_0' \end{array} \qquad \begin{array}{rcl} x_2 &=& n_{11}x_1 + n_{12}x_1' \\ x_2' &=& n_{21}x_1 + n_{22}x_1' \end{array}$$

gives the total transfer through both elements

$$\begin{array}{rcl} x_2 &=& (n_{11}m_{11} + n_{12}m_{21})x_0 + (n_{11}m_{12} + n_{12}m_{22})x_0' \\ x_2' &=& (n_{21}m_{11} + n_{22}m_{21})x_0 + (n_{21}m_{12} + n_{22}m_{22})x_0'\ . \end{array}$$

This is the same as a transfer with a total matrix being the product of the two matrices in *inverse* order and having also unit determinant

$$\begin{pmatrix} x_2 \\ x_2' \end{pmatrix} = (N \cdot M) \begin{pmatrix} x_0 \\ x_0' \end{pmatrix} = \left(\begin{pmatrix} n_{11} & n_{12} \\ n_{21} & n_{22} \end{pmatrix} \cdot \begin{pmatrix} m_{11} & m_{12} \\ m_{21} & m_{22} \end{pmatrix} \right) \begin{pmatrix} x_0 \\ x_0' \end{pmatrix}\ .$$

2.4.2 FODO lattice cell

We take a simple storage ring lattice with equidistant F and D quads of equal absolute strength with bending magnets in between, neglecting edge focusing, Fig. 23.

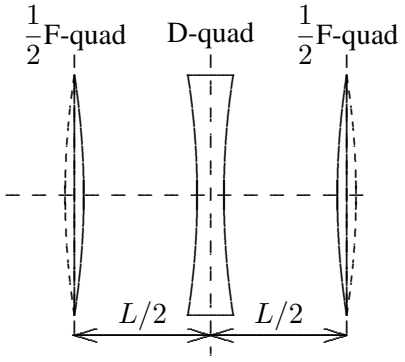

Fig. 23: FODO lattice consisting of F and D quads of equal strength and spacing

$$M_x = \begin{pmatrix} 1 & 0 \\ -\frac{1}{2f} & 1 \end{pmatrix} \begin{pmatrix} 1 & \frac{L}{2} \\ 0 & 1 \end{pmatrix} \begin{pmatrix} 1 & 0 \\ \frac{1}{f} & 1 \end{pmatrix} \begin{pmatrix} 1 & \frac{L}{2} \\ 0 & 1 \end{pmatrix} \begin{pmatrix} 1 & 0 \\ -\frac{1}{2f} & 1 \end{pmatrix}$$
$$= \begin{pmatrix} 1-\frac{L^2}{8f^2} & L\left(1+\frac{L}{4f}\right) \\ -\frac{L}{4f^2}\left(1-\frac{L}{4f}\right) & 1-\frac{L^2}{8f^2} \end{pmatrix} = \begin{pmatrix} \cos\mu_c & \beta_x \sin\mu_c \\ -\frac{1}{\beta_x}\sin\mu_c & \cos\mu_c \end{pmatrix} . \qquad (2)$$

Here we made a formal substitution

$$1-\frac{L^2}{8f^2} = \cos\mu_c = 1-2\sin^2(\mu_c/2)\ , \quad \frac{L}{4f} = \sin(\mu_c/2)\ , \quad L\frac{1+\sin(\mu_c/2)}{\sin\mu_c} = \beta_x,$$

where β_x is a scaling factor between angle and displacement at the entrance of the cell and μ_c is the phase advance of the particle motion across this cell to be discussed later.

2.5 Position and angle measurement of a single particle each turn

We consider a storage ring consisting of a number of cells in which a single particle circulates and measure its position x_k and angle x'_k each turn k. This is shown in Fig. 24 where we use a ring having a FODO lattice consisting of six cells.

We select different positions along the ring to observe the spatial and angular deviations x_k, x'_k of the particle each turn k. Since the focusing is linear the measured points lie on an ellipse in this (x, x') phase-space. At any location the area A of these ellipses is the same (Liouville's theorem) but its shape can be different. In the centre of an F quad the spatial excursions x_k are large but the angles x'_k small giving an ellipse with large horizontal/vertical aspect ratio. In a D quad the situation is reversed with an ellipse being narrow and high. In between quads the ellipse is tilted. After an F quad the trajectories of different turns are convergent, the ellipse is tilted with a negative correlation between spatial and angular deviations. After a D quad we have divergence with a positive correlation between the two deviations.

We also plot on the top of the figure the beam position against the turn number k and connect the points with a harmonic fit $x_k = \hat{x}\cos(n \pm k\mu_x + \phi)$ where $\mu_x = 2\pi Q_x$ is the betatron phase per turn and n a fitting integer. Comparing such measurements done at two locations gives the phase advance

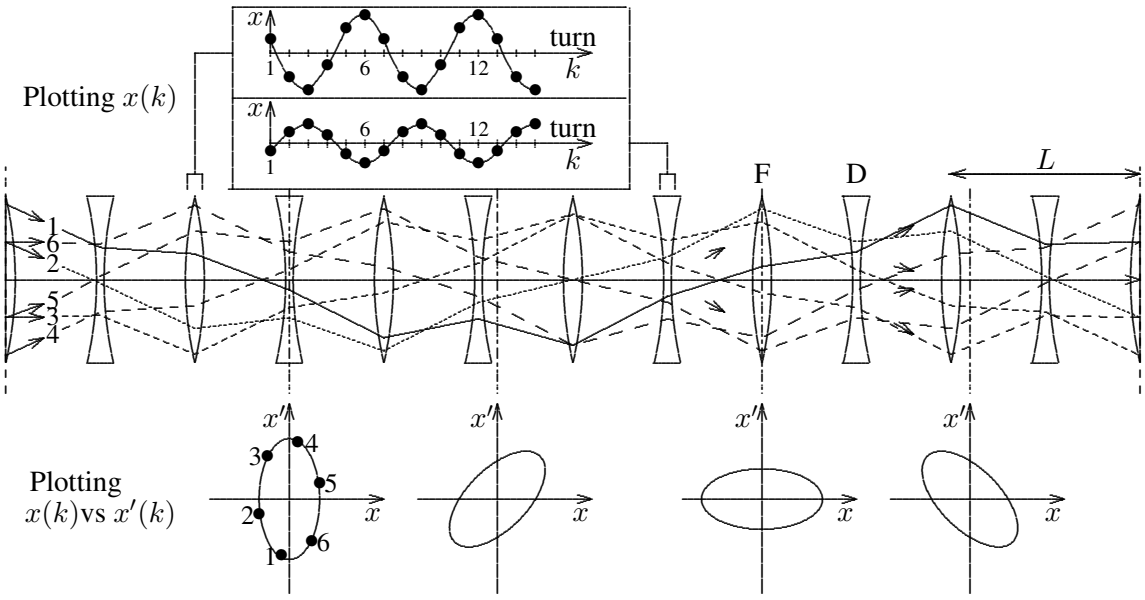

Fig. 24: Measuring position and angle of a particle during successive turns

between these points. Later on we shall describe turn-by-turn measurements done with bunches instead of with single particles.

2.6 The one-turn matrix

Starting at a given ring location and taking all the elements by multiplying their matrices in reverse order gives the one-turn matrix M. From the initial x_0, x_0' we get the values x_1, x_1' after one turn

$$\begin{array}{rcl} x_1 &=& m_{11}x_0 + m_{12}x_0' \\ x_1' &=& m_{21}x_0 + m_{22}x_0' \end{array} \rightarrow \begin{pmatrix} x_1 \\ x_1' \end{pmatrix} = \begin{pmatrix} m_{11} & m_{12} \\ m_{21} & m_{22} \end{pmatrix} \begin{pmatrix} x_0 \\ x_0' \end{pmatrix}$$

and, by matrix multiplications, the values (x_k, x_k') after k turns

$$\begin{pmatrix} x_1 \\ x_1' \end{pmatrix} = \begin{pmatrix} m_{11} & m_{12} \\ m_{21} & m_{22} \end{pmatrix}^k \begin{pmatrix} x_0 \\ x_0' \end{pmatrix} .$$

With all elements being linear the matrix represents a linear mapping of (x_0, x_0') to points x_k, x_k' after k turns which lie on an ellipse

2.6.1 One-turn matrix at a symmetry point

We start with the case where the location of the particle observation is in the centre of an F quad and the ring consists of n FODO cells with the matrix (2). Using the phase advance around the ring $\mu = n\mu_c$ the one-turn matrix becomes

$$M = \begin{pmatrix} \cos(\mu_{cx}) & \beta_x \sin(\mu_{cx}) \\ \dfrac{-\sin(\mu_{cx})}{\beta_x} & \cos(\mu_{cx}) \end{pmatrix}^n = \begin{pmatrix} \cos\mu_x & \beta_x \sin\mu_x \\ \dfrac{-\sin\mu_x}{\beta_x} & \cos\mu_x \end{pmatrix} .$$

By choosing the centre of a quadrupole as observation point we have a special case where the phase-space ellipse is upright as shown on top of Fig. 25. The ratio between the maximum excursions in position and angle is expressed by the beta function

$$\hat{x}/\hat{x'} = \beta_x ,$$

which is a function of the position s around the ring and given by the optical properties of the lattice but independent of the beam. It is large in the centre of an F quad and small in the D quad as shown in Fig. 24. One important property of a circulating particle is the emittance, or normalized phase-space area $\epsilon_x = A/\pi$ from which the beam dimensions and angular spread can be obtained with the help of the β-function

$$\epsilon_x = \hat{x}\hat{x}' = \frac{\hat{x}^2}{\beta_x} = \hat{x}'^2\beta_x \ , \ \ \hat{x} = \sqrt{\epsilon_x\beta_x} \ , \ \ \hat{x}' = \sqrt{\frac{\epsilon_x}{\beta_x}} \ , \ \ \frac{x^2}{\beta_x} + \beta_x x'^2 = \epsilon_x \ .$$

The observed pair $(x_1,\, x_1')$ can be described by

$$\begin{aligned}
x_1 &= \cos\mu_x x_0 + \beta_x \sin\mu_x x_0' = C\cos(\mu_x - \phi) \\
C &= \pm\sqrt{x_0^2 + \beta_x^2 x_0'^2} = \sqrt{\epsilon_x\beta_x} \ , \quad \tan\phi = \frac{\beta_x x_0'}{x_0} \\
x_1' &= -\sin\mu_x x_0/\beta_x + \cos\mu_x x_0' = C'\cos(\mu_x - \phi) \\
C' &= \pm\sqrt{x_0^2/\beta_x^2 + x'^2_0} = \sqrt{\epsilon_x/\beta_x} \ , \quad \tan\phi' = \frac{\beta_x x_0'}{x_0} = \tan\phi \\
x_1 &= \sqrt{\epsilon_x\beta_x}\cos(\mu_x - \phi_0) \ , \quad x_1' = -\sqrt{\frac{\epsilon_x}{\beta_x}}\sin(\mu_x - \phi_0) \ .
\end{aligned}$$

Since transverse beam dynamics measurements done at a symmetry point are easier to understand, we shall later often assume this case only. More general cases are best analysed by using a computer model of the lattice.

2.6.2 General one-turn matrix

For a general observation point the dynamic is more complicated and the phase-space plot of deviations in position and angle is represented by a tilted ellipse of the same area. This is illustrated Fig. 25 which shows an observation at the quadrupole centre (top) and at its exit (bottom). The ellipse is upright in the first case but by going through the second half of the quadrupole the particle receives an angular kick $\Delta x_k' = -\frac{1}{2}x_k/|f|$ which slides vertical stripes of the ellipse up or down leading to a distortion. It is clear that this does not change the area of the ellipse.

To describe this general case we need in addition to the β-function its derivative $\beta_x'(s) = \mathrm{d}\beta_x(s)/\mathrm{d}s$. It is convenient to use now three quantities, called Twiss parameters, to describe the optics

$$\beta_x(s) \ , \ \ \alpha_x(s) = -\frac{1}{2}\beta_x'(s) = -\frac{1}{2}\frac{\mathrm{d}\beta_x(s)}{\mathrm{d}s} \ , \ \ \gamma_x(s) = \frac{1+\alpha_x^2(s)}{\beta_x(s)} \ ,$$

with corresponding parameters in the vertical direction β_y, α_y, γ_y. Obviously the three are not independent. In a symmetry point we have $\alpha_x = 0$, $\gamma_x = 1/\beta_x$.

In this general case the one-turn matrix is

$$\begin{aligned}
M_x &= \begin{pmatrix} m_{11} & m_{12} \\ m_{21} & m_{22} \end{pmatrix} = \begin{pmatrix} \cos\mu_x + \alpha_x\sin\mu_x & \beta_x\sin\mu_x \\ -\gamma_x\sin\mu_x & \cos\mu_x - \alpha_x\sin\mu_x \end{pmatrix} \ , \ \ |M_x| = 1 \\
\cos\mu_x &= \frac{m_{11}+m_{22}}{2} \ , \ \ \beta_x^2 = \frac{m_{12}^2}{1 - \left(\frac{m_{11}+m_{22}}{2}\right)^2} \ , \ \ \alpha_x^2 = \frac{\left(\frac{m_{11}-m_{22}}{2}\right)^2}{1 - \left(\frac{m_{11}+m_{22}}{2}\right)^2}
\end{aligned} \tag{3}$$

and the k-turn matrix is obtained by multiplying μ_x by k. The ellipse parameters are shown in Fig. 26.

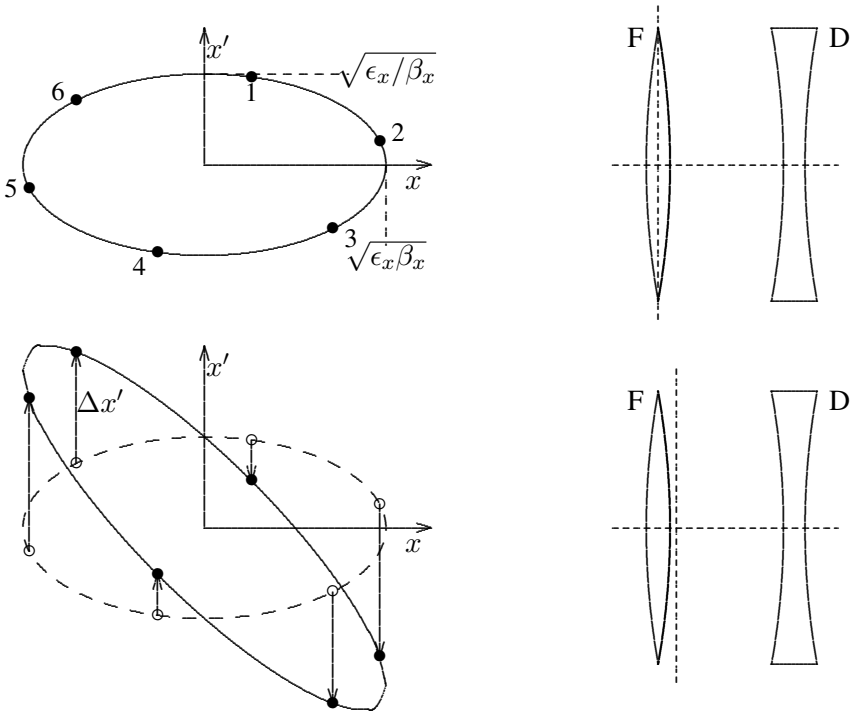

Fig. 25: Upright and tilted ellipse in the quadrupole centre and at its exit

$$\epsilon_x = \gamma_x x^2 + 2\alpha_x x x' + \beta_x x'^2$$
$$\beta_x \epsilon_s = x^2 + \left(\alpha_x x + \beta_x x'\right)^2 \quad (4)$$
$$\hat{x} = \sqrt{\epsilon_x \beta_x}\ , \quad \hat{x}' = \sqrt{\epsilon_x \gamma_x}$$
$$\epsilon_x = \frac{\hat{x}^2}{\beta_x} = \frac{\hat{x}'^2}{\gamma_x} = \frac{\hat{x}\hat{x}'}{\sqrt{\beta_x \gamma_x}}$$

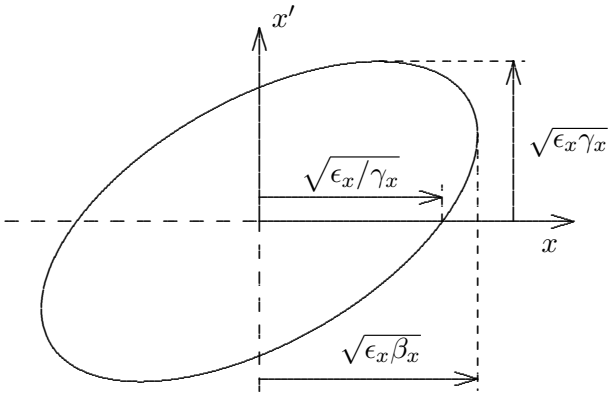

Fig. 26: Parameters of the general phase-space ellipse

The coordinates $(x_1,\, x_1')$ seen after a turn at location s with $\beta_x(s)$, $\alpha_x(s)$, $\gamma_x(s)$ are

$$x_1 = (\cos\mu_x + \alpha_x \sin\mu_x)x_0 + \beta_x \sin\mu_x x_0' = C\cos(\mu_x - \phi)$$
$$C = \sqrt{x_0^2 + (\alpha_x x_0 + \beta_x x_0')^2} = \sqrt{\epsilon_x \beta_x}\ , \quad \tan\phi = \frac{\alpha_x x_0 + \beta_x x_0'}{x_0}$$
$$x_1' = -\gamma_x \sin\mu_x x_0 + (\cos\mu_x - \alpha_x \sin\mu_x)x_0' = C'\cos(\mu_x - \phi')$$
$$C = \sqrt{\gamma^2 x_0^2 + 2\gamma_x \alpha_x x_0 x_0' + (1+\alpha_x^2)x_0'^2} = \sqrt{\epsilon_x \gamma_x}\ , \quad \tan\phi' = \frac{x_0'}{\gamma_x x_0 + \alpha_x x_0'}$$
$$x_1 = \sqrt{\epsilon_x \beta_x}\cos(\mu_x - \phi)\ , \quad x_1' = \sqrt{\epsilon_x \gamma_x}\sin(\mu_x - \phi')\ .$$

2.7 Particle trajectory within one turn

Position and angle x_1, x_1' at s_1 of a ring are obtained from x_0, x_0' at s_0 by multiplication by the transfer matrix between these points, Fig. 27. The matrix elements m_{ij} can be expressed by the betatron phase advance $\phi(s)$ along s and the lattice functions $\beta_x(s),\ \alpha_x(s)$ which depend now on s and are in general different at the two points. This matrix becomes complicated and the trajectory is better expressed with

$$x(s) = \sqrt{\epsilon_x \beta_x(s)}\cos(\phi_x(s) - \phi_0)$$

$$x'(s) = -\sqrt{\frac{\epsilon_x}{\beta_x(s)}}\left(\alpha_x(s)\cos(\phi_x(s) - \phi_0) + \sin(\phi_x(s) - \phi_0)\right) = -\sqrt{\epsilon_x \gamma_x}\cos(\phi_x(s) - \phi_1)$$

$$\frac{\mathrm{d}\phi_x}{\mathrm{d}s} = \frac{1}{\beta_x(s)}\ ,\quad \phi_x \text{ advances fast where } \beta_x \text{ is small.}$$

Since the amplitude is proportional to $\sqrt{\epsilon_x \beta_x(s)}$ the square root of the beta function represents an envelope of all trajectories having different phases but the same emittance.

$$\begin{aligned} x_1 &= m_{11}x_0 + m_{12}x_0' \\ x_1' &= m_{21}x_0 + m_{22}x_0' \end{aligned}$$

$$\begin{pmatrix} x_1 \\ x_1' \end{pmatrix} = \begin{pmatrix} m_{11} & m_{12} \\ m_{21} & m_{22} \end{pmatrix} \begin{pmatrix} x_0 \\ x_0' \end{pmatrix}$$

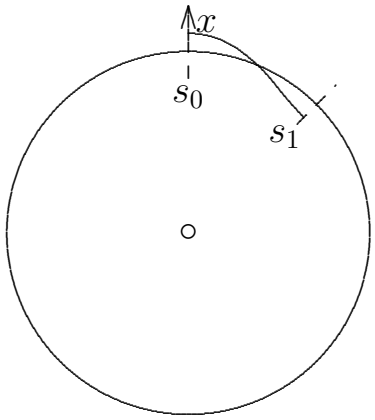

Fig. 27: Particle trajectory within one turn

Between focusing elements, $\beta_x(s)$ propagates with s as

$$\beta_x(s) = \beta_x(0) + \beta_x'(0)s + \frac{1}{2}\beta_x''(0)s^2 = \beta_x(0) - 2\alpha_x(0)s + \gamma_x(0)s^2.$$

2.8 Beam with many particles

The many particles in a beam execute betatron oscillations of different phases and amplitudes. Their phase-space ellipses have different areas but at a given location the same orientation and aspect ratio, as shown in Fig. 28. Therefore, the beam as a whole covers a phase-space distribution $\psi(x, x')$ with a beam emittance being the average of the ones taken by the individual particle ellipses $E_x = \langle \epsilon_x \rangle$.

The most complete description of such a beam is the phase-space distribution $\psi(x, x')$, with the projections $f(x)$ and $g(x')$ as shown in Fig. 29.

- One position monitor measures $\langle x \rangle$, a pair can measure $\langle x' \rangle$. In many measurements the whole beam behaves like a single particle.
- Synchrotron radiation gives the spatial distribution $f(x)$ if used for imaging, and the angular distribution $g(x')$ in direct observation, as shown in Figs. 15 and 16.

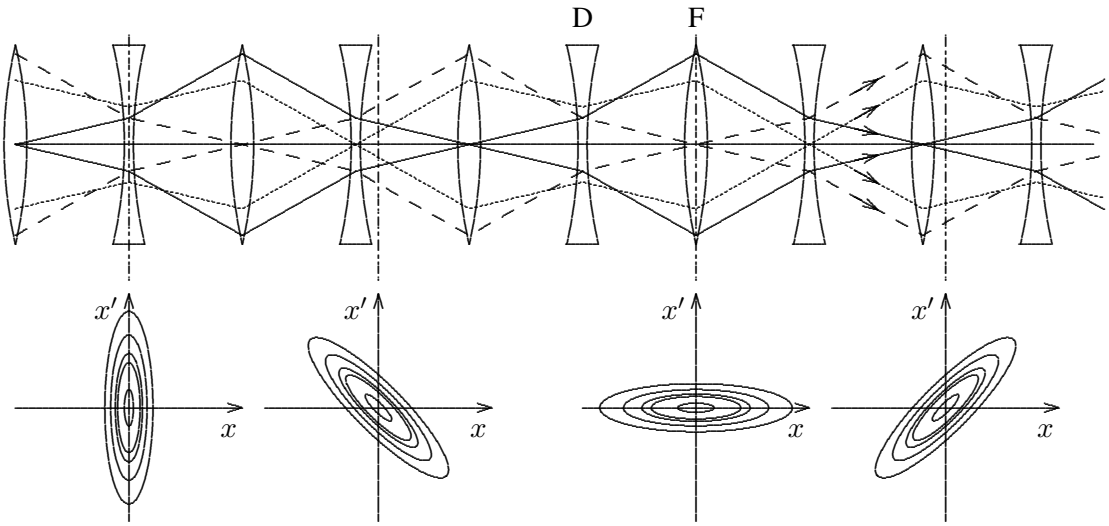

Fig. 28: Beam with many particles of different emittances

$$f(x) = \int \psi(x,x')\mathrm{d}x'$$
$$g(x') = \int \psi(x,x')\mathrm{d}x$$
$$\langle x\rangle = \frac{\int f(x)x\mathrm{d}x}{\int f(x)\mathrm{d}x}$$
$$\langle x'\rangle = \frac{\int g(x')x'\mathrm{d}x'}{\int g(x')\mathrm{d}x'}$$
$$\sigma_x^2 = \frac{\int f(x)x^2\mathrm{d}x}{\int f(x)\mathrm{d}x}$$
$$\sigma_x'^2 = \frac{\int g(x')x'^2\mathrm{d}x'}{\int g(x)\mathrm{d}x'}$$

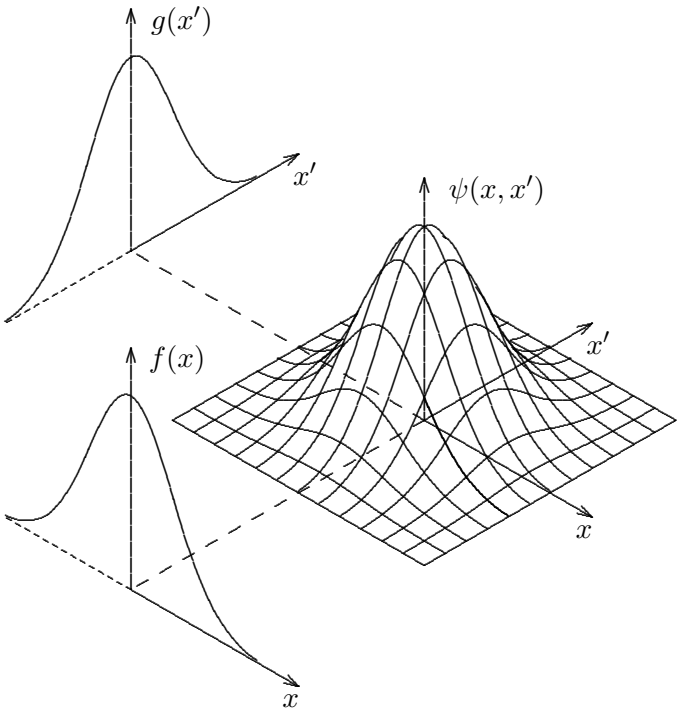

Fig. 29: Phase-space distribution with projections

2.9 Perturbations to the beam optics

2.9.1 Closed-orbit distortion by a dipole error

In a machine with a beam on the nominal closed orbit we make a local deflection $\Delta\theta$ with a dipole magnet. We calculate the new closed orbit including this deflection

$$x(s) = \sqrt{\epsilon_x\beta_x(s)}\cos(\phi_x(s)-\phi_0)$$
$$x'(s) = \sqrt{\frac{\epsilon_x}{\beta_x(s)}}\left(\alpha_x(s)\cos(\phi_x(s)-\phi_0)+\sin(\phi_x(s)-\phi_0)\right)$$
$$x(0) = x(2\pi R)\,,\quad x'(0) \;=\; x'(2\pi R)+\Delta\theta$$

$$x(s) = \frac{\Delta\theta\sqrt{\beta_x(0)\beta_x(s)}}{2}\frac{\cos(\pi Q_x - \phi_x(s))}{\sin(\pi Q_x)}. \tag{5}$$

The orbit distortion propagates around the ring like a betatron oscillation, Fig. 30. Of special interest for measurements is the distortion $x(0)$ right at the dipole error

$$x(0) = \frac{\Delta\theta\beta_x(0)}{2}\cot(\pi Q_x). \tag{6}$$

If Q_x is close to an integer the distortion is large — integer stop band.

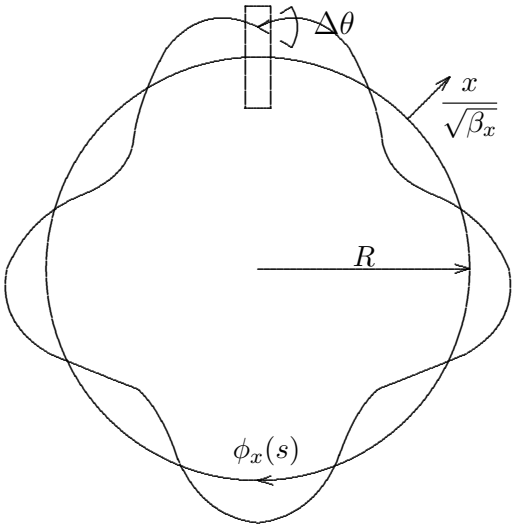

Fig. 30: Orbit distortion due to a dipole error

2.9.2 Tune and beta function change by a quadrupole error

We introduce a weak extra quadrupole in a ring with nominal tune $\mu_0 = 2\pi Q_0$ and calculate the resulting tune change ΔQ. We get the new transfer matrix, with parameters β_1, α_1, γ_1, μ_1, by multiplying the unperturbed matrix, having parameters β_1, α_1, γ_1, μ_0, by the one of a thin quadrupole of focusing strength $1/f$

$$\begin{aligned} M_1 &= \begin{pmatrix} \cos\mu_1 + \alpha_1\sin\mu_1 & \beta_1\sin\mu_1 \\ -\gamma_1\sin\mu_1 & \cos\mu_1 - \alpha_1\sin\mu_1 \end{pmatrix} \\ &= \begin{pmatrix} \cos\mu_0 + \alpha_0\sin\mu_0 & \beta_0\sin\mu_0 \\ -\gamma_0\sin\mu_0 & \cos\mu_0 - \alpha_0\sin\mu_0 \end{pmatrix} \cdot \begin{pmatrix} 1 & 0 \\ -1/f & 1 \end{pmatrix} \\ &= \begin{pmatrix} \cos\mu_0 + \alpha_0\sin\mu_0 - \beta_0\sin\mu_0/f & \beta_0\sin\mu_0 \\ -\gamma_0\sin\mu_0 - (\cos\mu_0 - \alpha_0\sin\mu_0)/f & \cos\mu_0 - \alpha_0\sin\mu_0 \end{pmatrix} . \end{aligned}$$

The new phase advance per turn is given according to (3) by the matrix trace

$$\cos\mu_1 = \cos(\mu_0 + \Delta\mu) = \frac{1}{2}(m_{11} + m_{22}) = \cos\mu_0 - \frac{\beta_0}{2f}\sin\mu_0 \, .$$

For small perturbation we expand to first order in $\Delta\mu$ giving

$$\Delta\mu = \frac{\beta_0}{2f} \, , \quad \Delta Q = \frac{\beta_0}{4\pi f} \, . \tag{7}$$

This relation is used to measure the β function by observing the tune change ΔQ as a function of $1/f$. If the second order is included we find

$$\Delta Q \approx \frac{\beta_0}{4\pi f}\left(1-\frac{\beta_0}{4f\tan(2\pi Q)}\right)\ ,\quad \beta_0 \approx 4\pi f\Delta Q\left(1+\frac{\pi\Delta Q}{\tan(2\pi Q_0)}\right)\ .$$

From the matrix element m_{12} we find also a change of the beta function at the inserted quadrupole which is to first order

$$\beta_1\sin\mu_1 = (\beta_0+\Delta\beta)\sin(\mu_0+\Delta\mu) = \beta_0\sin\mu_0$$
$$\frac{\Delta\beta}{\beta_0} \approx -\frac{\Delta\mu}{\tan\mu_0} = -\frac{2\pi\Delta Q}{\tan(2\pi Q_0)} = -\frac{\beta_0}{2f\tan(2\pi Q_0)}\ .$$

This effect is strong if the value of Q_0 is close to an integer or half-integer.

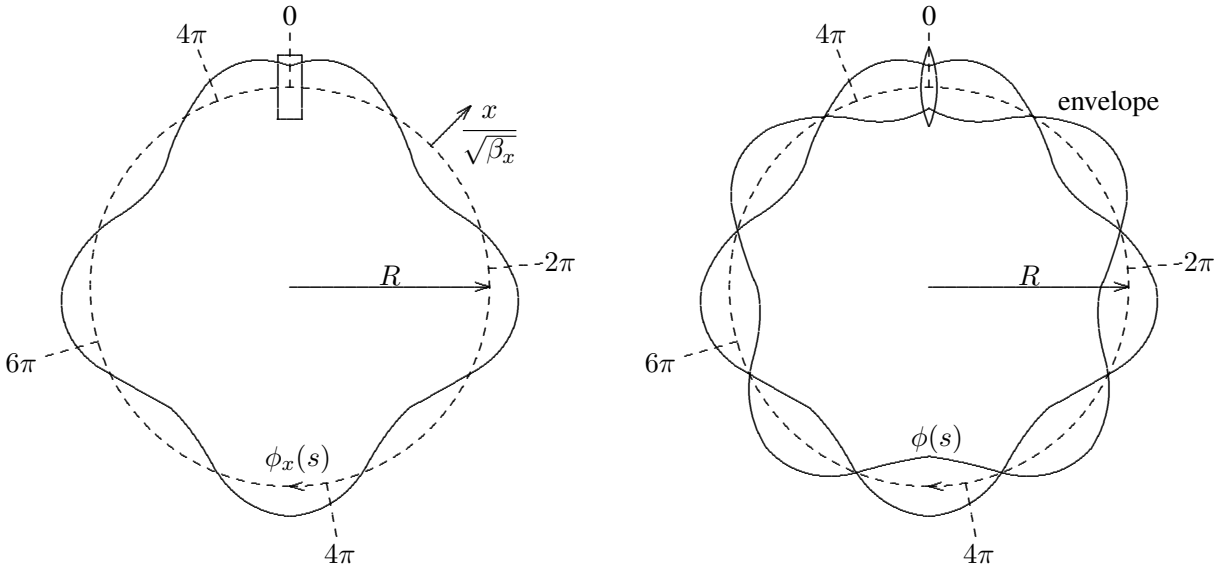

Fig. 31: Left: dipole error gives an orbit distortion advancing with betatron phase ϕ_s; right: quadrupole error gives a beating of the beam envelope, i.e., beta function, around the ring advancing with twice the betatron phase

A quadrupole error not only perturbs the beta function at its location but also creates a beating of the nominal beta function around the machine. This advances with twice the unperturbed phase advance $\cos(2\phi_0(s)-\phi_a)$, as illustrated in Fig. 31. Owing to the relation between $\beta(s)$ and $\phi(s)$ there is also a beating in the phase advance giving to lowest approximation

$$\frac{\Delta\beta}{\beta} \propto \cos(2\phi_0(s)-\phi_a)\ ,\quad \frac{1}{\beta(s)} = \frac{\mathrm{d}\phi(s)}{\mathrm{d}s}\ \rightarrow\ \Delta\phi(s) \propto \cos(2\phi_0(s)-\phi_b)\ .$$

As a consequence of the beating with $2\phi_0(s)$, two points which were separated by $n\pi$ without the perturbation still have the same phase separation including it as long as the focusing error does not lie in between them. This is helpful for locating errors.

2.9.3 Tilted quadrupoles

We approximate these quadrupoles by short lenses and give the magnetic field relations, the expressions for the particle transfer, and the corresponding matrices.

$$\text{Normal F quad: } B_x = ky\ ,\quad B_y = kx\ ,\quad \Delta x' = -\frac{x}{f}\ ,\quad \Delta y' = \frac{y}{f}\ ,$$

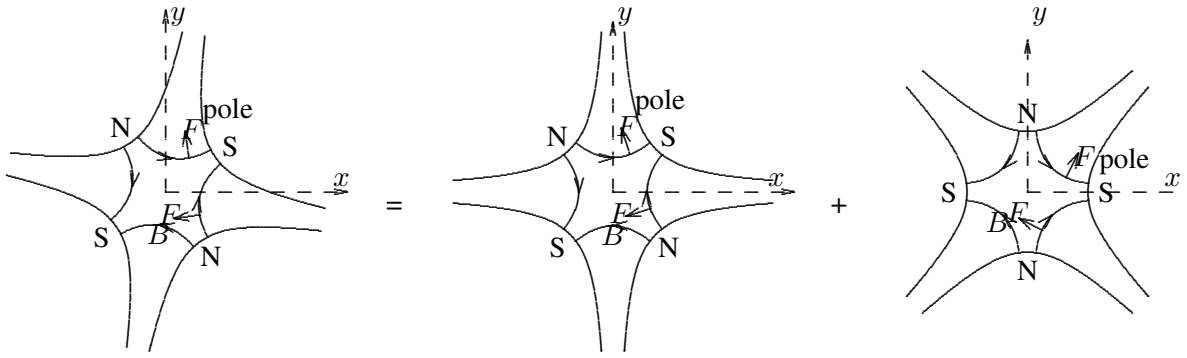

Fig. 32: Imitate a small tilt by a normal quad and a weak one being rotated by 45°

$$\begin{array}{rcrcl} x_1 &=& x_0 & & \\ x_1' &=& -x_0/f &+& x_0' \\ y_1 &=& y_0 & & \\ y_1' &=& y_0/f &+& y_0' \end{array} \quad \rightarrow \quad \begin{pmatrix} x_1 \\ x_1' \\ y_1 \\ y_1' \end{pmatrix} = \begin{pmatrix} 1 & 0 & 0 & 0 \\ -1/f & 1 & 0 & 0 \\ 0 & 0 & 1 & 0 \\ 0 & 0 & 1/f & 1 \end{pmatrix} \cdot \begin{pmatrix} x_0 \\ x_0' \\ y_0 \\ y_0' \end{pmatrix} .$$

Rotated quad: $B_x = kx\ ,\ \ B_y = -kx\ ,\ \ \Delta x' = \dfrac{y}{f}\ ,\ \ \Delta y' = \dfrac{x}{f}\ ,$

$$\begin{array}{rcrcl} x_1 &=& x_0 & & \\ x_1' &=& y_0/f &+& x_0' \\ y_1 &=& y_0 & & \\ y_1' &=& x_0/f &+& y_0' \end{array} \quad \rightarrow \quad \begin{pmatrix} x_1 \\ x_1' \\ y_1 \\ y_1' \end{pmatrix} = \begin{pmatrix} 1 & 0 & 0 & 0 \\ 0 & 1 & 1/f & 0 \\ 0 & 0 & 1 & 0 \\ 1/f & 0 & 0 & 1 \end{pmatrix} \cdot \begin{pmatrix} x_0 \\ x_0' \\ y_0 \\ y_0' \end{pmatrix} .$$

We approximate a small tilt of a lens by a normal quadrupole and a weak one being rotated by 45°, as shown in Fig. 32.

A tilted quadrupole produces coupling between horizontal and vertical betatron oscillations. If it is located at finite horizontal dispersion it also produces vertical dispersion. These two effects are responsible for most of the vertical emittance in an electron ring. This coupling can be compensated for with rotated quadrupoles. A single tilted quad would be sufficient if it is located at the correct horizontal and vertical betatron phase. Since the two phases usually advance by different amounts and the location of the coupling source is not known, four rotated quads are generally needed. However, a smaller number is already helpful.

3 Transverse measurements

3.1 Overview

Transverse measurements are treated in order of increasing complexity, starting with static beam condition, going to oscillations and phase-space observation, as listed in Table 1 together with the necessary instruments. The topics on the last line are important for continuous beams without bunches and will not be treated here.

3.2 Equilibrium conditions — static measurements

3.2.1 Orbit distortion by single deflection

The effect of a single deflection was treated before and the resulting orbit distortion is shown in general in Fig. 30 and in detail in Fig. 33.

This measurement can be done with any corrector and gives useful information. The orbit is measured before and after applying a deflection angle $\Delta\theta$ at a location $s = 0$. This gives the so-called

Table 1: List of transverse measurements with the necessary tools

Conditions	Observation	Action
	position monitor	deflector, change ring parameters
static, equilibrium conditions	closed orbit, lattice functions, physical aperture	orbit correction, beam bumps
dynamic, oscillations, turn by turn	tunes, lattice functions, dynamic aperture	excite transverse oscillations
excitation-response relation	pulse excitation (Green function) harmonic excitation (transfer function)	
excitation-response dependence	feed-back systems, tune control, instabilities	

'difference orbit' which avoids the influence of other deflections. Outside the deflector, around the rest of the ring, the orbit is given by (5)

$$x(s) = x(0)\sqrt{\beta_x(s)/\beta_x(0)}\cos(\phi_x(s) - \phi_0),$$

with $\phi_x(s)$ being the betatron phase advance.
The conditions $x(0) = x(2\pi R),\ x'(0) = x'(2\pi R) + \Delta\theta$ give for the difference orbit

$$x(s) = \frac{\Delta\theta\sqrt{\beta_x(s)\beta_x(0)}}{2}\frac{\cos(\pi Q_x - \phi_x(s))}{\sin(\pi Q_x)}\ .$$

This orbit distortion, normalized by $\sqrt{\beta_s(\phi_x)}$, being plotted at the bottom of Fig. 33 as a function of the betatron phase $\phi(s)$, is much easier to understand than the one of raw data shown on top of this figure. It visualizes the betatron phase advance, general behaviour of the beta function, and gives the integer and approximately the fractional part of the tune Q_s. For this reason it useful to have the option to show the raw and the normalized orbit. However, this requires knowledge of the optical functions $\beta_x(s)$ and $\phi_x(s)$. Since one tries to obtain them with such a measurement, some iteration might be necessary.

Interesting information can be extracted from the measured difference orbit close to $s = 0$ where the deflection is applied and where the normalized orbit has a cusp, as shown in Fig. 34. We find from

$$x(0) = \frac{\Delta\theta}{2}\beta_x(0)\cot(\pi Q_x)\ \rightarrow\ \beta_x(0) = \frac{2x_0\tan(\pi Q_x)}{\Delta\theta}\ .$$

It gives the value of either the tune or the beta function at the deflection if the other is known. For this reason it is good to have position monitors and deflectors close by.

3.2.2 Response matrix

After measuring $\beta(0)$ and $\beta(1)$ at two monitor–corrector pairs we can determine the phase advance $\phi(s_1) - \phi(s_0)$ between them.

$$x(s) = \frac{\Delta\theta\sqrt{\beta_x(s)\beta_x(0)}}{2}\frac{\cos(\pi Q_x - \phi(s_1))}{\sin(\pi Q_x)}\ .$$

As a further step the orbit change is measured everywhere for the variation of each corrector. For a sufficiently dense distribution of monitors and deflectors the obtained system of equations is overdetermined and also gives information about the calibrations. This method is called 'response matrix' and is based on difference orbit measurements which are very accurate [6].

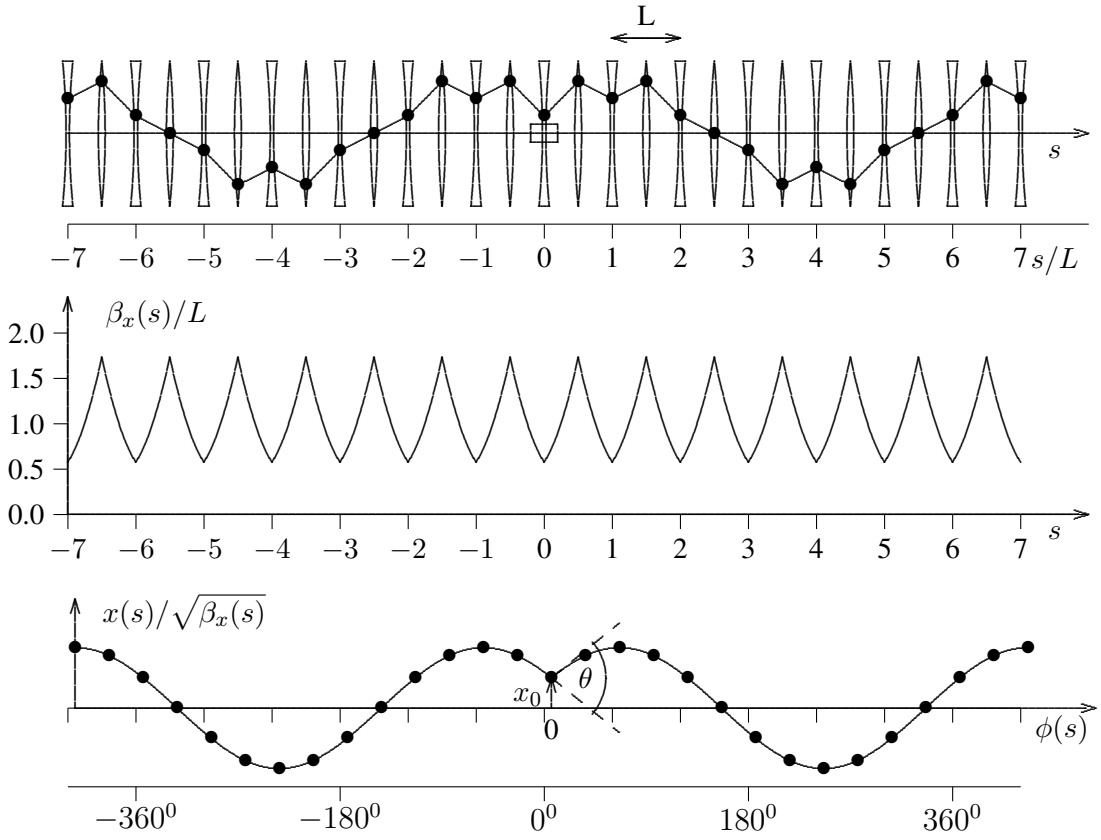

Fig. 33: Orbit perturbation in direct and normalized presentation

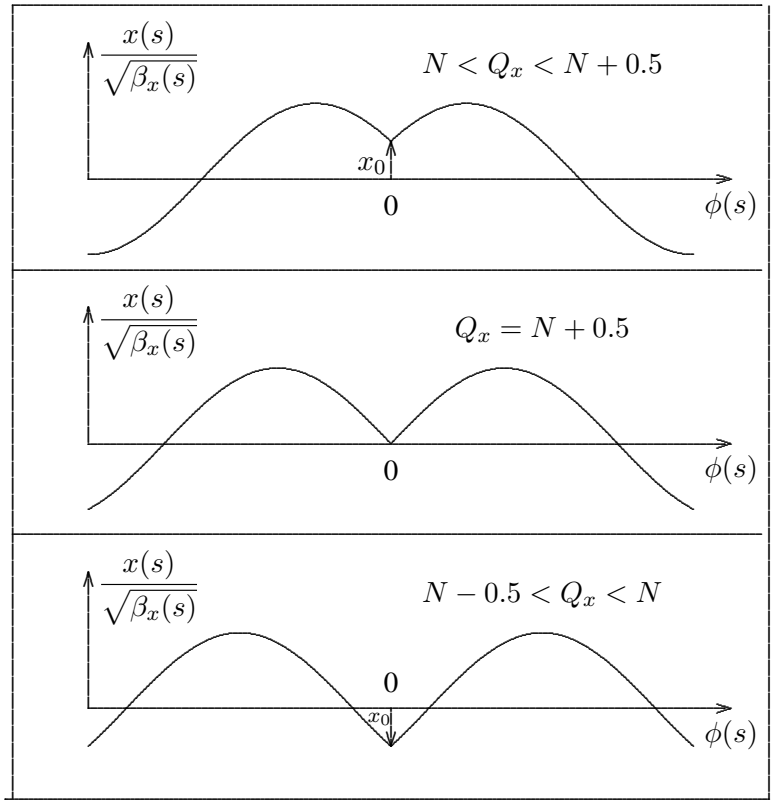

Fig. 34: Orbit close to the deflection for Q_x being above, on, and below the half-integer

3.2.3 Beam bumps

Local beam bumps are important tools for some machine measurements. Some correctors are powered to create a local orbit distortion which vanishes in the rest of the ring. If there are correctors separated by a betatron phase of $n\pi$, only two are needed, otherwise one more is necessary, as illustrated in Fig. 35.

Applications: Local scans to find physical aperture limitations; centring the beam in quadrupoles, sextupoles or other devices; scraping the beam to reduce the current in a controlled way or to measure the transverse distribution of the particles in a beam; localize elements which produce coupling by making a horizontal bump and look for vertical orbit distortions.

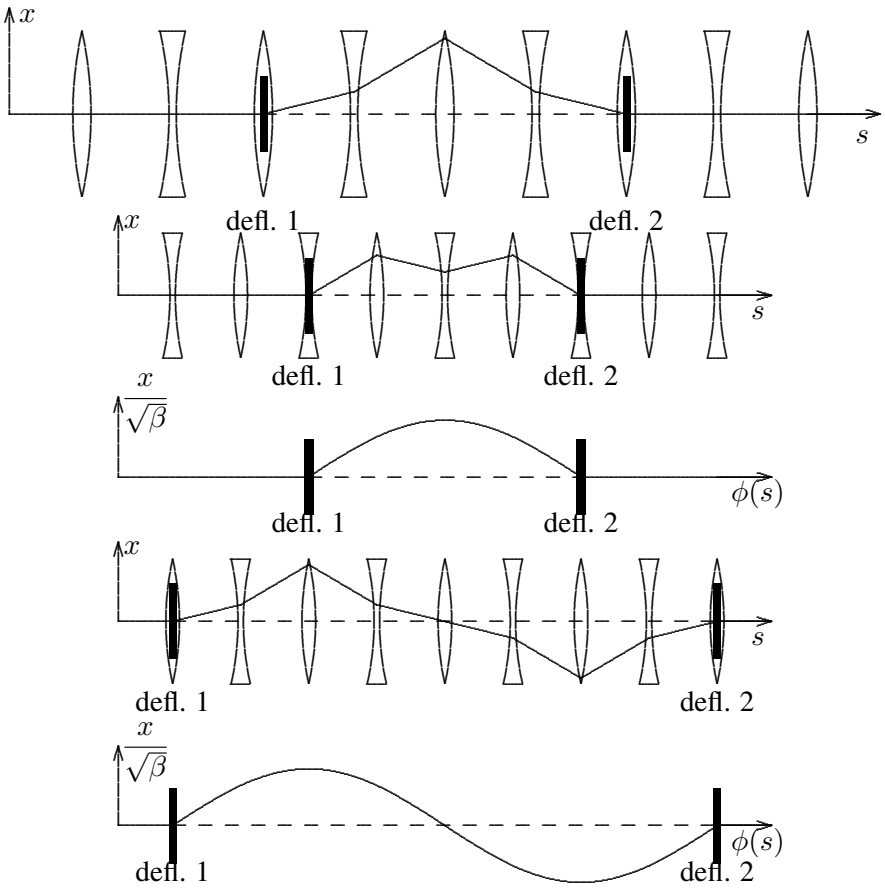

Fig. 35: Beam bumps of π and 2π phase advance between deflectors

3.2.4 Beam-based alignment of the position monitors with respect to quadrupoles

Beam position monitors are usually aligned with respect to the nominal orbit which goes through the centres of the quadrupoles. This can be checked by making a small quadrupole strength change, often called K modulation, and observing the resulting orbit change. The deflection in a quadrupole of length L and focusing parameter K of a beam with an off-set x_0 with respect to the quadrupole axis is

$$x_0' = -\frac{x_0}{f} = -x_0 L K \;\rightarrow\; \Delta x' = -x_0 L \Delta K \; .$$

Since only the resulting modulation of the orbit has to be observed, the strength change can be kept small so as to avoid large tune changes. The measurement is usually done by moving the beam with a bump in steps through the quadrupole and checking the orbit motion due to a K change at each point to find its minimum.

3.3 Measurements based on betatron oscillations

3.3.1 Measuring betatron frequencies — tunes

To measure the tune, we excite a betatron oscillation either with a short deflecting pulse or a harmonic deflection with swept frequency and observe it with a position monitor (Fig. 36).

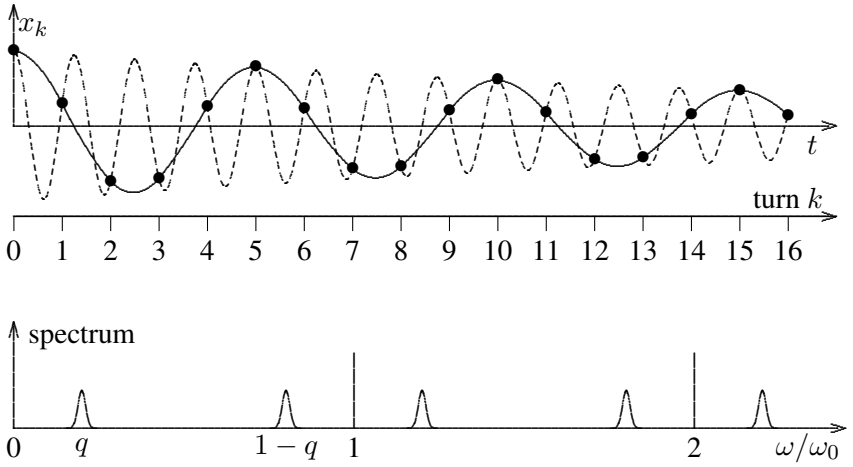

Fig. 36: Exciting and frequency measurement of betatron oscillations. Top: pulse excitation; bottom: swept frequency excitation.

In the first case we observe the coherent centre-of-mass signal in time domain giving values x_k each revolution k which are fitted by damped oscillations of frequencies

$$\omega_\beta = (n \pm q)\omega_0$$

where ω_0 is the revolution frequency, q the fractional part of the tune $Q =$ integer $+ q$, and n a free fitting integer. This is shown on top of the figure with two fits $\omega_\beta = q\omega_0$ and $\omega_\beta = (1-q)\omega_0$. The signal from the free betatron oscillation is decaying either by the synchrotron radiation damping in an electron ring or by the phase mixing of the individual particle motions due to a spread of betatron tunes which is related to Landau damping.

The second measurement method works in frequency domain and is shown on the bottom of the figure. The beam is excited with a swept frequency ω and its response measured. It is large when the frequency goes through one of the betatron frequencies $\omega \approx \omega_\beta$. The obtained spectrum has betatron sidebands of finite widths due to a tune spread or damping.

As far as the instrument is concerned, the measurement is carried out with a spectrum analyser having a tracking generator output of the sweeping frequency, a network analyser, or an FFT with noise excitation. Since this measurement can be carried out at any frequency $\omega_\beta = (n \pm q)\omega_0$, one normally chooses one for which the exciter and the position monitor give strong signals. One only obtains the fractional part q of the tune since the beam motion is only observed at one location without any information from the rest of the ring. Even this part is ambiguous corresponding to q or $1-q$. This can be resolved by repeating the measurement with a slightly higher excitation of a focusing quadrupole which should increase the tune Q, or by making a deflection and observing the cusp, Fig. 34. The integer part of the tune is usually determined from a closed-orbit distortion measurement.

Applications:

- Measure the betatron frequency ω_β and the tune Q; $\omega_\beta = \omega_0(n \pm Q)$
- $Q = Q(\Delta E) \rightarrow Q'$ chromaticity
- Dynamic aperture

- $Q = Q(\Delta K)$ tune as a function of quad strength $\Delta Q = \beta \Delta K L/(4\pi)$
- Observe vertical oscillation driven by a horizontal excitation — coupling
- Measure growth of self-excited oscillation — instability driven by impedance Z_{Tr}

3.3.2 Measure non-linearities

By measuring the tune for different betatron amplitudes we can study non-linearities. For the time domain observation one should give the beam a deflection of different amplitude and not rely on the decaying signal amplitude, since this might be due to phase mixing. In frequency domain measurements, one sweeps through the betatron frequency with different excitation strengths.

3.3.3 Measuring the beta function at a quadrupole

A single quadrupole strength change $L\Delta K = 1/f$ leads to a change ΔQ of the tune. This can be used to measure the beta function, (7)

$$\Delta Q = \frac{\beta}{4\pi} L \Delta K \quad \rightarrow \quad \beta = \frac{4\pi}{L} \frac{\Delta Q}{\Delta K} \, .$$

In this measurement we make a *small* change of a quadrupole strength and observe the resulting tune variation. If the change is larger we also change the beta function at the quadrupole and can use a better approximation

$$\beta = \frac{4\pi}{L} \frac{\Delta Q}{\Delta K} \left(1 + \frac{\Delta Q}{\tan Q} \right) \, .$$

This is still a short lens approximation and gives some average β in a longer quadrupole. There are some limitations:

- For a long quadrupole we have to know something about the optics in the neighbourhood of the quadrupole to interpret the average beta measured. Usually one calculates the expected ΔQ for a given ΔK with the lattice model and a computer code and does the experiment to check it.
- Owing to the hysteresis effect, a small current change does not always give a well known field change. We make a change in both directions, a larger change, or use an induction loop measuring $\dot{B}$ and integrate.
- Most rings have only a few quadrupoles with individual powering but they are usually the important ones.

Application: Check low-beta insertion. One of the critical optical elements in a circular collider is the low-beta insertion. Measuring the beta function in the closest quadrupoles gives the beta function in the interaction point from

$$\beta(s) = \beta_{\text{min}} \left(1 + \left(\frac{s - s_0}{\beta_{\text{min}}} \right)^2 \right)$$

and locates the minimum which should be in the centre, Fig. 37.

3.3.4 Measure dynamic acceptance

The dynamic acceptance (dynamic aperture) is the normalized maximum betatron oscillation amplitude which is accepted by the beam optics. Because of non-linear elements (sextupoles, octupoles) the betatron tune changes with oscillation amplitude resulting eventually in an instability. This acceptance is measured by exciting a betatron oscillation and slowly increasing its amplitude until the beam life-time becomes short. The amplitude has now reached the dynamic acceptance, as indicated in Fig. 38. To measure it we move a scraper into the beam until the life-time gets even smaller. We measure the distance

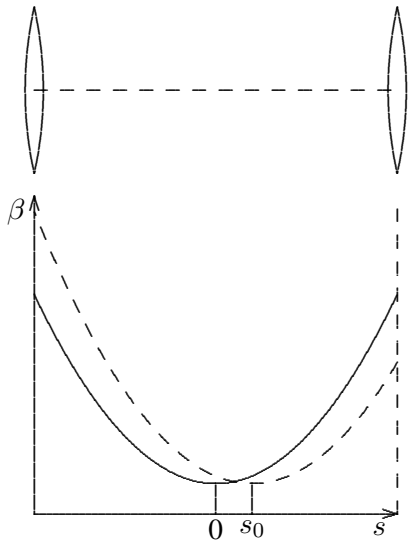

Fig. 37: Measure the longitudinal centring of the 'low beta' insertion

x_a of the scraper from the axis and get for the acceptance $A = x_a^2/\beta$. At this point one should check if it is not due to a tune change. The betatron oscillation can also be excited by a kick. In this case one often increases the amplitude until half the intensity is lost and then makes a calibration later.

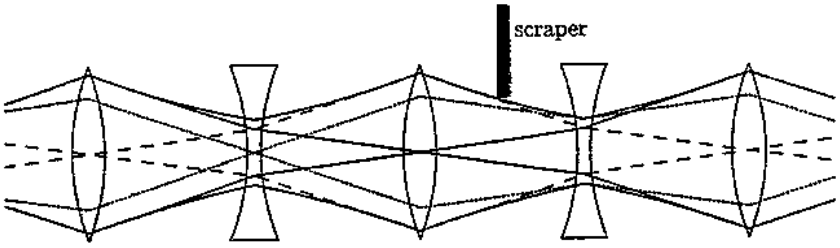

Fig. 38: Measuring dynamic acceptance

3.4 Coupling measurement

Usually the horizontal and vertical betatron oscillations are treated independently. However, certain elements, rotated quadrupoles as shown in Fig. 32, and solenoids, can couple the two motions.

3.4.1 Cross excitation and measurement of betatron oscillations

The coupling can be measured by kicking the beam in one plane and observing the resulting oscillation in both planes. In the example shown in Fig. 39 a beam in the ISR was pulse excited in the horizontal plane (bottom) and the resulting oscillation observed in both planes [7]. The beam oscillations in the two planes behave like two coupled pendulums with energy going from one to the other and vice versa. Provided $\beta_x \approx \beta_y$ the modulations in the two planes should have about the same amplitude but opposite phase as confirmed by the measurement.

3.4.2 Closest tune approach

The tunes are changed by varying the strength of a quadrupole until they cross. During this operation both are carefully measured and plotted, Fig. 40. Owing to coupling they will not simply cross but

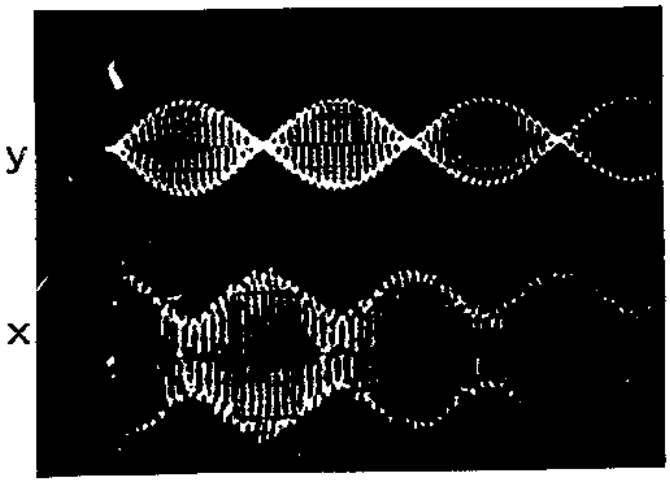

Fig. 39: Coupling measurement by cross excitation

approach each other to a point where they are no longer distinguishable and become separated again later. The stronger the coupling, the larger this unclear region.

We take as approximation two coupled oscillations corresponding to a machine with uniform focusing and some coupling

$$\ddot{x} + Q_x^2\omega_0^2 x = ky \ \ , \ \ \ddot{y} + Q_y^2\omega_0^2 y = kx$$

seeking a solution $x = A\exp(-\lambda t)$, $y = B\exp(-\lambda t)$

$$\begin{gathered} A(Q_x^2\omega_0^2 - \lambda^2) = Bk \ , \ \ B(Q_y^2\omega_0^2 - \lambda^2) = Ak \\ \frac{B}{A} = \frac{Q_x^2\omega_0^2 - \lambda^2}{k} = \frac{k}{Q_y^2\omega_0^2 - \lambda^2} \\ (Q_x^2\omega_0^2 - \lambda^2)(Q_y^2\omega_0^2 - \lambda^2) = k^2 \\ \lambda^4 - \lambda^2(Q_x^2 + Q_y^2)\omega_0^2 + Q_x^2Q_y^2\omega_0^4 - k^2 = 0 \\ \lambda^2 = \frac{\omega_0^2(Q_x^2 + Q_y^2) \pm \sqrt{(Q_x^2 - Q_y^2)^2\omega_0^4 - k^2}}{2} = 0 \ . \end{gathered}$$

Far from the crossing point of the tunes we have

$$(Q_x^2 - Q_y^2) \gg 2k/\omega_0^2 \ \ \rightarrow \ \ \lambda_1 = Q_x\omega_0 \ \ , \ \ \lambda_2 = Q_y\omega_0 \ ,$$

while at the crossing point we get

$$Q_x = Q_y = Q \ \ \rightarrow \ \ \lambda^2 = Q^2\omega_0^2 \pm k \ \ , \ \ \lambda_1^2 - \lambda_2^2 = 2k \ .$$

If the coupling is not too strong we get two solutions for λ with a difference being directly related to the coupling constant we like to measure:

$$k \ll Q^2\omega_0^2 \ \rightarrow \ \lambda \approx Q\omega_0\left(1 \pm \frac{k}{2Q^2\omega_0^2}\right) \ , \ \ \Delta\lambda = \lambda_1 - \lambda_2 \approx \frac{k}{Q\omega_0} \ .$$

The two betatron tunes behave like the frequencies of the two coupled oscillators during such an experiment as shown in Fig. 40.

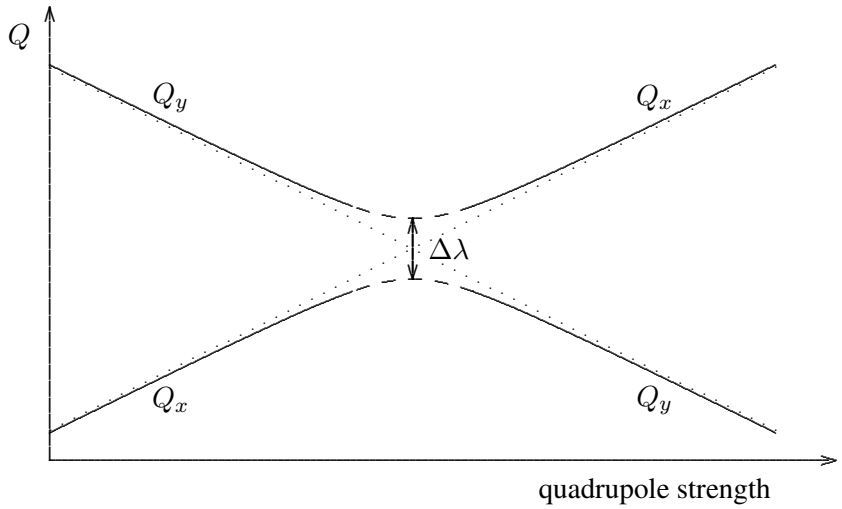

Fig. 40: Coupling measurement by 'closest tune approach'

3.5 Phase measurements

3.5.1 Two fast monitors — experimental tracking

The non-linear optics of a storage ring is often studied theoretically by tracking. A particle is launched with some initial offset and angle $(x_0,\, x_0')$ and its trajectory calculated. After each revolution the co-ordinate pair (x_n, x_n') is plotted, as described earlier. In a linear machine these points lie on an ellipse; however, non-linearities distort this curve.

We can study an existing machine experimentally with the same method. A fast angular deflection excites a betatron oscillation at some time and the beam position is observed turn by turn using two position monitors being separated in betatron phase by $90°$. These two monitors are equivalent to a measurement of position and angle at one location. To have clean conditions one observes the beam for a limited number of turns and repeats the observation with a different initial kick amplitude.

We use two fast position monitors separated in betatron phase by $\pi/2$. For simplicity we take $\alpha = -\beta'/2 = 0$ for both and get

$$x(s) = \sqrt{\epsilon\beta(s)}\cos(\phi(s) - \phi_0)\ ,\quad x'(s) = -\sqrt{\epsilon/\beta(s)}\sin(\phi(s) - \phi_0)\ .$$

For the two monitors the signals as a function of turns k are

$$x_1 = \sqrt{\epsilon\beta_s}\cos(\phi_1 + k2\pi Q)\ ,\quad x_2 = -\sqrt{\epsilon\beta_2}\sin(\phi_1) \propto x_1'\ .$$

In Fig. 41 the results of such an experiment done at SPEAR are shown [8]. On the left we see the signals from the beam being excited at three different amplitudes. At small amplitude the points lie on an ellipse which gets distorted at larger amplitudes due to the non-linearity of the sextupoles and the proximity of the 3rd order resonance. The right part shows the large amplitude case with better statistic.

3.5.2 Turn-by-turn measurement in all monitors — betatron phase advance

A betatron oscillation is excited and measured with many position monitors i around the ring, every revolution k. From this the phase and relative amplitude are obtained

$$x_{ik} = \frac{\hat{x}}{\sqrt{\beta_{x0}}}\sqrt{\beta_{xi}}\cos(2\pi Q_x k + \mu_{xi})\ ,\quad \frac{\beta_{x,i+1}}{\beta_{x,i}} = \left(\frac{\hat{x}_{i+1,k}}{\hat{x}_{i,k}}\right)^2\ ,$$

with β_{xi}, μ_{xi} being the beta function and phase at monitor i. A measurement of the betatron phase advance between adjacent monitors $\Delta\phi = \mu_{i+1} - \mu_i$ is related to the optical functions, Fig. 42. This

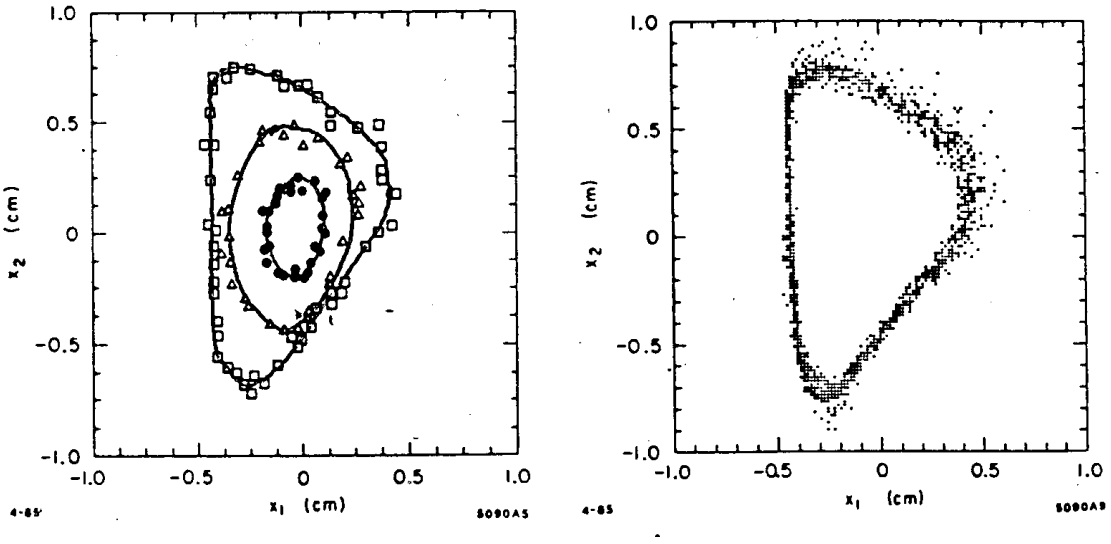

Fig. 41: Experimental tracking. Left: few turns at three different amplitudes; right: many turns at large amplitudes.

measurement has small systematic errors. The beta function itself is obtained from the amplitudes, [9]. Cable delays are not important since the bunch itself gives a timing signal.

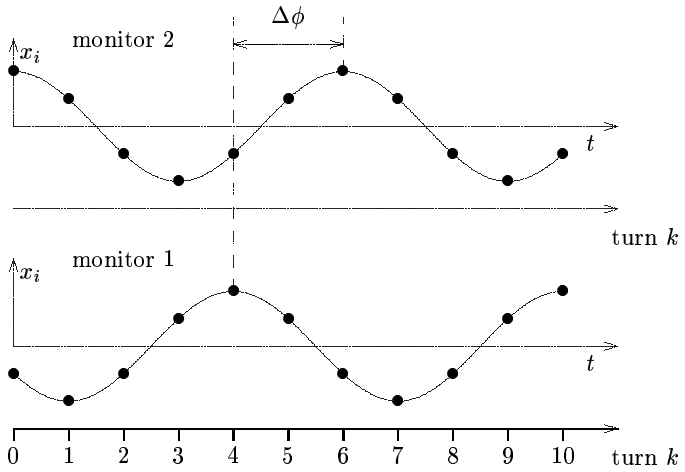

Fig. 42: Betatron phase measurement between two monitors

By measuring the betatron phase around the ring and comparing it with the calculated one, we can check the beam optics and find errors. A local focusing error creates a beating of the beta function and the betatron phase advance. This deviation goes at twice the betatron frequency, i.e., points being separated by $n\pi$ will keep this separation unless the error is located in between them, as illustrated in Fig. 43.

4 Longitudinal dynamics

4.1 Off-energy optics

A particle with positive deviation $\Delta p > 0$ is bent less in the dipoles; to get a closed orbit it moves further outside and obtains extra bending in the quadrupoles. This off-momentum equilibrium orbit has at a given location a radial distance Δx from the nominal equilibrium orbit and also has a different

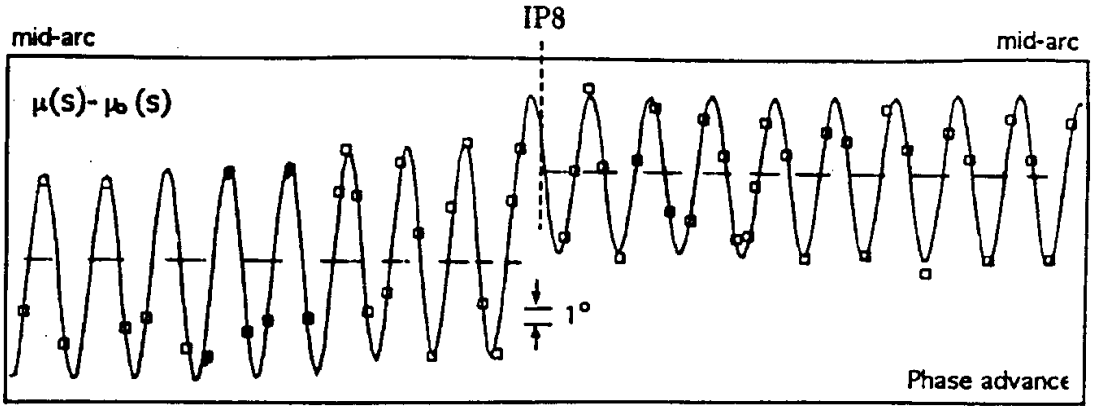

Fig. 43: Beta beating and phase jump at focusing error

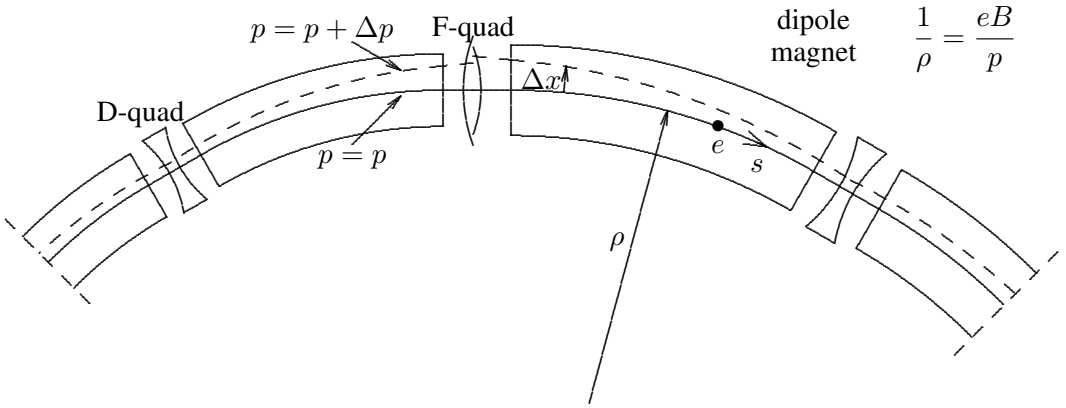

Fig. 44: Trajectory of a particle with a momentum deviation Δp

circumference, as shown in Fig. 44. In linear approximation both are proportional to $\Delta p/p$:

$$\Delta x = D_x \frac{\Delta p}{p} \ , \quad \frac{\Delta C}{C} = \alpha_c \frac{\Delta p}{p}$$

where the factor D_x is called dispersion. The relative change of circumference is given by the momentum compaction α_c which can by obtained from the dispersion to first order

$$\alpha_c = \frac{1}{C} \oint \frac{D_x(s)}{\rho} \mathrm{d}s \ .$$

The revolution time $T_0 = C/(\beta c)$ changes because the circumference as well as the particle velocity depend on momentum

$$\frac{\Delta T_0}{T_0} = \frac{\Delta C}{C} - \frac{\Delta \beta}{\beta} = \left(\alpha_c - \frac{1}{\gamma^2} \right) \frac{\Delta p}{p} = \eta_c \frac{\Delta p}{p} \ , \quad \text{with } \eta_c = \alpha_c - \frac{1}{\gamma^2} \ . \tag{8}$$

Here we introduced the abbreviation η_c, also called slippage factor; be careful: its sign definition is not uniform in the literature. The proportionality factors D_x, α_c, η_c for the deviations in orbit position, circumference, and revolution time with momentum deviation Δp have to be computed with a beam optics program.

Many rings, in particular electron machines, operate in an ultra-relativistic regime with $\beta \approx 1$, $\gamma \gg 1$ where we can use the trivial but useful relations between relative increments which allow

$$B_y \propto \frac{1}{2}(x^2 - y^2)\,, \quad B_x \propto xy$$
$$\frac{\mathrm{d}B_y}{\mathrm{d}x} = \propto x\,, \quad \frac{\mathrm{d}B_x}{\mathrm{d}y} \propto x$$

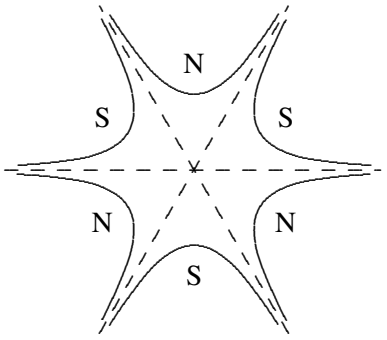

Fig. 45: Sextupole magnet and its field

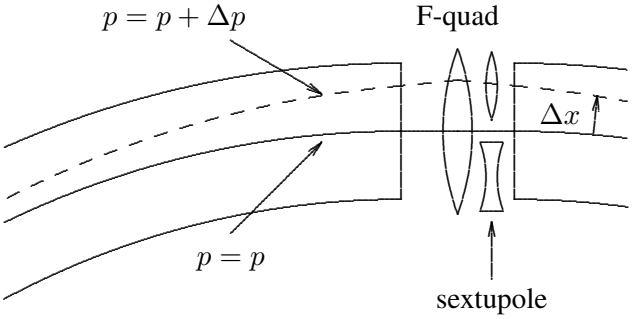

Fig. 46: Off-energy focusing correction with a sextupole at finite dispersion

one to simplify some expressions.

$$\text{From } \gamma = \frac{1}{\sqrt{1-\beta^2}}\,, \quad p = m_0 c\beta\gamma\,, \quad E = m_0 c^2 \gamma^2$$
$$\text{we get } \frac{\Delta\gamma}{\gamma} = \beta^2\gamma^2\frac{\Delta\beta}{\beta}\,, \quad \frac{\Delta(\beta\gamma)}{\beta\gamma} = \frac{\Delta p}{p} = \gamma^2\frac{\Delta\beta}{\beta} = \frac{1}{\beta^2}\frac{\Delta\gamma}{\gamma} = \frac{1}{\beta^2}\frac{\Delta E}{E}\,. \tag{9}$$

Most storage rings contain no vertical bending and have $D_y = 0$. However, tilt errors of quadrupole and dipole magnets can produce some residual vertical dispersion.

4.2 Off-energy transverse focusing

The focusing strength of a quadrupole depends on the momentum of the particle

$$\frac{1}{\rho} \propto \frac{1}{p} \rightarrow \frac{1}{f} \propto \frac{1}{p}\,.$$

As a result the tune depends on the momentum deviation, expressed as chromaticity

$$Q'_x = \frac{\Delta Q_x}{\Delta p/p}\,, \quad \xi_x = \frac{\Delta Q_x/Q_x}{\Delta p/p}\,.$$

This can be corrected with sextupole magnets, Fig. 45, located at finite dispersion, Fig. 46.

Sextupoles are non-linear elements which cannot be treated with simple matrices and which can limit the betatron amplitudes accepted by the ring, i.e., the dynamic aperture.

In the absence of sextupoles the horizontal and vertical chromaticities of a ring are always negative and called ‘natural chromaticities’. With the sextupoles these chromaticities are corrected to slightly positive values to avoid the head–tail instability.

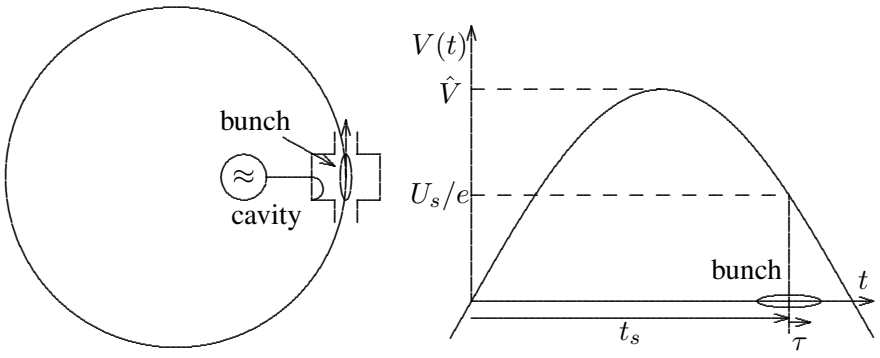

Fig. 47: RF system replaces energy loss and provides longitudinal focusing

4.3 Longitudinal focusing

The different circumference and velocity of an off-momentum particle change revolution time T_0 and revolution frequency ω_0 with a momentum deviation (8).

A cavity oscillating with voltage $\hat{V}$ and frequency $\omega_{\rm RF} = h\omega_0$, being a harmonic h of the nominal revolution frequency, replaces the energy U_s lost by a particle per turn due to synchrotron radiation or other effects and provides energy focusing, Fig. 47. A particle with excess energy has a longer revolution time and arrives at the cavity late when the voltage is small and vice versa.

4.3.1 Small synchrotron oscillations

We consider a particle with nominal momentum, energy, and revolution frequency p, E, ω_0 and an energy loss U_s per turn due to synchrotron radiation or other dissipative effect which might depend itself on the particle energy

$$U_s = U_{s0} + \frac{\partial U_s}{\partial E}\Delta E \, .$$

The energy loss or gain during one turn is

$$\begin{aligned}
\delta E &= e\hat{V}\sin(h\omega_0(t_s+\tau) - U_s \\
&\approx e\hat{V}\left(\sin\phi_s + \cos\phi_s h\omega_0\tau\right) - U_{s0} - \frac{\partial U_s}{\partial E}\Delta E \\
&= \omega_0 he\hat{V}\cos\phi_s\tau - \frac{\partial U_s}{\partial E}\Delta E \, . \\
\delta\tau &= \frac{\eta_c}{\beta^2}\frac{\Delta E}{E}T_0
\end{aligned}$$

where we used for $\Delta E = \tau = 0$ the equilibrium condition $e\hat{V}\sin\phi_s = U_0$. We call $\Delta E/E = \epsilon$ and approximate for continuous changes

$$\dot{\epsilon} = \frac{1}{E}\frac{{\rm d}E}{{\rm d}t} \approx \frac{1}{E}\frac{\delta E}{T_0} = \frac{\omega_0}{2\pi}\frac{\delta E}{E} \, , \quad \dot{\tau} \approx \frac{\delta\tau}{T_0} = \frac{\eta_c}{\beta^2}\epsilon \, ,$$

and get two first-order differential equations

$$\dot{\epsilon} = \omega_0^2\frac{he\hat{V}\cos\phi_s}{2\pi E_0}\tau - \frac{\omega_0}{2\pi}\frac{\partial U_s}{\partial E}\epsilon \, , \quad \dot{\tau} = \frac{\eta}{\beta^2}\epsilon \, ,$$

which are combined into one second-order equation

$$\ddot{\tau} + \frac{\omega_0}{2\pi}\frac{\partial U_s}{\partial E}\dot{\tau} - \omega_0^2\frac{\eta_c he\hat{V}\cos\phi_s}{2\pi\beta^2 E_0}\tau = \ddot{\tau} + 2\alpha_d\dot{\tau} + \omega_{s0}^2\tau = 0 \, ,$$

where we use the nominal synchrotron frequency ω_{s0} and the damping rate α_d

$$\omega_{s0} = \omega_0 \sqrt{\frac{\eta_c h e \hat{V} \cos\phi_s}{2\pi\beta^2 E_0}} \ , \quad \alpha_d = \frac{\omega_0}{4\pi} \frac{\partial U_s}{\partial E}$$

and get the solutions

$$\tau = \hat{\tau} \mathrm{e}^{-\alpha_d t} \sin(\omega_s t) \ , \quad \epsilon = \hat{\epsilon} \mathrm{e}^{-\alpha_d t} \cos(\omega_s t) \ , \quad \omega_s = \omega_{s0} \sqrt{1 - \alpha_d^2/\omega_{s0}^2} \approx \omega_{s0} \ .$$

To get a stable oscillation we need $\omega_{s0}^2 > 0$ which imposes a condition on the synchronous phase

$$E > E_T, \ \eta_c < 0 \ \rightarrow \cos\phi_s < 0 \ , \quad E < E_T, \ \eta_c > 0 \ \rightarrow \cos\phi_s > 0 \ .$$

For the oscillation to decay, the damping term has to be positive

$$\alpha_d = \frac{1}{2} \frac{\omega_0 \eta}{2\pi} \frac{\partial U_s}{\partial E} > 0 \ ,$$

giving the self-evident stability condition that the energy loss U_s has to increase for a positive energy deviation of the particle. Synchrotron radiation emits an instantaneous power $P_s \propto E^2 B^2$ which in nearly all cases fulfils the damping condition. However, in some ring lattices the dispersion is such that higher energy particles go through lower magnetic fields and actually lose less energy which can create growing oscillation. We exclude this here and assume that synchrotron oscillations are radiation damped.

The radiation is not emitted continuously but in quanta of finite energy. This process itself excites synchrotron oscillations which represent some noise and, together with the damping, leads to an equilibrium distribution that is usually Gaussian.

We shall investigate later the interaction between the beam and the impedance of the vacuum chamber. This can lead to an energy loss per turn which increases or decreases with an energy deviation and produces damping or an instability.

4.3.2 Longitudinal particle distribution

The damping, or growth, rate of synchrotron oscillation is usually much smaller than its frequency and can be neglected for shorter time scales, giving

$$\tau = \hat{\tau} \sin(\omega_s t) \ , \quad \epsilon = \hat{\epsilon} \cos(\omega_s t) \ , \quad \hat{\tau}\omega_s = \hat{\epsilon}\eta_s \ , \quad \omega_s \approx \omega_{s0} \ , \quad \beta \approx 1$$

in ultra-relativistic approximation. Neglecting the damping allows one to describe the synchrotron motion by an invariant Hamiltonian H and the corresponding canonical equation

$$H = \frac{\eta_c \epsilon^2}{2} + \frac{\omega_s^2 \tau^2}{2\eta_c} = \frac{\eta_c \hat{\epsilon}^2}{2} = \frac{\omega_s^2 \hat{\tau}^2}{2\eta_c} \ , \quad \frac{\partial H}{\partial \epsilon} = \eta_c \epsilon = \dot{\tau} \ , \quad \frac{\partial H}{\partial \tau} = \frac{\omega_s^2 \tau}{\eta_c} = -\dot{\epsilon} \ . \tag{10}$$

Other variables which are closely related to measurable RF parameter are convenient

$$\phi = h\omega_0 \tau \ , \quad \dot{\phi} = h\omega_0 \alpha_c \epsilon \ , \quad \hat{\dot{\phi}} = \omega_s \phi \ , \quad H_\phi = \frac{\dot{\phi}^2}{2} + \frac{\omega_s^2 \phi^2}{2} \ .$$

We use the invariant to study distributions. It can be shown [10] that any stationary phase-space distribution $\psi(\tau, \epsilon)$ is a direct function of the Hamiltonian and does not depend in an independent way on the individual coordinates.

The Gaussian distribution of electrons must be of the form $\psi(H) = \psi(\epsilon, \tau)$ with the observable projection line density $\lambda(\tau)$ or current $I(\tau)$ both being also Gaussian

$$\psi(\epsilon, \tau) = \frac{\mathrm{e}^{-H/\langle H' \rangle}}{2\pi\sigma_\epsilon\sigma_\tau} = \frac{1}{2\pi\sigma_\epsilon\sigma_\tau} \mathrm{e}^{-\frac{\epsilon^2 + \tau^2\omega_s^2/\eta_c^2}{2\sigma_\epsilon^2}} \ , \quad \langle H \rangle = \eta_c \sigma_\epsilon^2 = \omega_s^2 \sigma_\tau^2 / \eta_c$$

$$\lambda(\tau) = \int \psi(\tau,\, \epsilon)\mathrm{d}\epsilon = \frac{1}{\sqrt{2\pi}\sigma_\tau}\mathrm{e}^{-\frac{\tau^2}{2\sigma_\tau^2}} \;, \quad \int \lambda(\tau)\mathrm{d}\tau = 1$$
$$I(\tau) = N_b e\lambda(\tau) = \frac{N_b e}{\sqrt{2\pi}\sigma_\tau}\mathrm{e}^{-\frac{\tau^2}{2\sigma_\tau^2}} = \hat{I}\mathrm{e}^{-\frac{\tau^2}{2\sigma_\tau^2}}.$$

The current has the form of a Gaussian.

For a proton beam the effect of synchrotron radiation is negligible and the distribution is not given by a basic process. However, experimentally a so-called elliptic phase-space distribution is often observed, [11, 12]. This is probably due to the fact that this distribution can contain the maximum bunch intensity for a given area in the presence of space-charge effects. Since at low energy this effect is large, some beam might get lost leaving a bunch having this elliptic distribution. It is of the form

$$\psi(\tau, \epsilon) = C\sqrt{H_0 - H} \;, \quad H_0 = \frac{\omega_s \tau_0 \epsilon_0}{2} = \frac{\omega_s^2 \tau_0^2}{2\eta_c} \;,$$

with $H_0,\ \tau_0,\ \epsilon_0$ being maximum values for the Hamiltonian and the coordinates. The normalization determines the constant C, and integration over ϵ gives the line density or current of the single bunch with revolution frequency ω_0

$$\psi(\tau,\, \epsilon) = \frac{3}{4\pi\tau_0\epsilon_0}\sqrt{1 - \frac{\tau^2}{\tau_0^2} - \frac{\epsilon^2}{\epsilon_0^2}}$$
$$\lambda(\tau) = \int \psi(\tau,\, \epsilon)\mathrm{d}\epsilon = \frac{3}{4\tau_0}\left(1 - \frac{\tau^2}{\tau_0^2}\right) \;, \quad \int \lambda(\tau)\mathrm{d}\tau = 1$$
$$I(\tau) = N_b e\lambda(\tau) = \frac{3\pi\langle I\rangle}{2\omega_0\tau_0}\left(1 - \frac{\tau^2}{\tau_0^2}\right) \;, \quad \langle I\rangle = \frac{N_b e\omega_0}{2\pi}$$

where $\langle I\rangle$ is the average current of a single bunch having N_b particles. The current can be observed by a fast intensity monitor, it has the form of a parabola.

The above treatment can easily be extended to more general cases. The Hamiltonian (10) is based on a linear RF voltage. For a more general voltage it gets modified and the corresponding phase-space distribution and its projection can easily be obtained.

4.4 Energy calibration

4.4.1 Energy calibration on central orbit from known bending field

In all storage rings the energy of the beam should be known with some precision. It determines the spectrum of synchrotron radiation used for experiments at light sources and it enters in the analysis of particle or nuclear physics experiments. Special knowledge of the beam energy is demanded for synchrotron light sources used for optical calibration and colliding electron–positron rings producing narrow resonances.

For bunched beams and plane orbits the energy is determined by two conditions.

– The equilibrium orbit has to be closed and its local curvature is given by the magnetic field

$$\oint \frac{1}{\rho(s)}\mathrm{d}s = 2\pi \;, \quad \frac{1}{\rho} = \frac{eB_z}{p} \;.$$

– The revolution time $T = 2\pi/\omega_0$ has to be a multiple h of the RF period, giving the condition

$$h\omega_0 = \frac{h\beta c}{C_b} \;.$$

Usually one defines a nominal central orbit, going through the quadrupoles centres, with a circumference C_c. In this case the bending is exclusively given by the magnetic field of the dipole magnets.

If the beam circumference is different, $C_b \neq C_c$, the particles go off-centre through the quadrupoles and get some extra bending. To satisfy the closure condition the average beam energy adjusts itself, i.e., the injected particle executes an energy, or synchrotron, oscillation around the setting energy. This leads to an energy spread for protons but is damped by synchrotron radiation for electrons. To get the beam energy E_b, or momentum p_b, the integration over the magnetic field involves not only that of the dipoles but also that seen by the displaced beam in the quadrupoles which is difficult to track down.

It is best to first centre the beam, at least on average, in the quadrupoles by adjusting the RF frequency to get $C_b = C_c$. This process can be carried out by measuring the radial beam position in the dispersive regions using monitors which have the same centre as the quadrupoles, e.g., obtained by beam-based alignment. The beam motion due to changes in the quadrupole strengths can be observed and minimized by adjusting the RF frequency. However, this also leads to tune changes and can make the beam unstable. Sextupole magnets are often close to the quadrupoles and aligned to have the same magnetic centre. Measuring the tunes as a function of RF frequency for different sextupole strength can lead to a circumference which goes on average through the centres of the sextupoles, and to good approximation, of the quadrupoles in the dispersive region, [13]. This centring of the beam is quite demanding since a small error in circumference ΔC_b is related to a momentum error by the momentum compaction α_c

$$\frac{\Delta p}{p} = \frac{1}{\alpha_c}\frac{\Delta C_b}{C_c} = \frac{1}{\alpha_c}\frac{C_b - C_c}{C_c} \, .$$

Since $1/\alpha_c$ is a rather big number in a large and strongly focusing ring, this leads to an amplification of a circumference error.

Once we have a centred beam with $C_b = C_c$ we get the energy nearly exclusively from the field in the dipole bending magnets, however, corrector magnets, Earth field and some other fields should be considered. Bending magnets are measured and calibrated before installation. They can include some built-in probes to measure fields during operation or have an extra pilot magnet powered in series with the others and be always accessible for field observation.

4.4.2 Energy calibration from revolution frequencies of electrons and protons

In rare cases two different particles, e.g., electrons and protons, can be injected into a ring, not necessarily at the same time but on the same orbit. Centring both beams gives two RF frequencies

$$\omega_{\mathrm{RF}p} = h_p \omega_{0p} \, , \;\; \omega_{\mathrm{RF}e} = h_e \omega_{0e} \, .$$

Knowing the energy approximately we can find the two harmonic numbers h_e and h_p, which can be different, and get the two revolution frequencies. Having the same closed orbit with the same circumference C_c in the same magnetic field, their momenta must be the same but their revolution frequencies are different.

$$\frac{1}{\rho} = \frac{eB}{p} \, , \;\; p_p = m_p c \beta_p \gamma_p = p_e = m_e c \beta_e \gamma_e \, , \;\; \omega_{0p} = \frac{2\pi\beta_p c}{C_0} \, , \;\; \omega_{0e} = \frac{2\pi\beta_e c}{C_0} \approx \frac{2\pi}{C_0} \, ,$$

where we assumed that the electron is ultra-relativistic and approximated $\beta_e \approx 1$ in the relation between circumference and revolution frequency. By measuring ω_{0e} we get the circumference $C_c = 2\pi c/\omega_{0e}$ which we can substitute in the proton expression to get the normalized velocity

$$\beta_p = \frac{C_c \omega_{cp}}{2\pi c} = \frac{\omega_{cp}}{\omega_{0e}} \, .$$

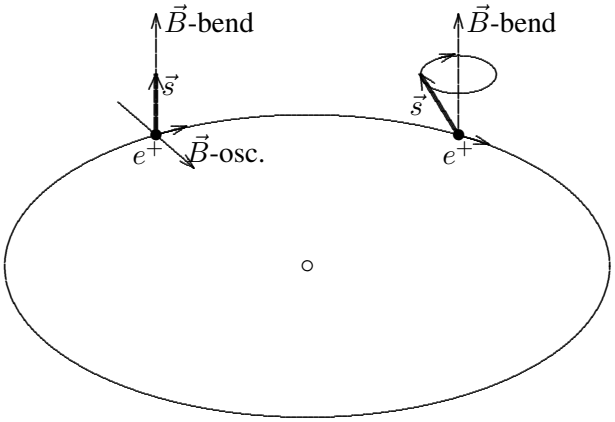

Fig. 48: Resonance depolarization of circulating positrons

By measuring the two revolution frequencies one gets β_p and $\gamma_p = 1/\sqrt{1-\beta_p^2}$ and finally

$$p_p = p_e = m_p c \frac{\beta_p}{\sqrt{1-\beta_p^2}} = m_p c \frac{\omega_{cp}/\omega_{ce}}{\sqrt{1-(\omega_{cp}/\omega_{0e})^2}} \; .$$

4.4.3 Energy calibration from depolarizing resonances

A positron has a spin $\vec{s}$ with angular momentum $J_e = \hbar/2\pi 2$, with $\hbar = 1.0546 \times 10^{-34}$ J s being Planck's number divided by 2π, and magnetic moment $\vec{\mu}_e = ge/(2m_e)\vec{s}$ with g being the normalized gyromagnetic ratio between the magnetic moment and the angular momentum of the electron spin. The magnetic field of the bending magnets applies a torque on this magnetic moment trying to align it, and the emitted synchrotron radiation leads to a polarization of the positron on a time scale between minutes or hours for small or large rings [14]. An electron has the same spin but its magnetic moment has the opposite direction with respect to it.

In order to obtain a polarized beam, field errors with horizontal components have to be avoided and the orbit should be well corrected. The degree of polarization is measured by Compton back scattering of circularly polarized light. For positrons and electrons with transverse polarization the scattered light shows an angular asymmetry. Once polarization is obtained, the spin vector $\vec{s}$ is in the vertical direction along the bending magnet field, Fig. 48. However, some local horizontal field can deflect the spin vector which starts to precess around the vertical axis with a frequency ω_p which is related to the revolution frequency ω_0 by the factor ν_p, called spin tune

$$\nu_p = \frac{\omega_p}{\omega_0} = \frac{g-2}{2}\gamma = 0.00115965\gamma = \frac{E}{0.44065 \text{ GeV}} \; .$$

This effect is used to get an absolute energy calibration involving only this natural constant g [15]. Such measurements can take some time, especially in large rings, and cannot be carried out often. In between, the orbit centring has to be checked and corrected regularly.

5 Longitudinal measurements

5.1 Overview

Like for the transverse case we list the longitudinal measurements in order of increasing sophistication. Starting with static conditions we progress to the observation of oscillations and finally to energy calibration, listed in Table 2. The last line mentions measurements specially useful in machines with continuous beams without bunches, these are not discussed here.

Table 2: Classes of longitudinal measurements

Conditions	Observation	Action
	position monitor, fast intensity monitors	RF modulation, change ring parameters
static, equilibrium conditions	momentum compaction, bunch length, energy aperture	adjust RF frequency, energy
dynamic, oscillations, turn by turn	synchrotron tunes, dispersion, dynamic energy aperture	excite longitudinal oscillations
excitation-response relation	harmonic excitation (longitudianl transfer function)	
excitation-response dependence	feed-back systems, synchrotron tune control, instabilities	

5.1.1 Instruments (passive)

– Beam position monitors can measure longitudinal beam properties at the location of a dispersion:

$$\Delta x = D_x \frac{\Delta p}{p} = D_x \frac{1}{\beta^2} \frac{\Delta E}{E} \ .$$

– Wideband intensity monitors can resolve the longitudinal bunch position, filling pattern and bunch length. A synchrotron oscillation represents a phase modulation of the intensity signal and leads to sidebands. The signal is observed on a fast scope or a spectrum analyser.

– The RF system in a ring can be used to excite synchrotron oscillations of the bunches. By making a phase modulation of the RF voltage at about the synchrotron oscillation frequency ω_s we excite a dipole mode oscillation. Correspondingly, an amplitude modulation at $2\omega_s$ produces a quadrupole oscillation.

– The beam energy can be changed by a variation of the RF frequency $\omega_{\mathrm{RF}} = h\omega_0$:

$$\frac{\Delta\omega_0}{\omega_0} = \frac{\Delta\omega_{\mathrm{RF}}}{\omega_{\mathrm{RF}}} = -\eta_c \frac{\Delta p}{p} = -\frac{\eta_c}{\beta^2} \frac{\Delta E}{E}$$

with $\eta_c = \alpha_c - 1/\gamma^2$ and α_c being the momentum compaction. Making a change in RF frequency $\Delta\omega_{\mathrm{RF}}$ we move the beam on an off-energy orbit and can measure dispersion D_x and chromaticity Q'.

– The energy can also be change by a variation of the dipole magnets keeping the beam on the central orbit where the quadrupoles do not contribute to the bending. For the ultra-relativistic case one keeps the RF frequency constant and gets

$$\frac{\Delta B_d}{B_d} = \frac{\Delta p}{p} = \frac{1}{\beta^2} \frac{\Delta E}{E} \ .$$

– A slow variation of the RF voltage V_{RF} changes the bunch length and the synchronous phase angle.

5.2 Observation of stationary bunches

5.2.1 Bunch filling pattern

A ring operates often with many bunches and their time and intensity distribution has to be checked. This can be done in time domain on a scope or in frequency domain by looking at the spectrum of a signal from an intensity monitor, Figs. 49 and 50. With one bunch in the ring we should see a line at each

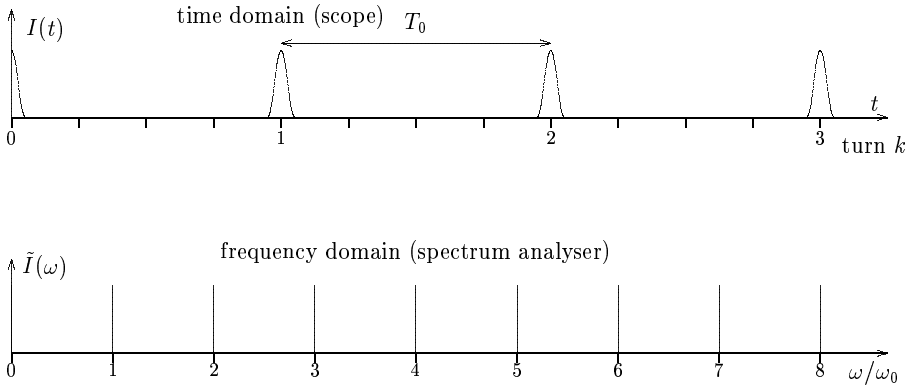

Fig. 49: Time domain signal and spectrum of a single bunch

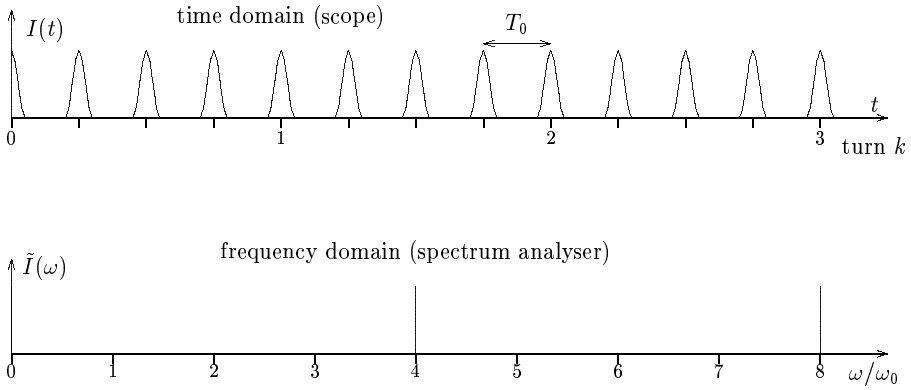

Fig. 50: Time signal and spectrum of four equidistant bunches

revolution frequency ω_0. The spectrum of four equidistant bunches of the same intensity gives lines with $4\omega_0$ spacing. Any other lines indicate a difference in current between bunches or an unequal spacing. For a wideband monitor the bunch length and the related spectrum can also be observed (Fig. 68).

As an application one checks in a collider that the e^- and e^+ bunches collide at the correct location. Intensity monitors at distance L on each side of the interaction point give both signals with $\Delta t = 2L/c$ spacing if the bunches collide correctly, Fig. 51.

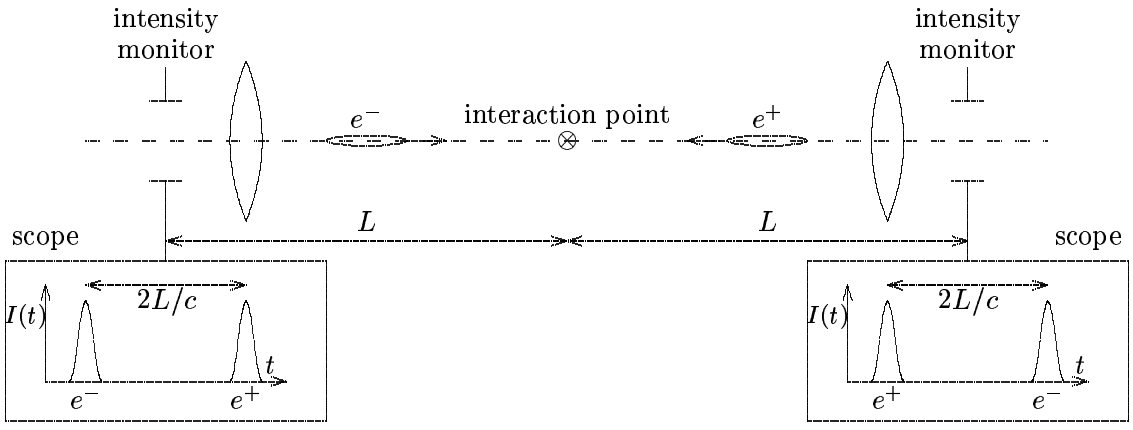

Fig. 51: Timing signals of colliding bunches

5.3 Energy change

5.3.1 Elements determining the energy

For some measurements (dispersion, chromaticity) we make a small change in the beam momentum or energy. The equilibrium beam energy E_b is given by two conditions:
The beam has to be on a closed orbit

$$\oint \frac{\mathrm{d}s}{\rho(s)} = 2\pi \text{ with } \frac{1}{\rho} = \frac{eB}{p_b} = \frac{eBc}{\beta E_b} .$$

For a bunched beam we have also the condition

$$\omega_{\mathrm{RF}} = h\omega_0 \text{ with } h = \text{ harmonic number (integer).}$$

To make a deviation $\Delta E = E_b - E$ in energy or $\Delta p = p_b - p$ in momentum we have two methods.

5.3.2 Keep focusing and bending magnet constant, change RF frequency

Changing the RF frequency moves the beam on a different orbit where it gets extra bending by the quadrupoles resulting in a momentum or energy change, Fig. 52

$$\frac{\Delta p}{p} = \frac{1}{\beta^2}\frac{\Delta E}{E} = \frac{1}{\eta_c}\frac{\Delta\omega_{\mathrm{RF}}}{\omega_{\mathrm{RF}}} .$$

This method is used to measure the dispersion and the corrected chromaticity.

5.3.3 Change dipole magnet strength

We can also change the energy by leaving all focusing elements constant and varying the dipole magnet field strength B_d, and keeping the beam on central orbit, Fig. 52

$$\frac{\Delta p}{p} = \frac{1}{\beta^2}\frac{\Delta E}{E} = \frac{\Delta B_d}{B_d} .$$

For an ultra-relativistic beam this is achieved to good approximation by keeping the RF frequency constant since the velocity change is negligible. For a more general case we have to make a slight change of the RF frequency

$$\frac{\Delta\omega_{\mathrm{RF}}}{\omega_{\mathrm{RF}}} \approx \frac{1}{\gamma^2}\frac{\Delta B}{B}$$

in order to stay on the central orbit. This method changes the energy but leaves the orbit and the focusing elements constant. It is used to measure the natural chromaticity.

5.4 Measurement of the dispersion

The dispersion gives the difference in equilibrium orbit for a change of energy

$$\Delta x = D_x\frac{\Delta p}{p} = \frac{D_x}{\beta^2}\frac{\Delta E}{E} , \quad \Delta y = D_y\frac{\Delta p}{p} = \frac{D_y}{\beta^2}\frac{\Delta E}{E} .$$

An energy change is made by a variation of the RF frequency

$$\frac{\Delta\omega_{\mathrm{RF}}}{\omega_{\mathrm{RF}}} = -\eta_c\frac{\Delta p}{p} = -\frac{\eta}{\beta^2}\frac{\Delta E}{E} \quad , \quad \eta_c = \alpha_c - 1/\gamma^2.$$

The closed orbit is measured for the two energies and the difference formed. This requires knowledge of η_c but no high accuracy is demanded. Most machines are designed to have no vertical dispersion. However, it is produced by coupling and magnetic errors and can be measured.

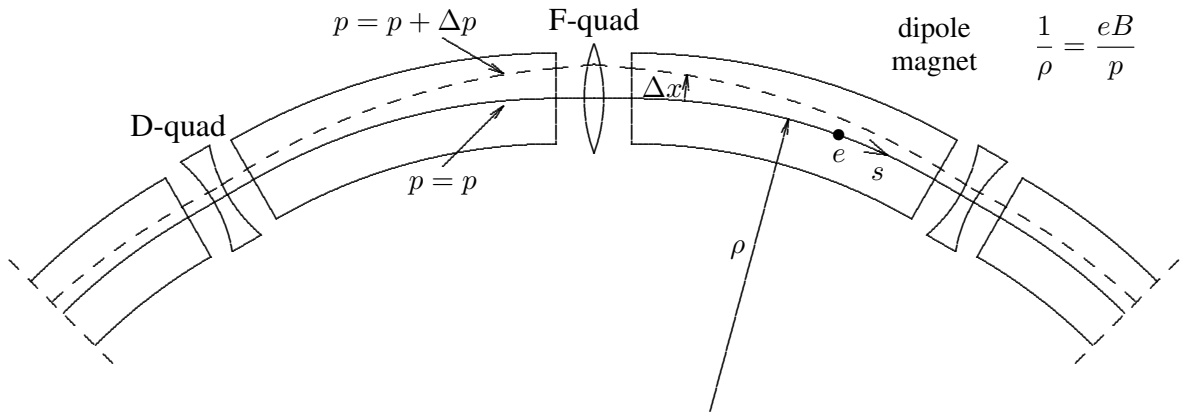

Fig. 52: Energy variation by a change of RF frequency — measure dispersion

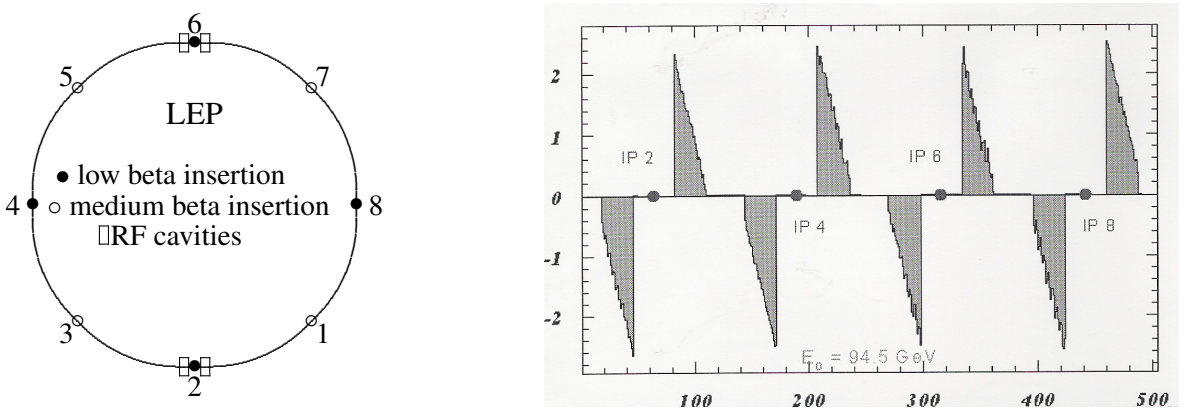

Fig. 53: Difference between electron and positron orbit in LEP showing the variation of energy between RF stations

If a closed orbit shows a distortion which follows approximately the shape of the dispersion, it is likely that the energy of the machine, i.e., the RF frequency is wrong. This should be adjusted before an orbit correction with the corrector magnets is attempted.

In an electron storage ring the particles lose energy due to synchrotron radiation which is replaced by the RF system. In large rings, like LEP, this loss can be relatively large between two RF stations. The particle will therefore come out of a cavity with an excess energy, will lose energy in the following bending magnets, and enter the next RF station with a lack of energy. At locations of finite dispersion the orbit is therefore displaced, spirals slowly towards the inside, and jumps outside after leaving the RF stations, it forms a 'sawtooth'. This can be measured directly, e.g., by taking the difference between the electron and positron orbit, for which the 'sawtooth' is opposite, [16]. This is shown in Fig. 53 for LEP.

5.4.1 Correction of the vertical dispersion

In a plane storage ring the vertical dispersion should vanish by design but some residual might be present due to errors and is best corrected at the source. Minimizing the betatron coupling will also reduce the vertical dispersion. Furthermore, experience shows that correcting the vertical orbit with many correctors of moderate strength leads to lower residual dispersion than the same orbit correction involving few strong correctors.

An orbit bump is only closed for the nominal momentum. A beam with a momentum deviation $\Delta p/p$ has a distorted orbit outside the bump which represents a dispersion, Fig. 54. By combining two orbit bumps we can make a closed dispersion bump. This is sometimes used to control the dispersion at

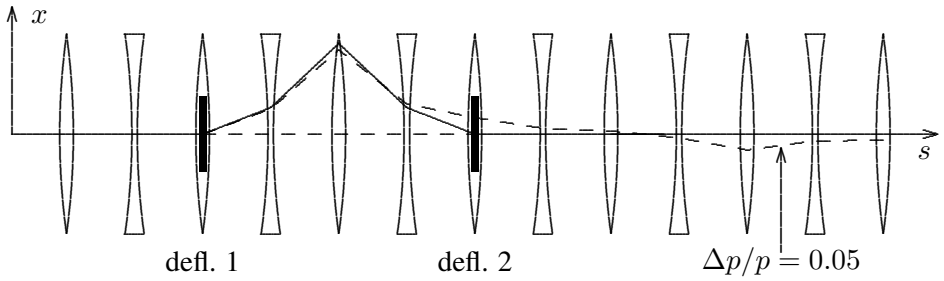

Fig. 54: Creating dispersion with a beam bump

the cavities to avoid synchro-betatron oscillations. This double bump can take up a large part of the ring.

5.4.2 Measuring synchronous phase and energy loss

The energy loss per turn U_s due to synchrotron radiation has to be compensated by the RF system. The bunch traverses the cavity at the synchronous phase angle ϕ_s and receives an energy gain

$$eV_{\mathrm{RF}} \sin \phi_s = U_{s0} \ .$$

To measure this phase we compare the cavity voltage with that induced by the bunch at ω_{RF} in an intensity monitor and determine the relative phase. Because of cable delays it would be very difficult to get an absolute phase measurement. However, changing the RF voltage results in a change in ϕ_s for a given U_s which can be measured. From the known voltage slope the energy loss U_s is obtained which determines ϕ_s, Fig. 55. The same experimental set-up can be used to measure energy loss caused by other effects like wall impedance, Fig. 70.

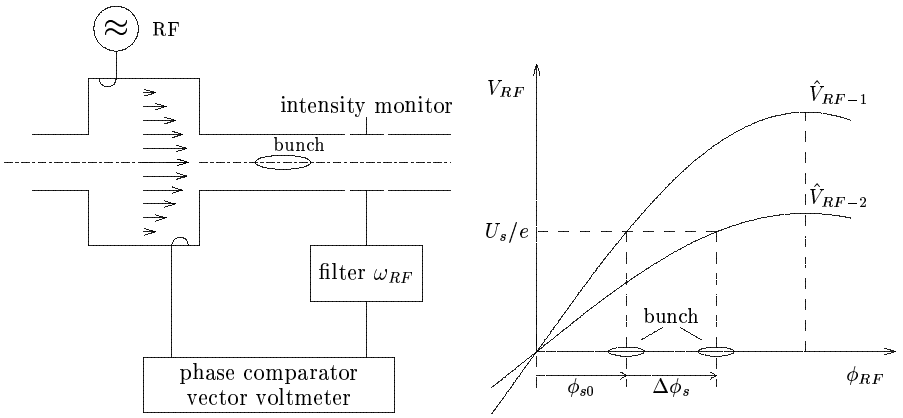

Fig. 55: Change of synchronous phase with RF voltage

5.5 Synchrotron oscillations

5.5.1 Exciting synchrotron oscillations and measuring their frequencies

The synchrotron frequency is

$$\omega_s = \omega_0 \sqrt{\frac{e\eta_c h V_{\mathrm{RF}} \cos \phi_s}{2\pi\beta^2 E}} \ , \quad \eta_c = \alpha_c - \frac{1}{\gamma^2} \ .$$

Its measurement can calibrate the RF voltage $V_{\rm RF}$ if the energy and the momentum compaction are known or determine α_c if $V_{\rm RF}$ and E are known.

Synchrotron oscillations are excited by injecting with the wrong energy or synchronous time t_s. At any time synchrotron oscillations can be excited by a phase modulation of the RF voltage with a frequency close to ω_s. The synchrotron frequency is best determined by varying the modulation frequency and observing the response either in time domain by direct observation of the bunches on a scope, or in frequency domain by observing the synchrotron sidebands of the revolution harmonics, as indicated on the left in Fig. 56. The mentioned excitation of a synchrotron oscillation leads to the coherent dipole mode $m = 1$, or rigid bunch mode in which all particles oscillate in phase. Other, higher, oscillation modes are also possible. For the quadrupole oscillation $m = 2$ the particles at the head and tail of the bunch oscillate with opposite phase. The bunch changes from being long with small energy spread to becoming short with large energy spread. This corresponds in phase-space to an ellipse rotating with ω_s. The period of this mode is only half of the dipole mode, its frequency is therefore $\omega_2 = 2\omega_1 = 2\omega_s$ and gives the corresponding sidebands. This mode is shown on the right of the figure and is excited by an amplitude modulation of the RF voltage, or by the injection of a mismatched bunch, having the wrong ratio between bunch length and energy spread.

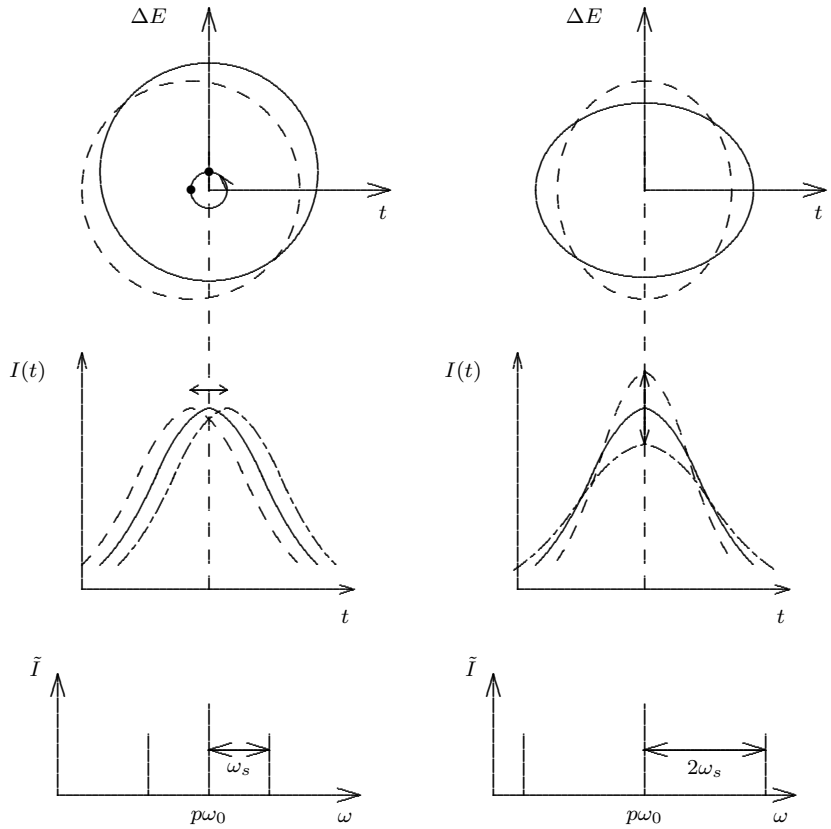

Fig. 56: Dipole and quadrupole oscillations: phase-space bunch current vs. time and spectrum

5.5.2 Measuring energy acceptance

To measure the energy acceptance we can make an adiabatic energy change either by varying the RF frequency (static acceptance) or by exciting a synchrotron oscillation of large amplitude (dynamic acceptance). In both cases the energy deviation is increased until the life time is short. One must check whether this is caused by a physical limitation at finite dispersion, by a tune change moving into a resonance, or a more general limitation. The accurate measurement of the energy change made is difficult. It

can be determined at a location of large dispersion with a scraper or a position monitor.

5.6 Measuring chromaticity

5.6.1 Chromaticity and its correction

The focusing strength of a quadrupole depends on the momentum of the particle. As a result the tune depends on the momentum deviation, expressed as chromaticity

$$Q'_x = \frac{\Delta Q_x}{\Delta p/p} \ , \ \ \xi_x = \frac{\Delta Q_x/Q_x}{\Delta p/p} \ .$$

This can be corrected with sextupole magnets located at finite dispersion as shown in Fig. 46. In the absence of sextupoles the horizontal and vertical chromaticities of a ring are always negative and called 'natural chromaticities'. With the sextupoles these chromaticities are usually corrected to slightly positive values in order to avoid the head–tail instability.

5.6.2 Measure corrected chromaticity

The chromaticity including the contribution by the sextupoles, called corrected chromaticity, is of major interest and used to adjust the powering of these magnets. For this the momentum change is achieved by a change of the RF frequency $\omega_{\rm RF} = h\omega_0$ which moves the beam radially at places of finite dispersion D_x, in particular at the sextupoles which correct the focusing dependence on momentum of the quadrupoles

$$\frac{\Delta p}{p} = -\frac{1}{\eta_c}\frac{\Delta\omega_0}{\omega_0} \ , \ \ Q' = -\frac{\Delta Q_x \eta_c}{\Delta\omega_{\rm RF}/\omega_{\rm RF}} \ .$$

This simulates the condition of an energy change which also results in a transverse motion at finite dispersion, in particular at the sextupoles, as is the case during a synchrotron oscillation. An example of such a measurement done at LEP [17] is shown in Fig. 57.

Continuous Q' measurement during energy ramping is of interest. It can be done by modulating the RF frequency in time and observing the resulting tune changes.

5.6.3 Measure uncorrected chromaticity

This parameter is of less interest except as a difference from the corrected one to check the effect of the sextupoles. In small machines it can easily be measured by turning the sextupoles off and repeating the above measurement involving a change of RF frequency.

However, large machines often have a short life time due to the tune spread in the absence of a chromatic correction. In this case quadrupoles and sextupoles stay on their nominal level and the energy is varied by changing the field B_D of the dipole bending magnets only as mentioned before. Assuming an ultra-relativistic approximation we keep the RF frequency constant. The resulting momentum change is

$$\frac{\Delta p}{p} = \frac{\Delta B_D}{B_D} \ .$$

In this case the beam has no radial movement and goes through the centre of the sextupoles where they have no effect [18]. An example of such a measurement is shown in Fig. 58.

5.6.4 Chromatic phase advance

Measuring the betatron phase advance for different energy deviations gives the chromatic phase advance (local chromaticity) which advances at locations of sextupoles (arcs) but lags at places of strong focusing (low-beta insertions), as shown in Fig. 59 for LEP. The detailed chromatic phase advance shows some beta beating since for an off-energy particle the optics is not matched everywhere but only at some strategic locations like the interaction point in a collider [17].

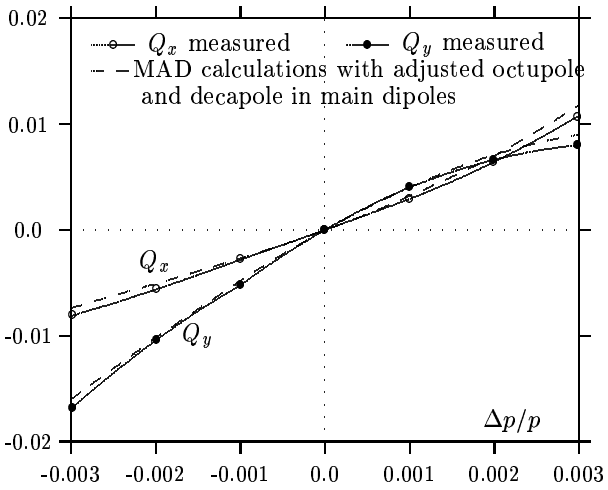

Fig. 57: Measured and calculated tunes vs. momentum in LEP

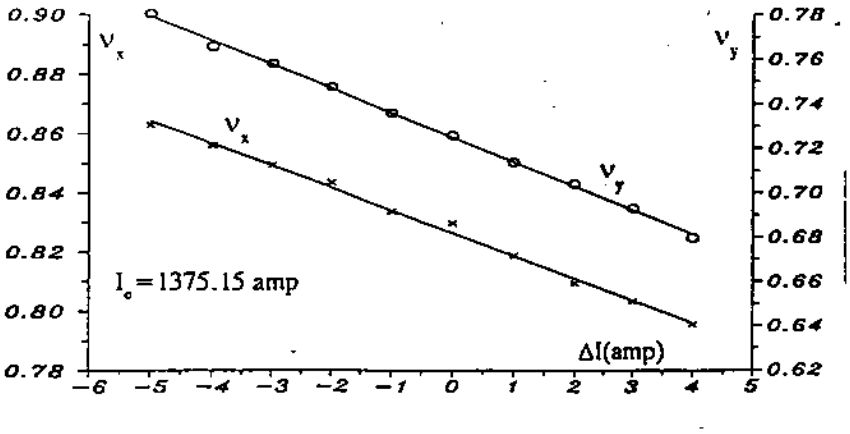

Fig. 58: Uncorrected Q' measurement in SPEAR (H. Wiedemann)

5.7 Energy calibration in the electron–positron collider LEP

One of the main purposes of this ring was the production and investigation of the Z^0 boson through the reaction

$$e^- + e^+ \rightarrow Z^0$$

which has an energy of about 91.6 GeV. The cross section of this reaction was measured by observing the production rate of Z^0 per unit luminosity as a function of the beam energy. This scan through this particle determines its central energy and width for which an accurate knowledge of the beam energy is essential.

Before the energy calibration with depolarization resonance one centres the beam as well as possible on the axes of the quadrupoles and sextupoles which are mounted together and have the same magnetic centre. The tunes were measured as a function of RF frequency which represents actually a chromaticity measurement [13]. This was repeated for different sextupole settings and shown in Fig. 60. At the crossing of the lines the sextupoles do not affect the tune which indicates that the beam goes through their centres.

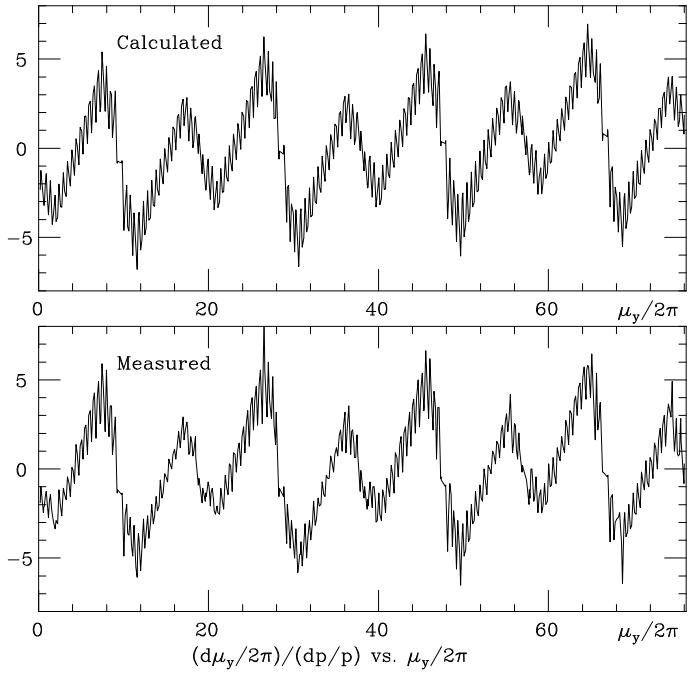

Fig. 59: Chromatic phase advance $d\mu_y/(dp/p)$

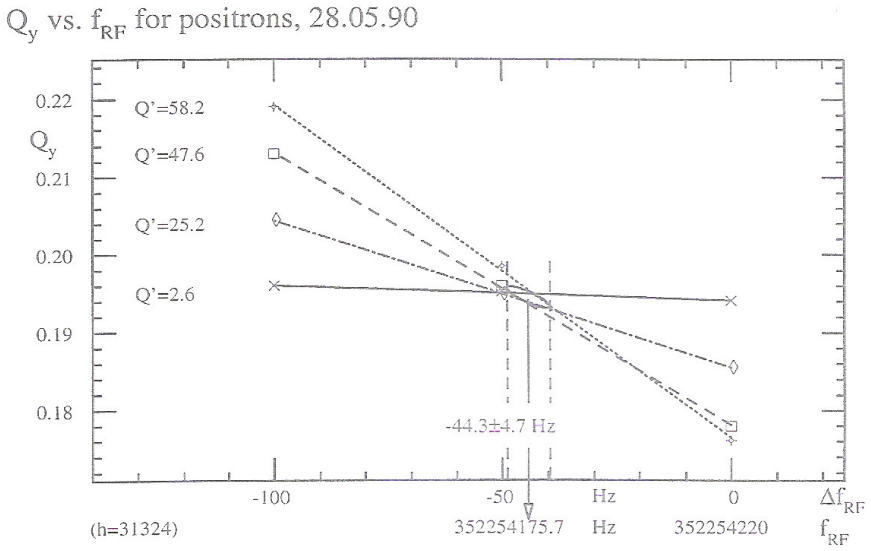

Fig. 60: Centring the beam in the sextupoles

The absolute energy calibration was carried out regularly using depolarizing resonances, described in an ealier section, but the orbit was centred in between in shorter intervals to keep the calibration. To get polarized beams the vertical orbit had to be corrected down to a very small residual distortion. The angular asymmetry of gamma ray photons obtained by Compton back scattering of circularly polarized visible light gave the degree of polarization. In Fig. 61 a series of several such energy calibrations are shown, which were carried out over a time span of about a day without centring the orbit. During this time the Earth undergoes a small vertical deformation of about 0.3 m due to the tidal forces created by the Moon and the Sun. This gives also a lateral strain changing the LEP circumference of 27 km by about

1 mm. The relation between relative energy and circumference involves the momentum compaction, $\alpha_c \approx 2 \cdot 10^{-4}$ for LEP,

$$\frac{\Delta E}{E} = \frac{1}{\alpha_c \beta^2} \frac{C_b - C_0}{C_0} \approx 5000 \frac{C_b - C_0}{C_0}$$

which leads to a large amplification of the circumference deviation resulting in an energy change of $\approx 2 \cdot 10^{-4}$ which is more than could be tolerated. In Fig. 61 the energy measured by resonant depolarization is plotted over the time of the experiment and compared with the one calculated from a table of tides [19]. The good agreement indicates the sensitivity and precision of this method of energy measurement. For the analysis of the physics experiment the energy variation due to the tides had to be corrected for.

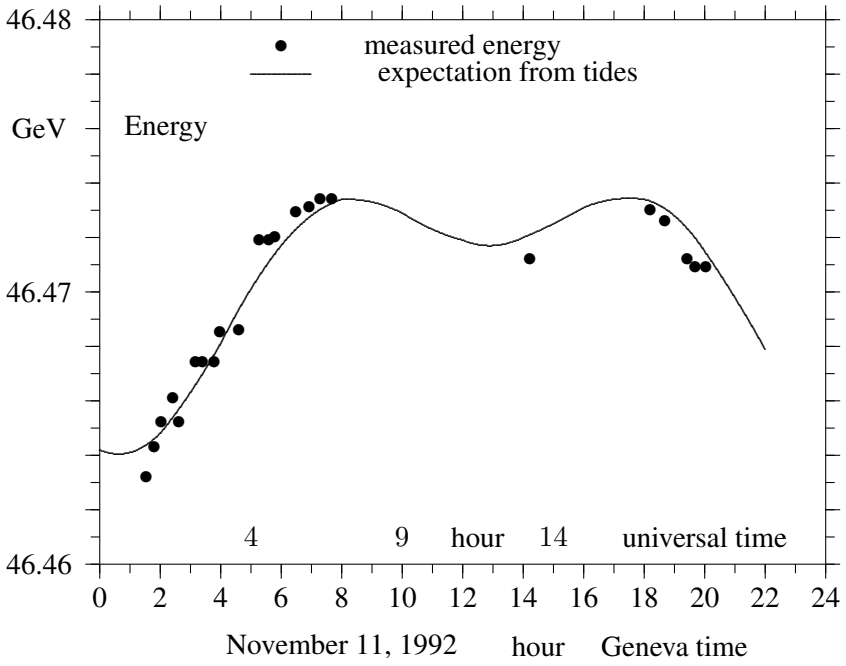

Fig. 61: Energy variation in LEP due to the circumference change by the Earth tides

6 Collective effects — instabilities

6.1 Introduction

The motion of a single particle in a storage ring is determined by the external guide fields created by the dipole and quadrupole magnets and the RF system, as well as by initial conditions and synchrotron radiation. The many particles contained in a high-intensity beam represent a sizeable charge and current which act as sources of electromagnetic fields called *self-fields*. They are modified by the boundary conditions imposed by the beam surroundings (vacuum chambers, cavities, etc.) and act back on the beam. This can lead to a *frequency shift* (change of the betatron or synchrotron frequency), to an increase of a small initial disturbance, an *instability*, or a *change of the particle distribution*, e.g., bunch lengthening. These phenomena are called *collective effects* since they are caused by a common action of the many particles in the beam.

As an introductory example we consider a bunch circulating in a storage ring and going through a passive cavity where it induces electromagnetic fields, Fig. 62. These fields oscillate and decay slowly. In the next turn the bunch might find some field left, having a phase such that a small initial synchrotron oscillation amplitude is increased, leading to an exponentially growing instability.

In most cases the fields created by the beam are small compared to the guide fields, and their effects can be treated as a *perturbation*. This is done in three steps:

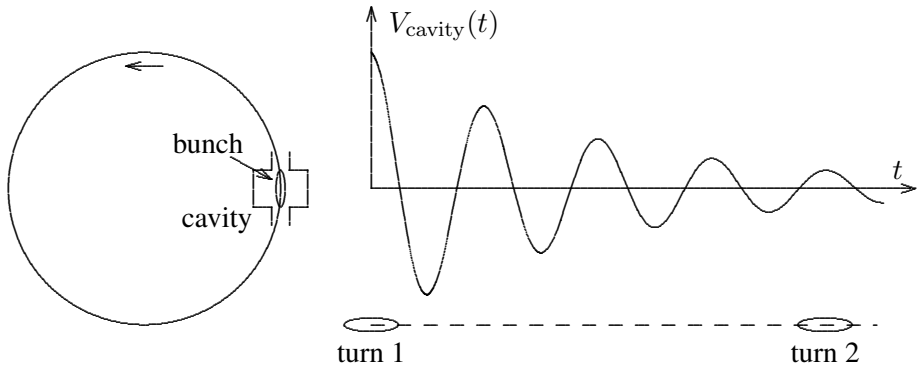

Fig. 62: Induced field acting on the bunch the next turn

– First, the motion in the guide field and the stationary particle distribution are established.
– A small disturbance of the bunch from its stationary motion is considered (betatron or synchrotron oscillation). The fields caused by this disturbance are determined taking the boundary condition imposed by the beam surroundings (impedance) into account.
– The effect of these fields on the initial disturbance is investigated. If its amplitude is increased we have an *instability*, if it is decreased we have *damping*, or, if the frequency of the oscillation mode is changed, we have a *frequency shift*.

For the case of small self-fields, considered here, the particle distribution in the bunch is given by external conditions (machine parameter, initial condition, synchrotron radiation) and is usually Gaussian in electron machines. As disturbances of the stationary distribution we consider some modes of oscillation which are orthogonal (independent of each other) and investigate their stability.

Strong self-fields, however, modify the particle distribution and also the modes of oscillation, such that they are no longer independent. A self-consistent solution has to be found, which is usually only attempted for the case of bunch lengthening.

We distinguish between *single* and *multi-traversal* collective effects. For the first kind no memory of the induced field over the time interval between the bunch passages is required. An example of a single-traversal effect is bunch lengthening. Multi-traversal effects need a memory to make an interaction between bunches or turns possible. This can be provided by cavity-like objects with a large quality factor Q, meaning narrow-band resonances.

Finally, we distinguish between *longitudinal* effects involving synchrotron oscillations and longitudinal impedances, and *transverse* effects involving betatron oscillations and transverse impedances. In both cases the longitudinal particle distribution (bunch length) is important, because it can be 'resolved' by the impedance, while the transverse distribution is usually not resolved and does not affect the instability.

The most important longitudinal single traversal effects are synchrotron frequency shifts and bunch lengthening. In the transverse case the effect of the chromaticity is important which can lead to head–tail instabilities.

6.2 Impedances, wakes, and longitudinal dynamics

Impedances and wake potentials are treated extensively in the literature, e.g., Ref. [20]. We illustrate here some of their essential properties based on the simple example of a cavity resonance.

Cavity-like devices are the most important objects which can cause coupled-bunch mode instabilities, because the induced fields oscillate for a relatively long time and provide a memory over the time interval between bunch passages. Such a cavity resonance resembles an RLC circuit as shown in

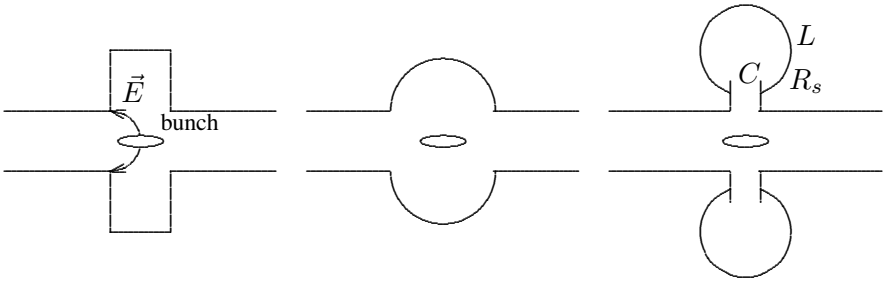

Fig. 63: Cavity resembling an RLC circuit

Fig. 63, and can be treated as such. The RLC circuit has a shunt impedance R_s, an inductance L, and a capacitance C, Fig. 64. In a real cavity these three parameters cannot be separated easily. For this reason we use some other related parameters which can be measured directly: The *resonance frequency* ω_r, the *quality factor* Q and the *damping rate* α:

$$\omega_\mathrm{r} = \frac{1}{\sqrt{LC}}\,,\quad Q = R_s\sqrt{\frac{C}{L}} = \frac{R_s}{L\omega_\mathrm{r}} = R_s C\omega_\mathrm{r}\,,\quad \alpha = \frac{\omega_\mathrm{r}}{2Q}\,,\quad C = \frac{Q}{\omega_\mathrm{r}R_s}\,,\quad L = \frac{R_s}{\omega_\mathrm{r}Q}\,.$$

If this circuit is driven by a current I the voltages across each element are

$$V_R = I_R R_s\,,\quad V_C = \frac{1}{C}\int_0^t I_C \mathrm{d}t\,,\quad V_L = L\frac{\mathrm{d}I_L}{\mathrm{d}t}$$

and have the relations

$$V_R = V_C = V_L = V\,,\quad I_R + I_C + I_L = I\,.$$

Differentiating with respect to t gives

$$\dot{I} = \dot{I}_R + \dot{I}_C + \dot{I}_L = \frac{\dot{V}}{R_s} + C\ddot{V} + \frac{V}{L}\,.$$

Using $L = R_s/(\omega_r Q)$ and $C = Q/(\omega_r R_s)$ gives the differential equation

$$\ddot{V} + \frac{\omega_r}{Q}\dot{V} + \omega_\mathrm{r}^2 V = \frac{\omega_r R_s}{Q}\dot{I}\,.$$

The solution of the homogeneous equation is a damped oscillation

$$V(t) = \mathrm{e}^{-\alpha \mathrm{t}}\left(\mathrm{A}\cos\left(\omega_\mathrm{r}\sqrt{1-\frac{1}{4\mathrm{Q}^2}}\,\mathrm{t}\right) + \mathrm{B}\sin\left(\omega_\mathrm{r}\sqrt{1-\frac{1}{4\mathrm{Q}^2}}\,\mathrm{t}\right)\right)\,. \tag{11}$$

6.2.1 Wake potential

We now calculate the response of the RLC circuit shown in Fig. 64, representing a cavity resonance, to a delta function pulse (very short bunch)

$$I(t) = q\delta(t).$$

The charge q induces a voltage in the capacitance

$$V(0^+) = \frac{q}{C} = \frac{\omega_r R_s}{Q}q\,.$$

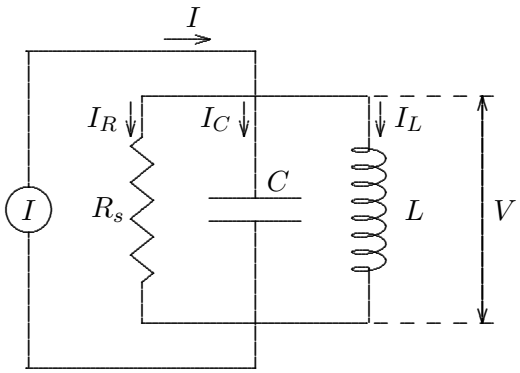

$$V_R = I_R R_s$$
$$V_C = \frac{1}{C}\int I_C \mathrm{d}t$$
$$V_L = L\frac{\mathrm{d}I_L}{\mathrm{d}t}$$

Fig. 64: RLC circuit equivalent to a cavity resonance

The resulting energy stored in the capacitance

$$U = \frac{q^2}{2C} = \frac{\omega_r R_s}{2Q}q^2 = \frac{V(0^+)}{2}q = k_{pm0}q^2,$$

must be equal to the energy lost by the charge. Here we introduce the *parasitic mode loss factor* for a point charge

$$k_{pm0} = \frac{U}{q^2} = \frac{\omega_r R_s}{2Q}$$

which is the energy loss normalized for the charge q. The capacitance C will discharge first through the resistor R_s and then also through the inductance L

$$\dot{V}(0^+) = -\frac{\dot{q}}{C} = -\frac{I_R}{C} = -\frac{1}{C}\frac{V(0^+)}{R_s} = -\frac{\omega_r^2 R_s}{Q^2}q = -\frac{2\omega_r k_{pm0}}{Q}q\,.$$

The voltage in this resonance circuit now has the initial conditions

$$V(0^+) = 2k_{pm0}q \quad \text{and} \quad \dot{V}(0^+) = \frac{2\omega_r k_{pm0}}{Q}q\,,$$

which determine the constants of the homogeneous solution (11) giving the voltage in a resonator circuit excited at the time $t = 0$ by a δ-pulse $I(t) = q\delta t$, which we normalize by the charge q

$$G(t) = \frac{V(t)}{q} = 2k_{pm0}\mathrm{e}^{-\alpha t}\left(\cos\left(\omega_r\sqrt{1-\frac{1}{4Q^2}}\;t\right) - \frac{\sin\left(\omega_r\sqrt{1-\frac{1}{4Q^2}}\;t\right)}{2Q\sqrt{1-\frac{1}{4Q^2}}}\right)\,.$$

This voltage induced by charge q at $t = 0$ is seen by a second point charge q' traversing the cavity at t and losing or gaining an energy $U = q'V(t) = qq'G(t)$ as shown in Fig. 65. This energy gain/loss per unit source and probe charges is called point charge *wake potential* or *Green function* $G(t)$. For a high quality factor, $Q \gg 1$, this simplifies to

$$G(t) \approx 2k_{pm0}\mathrm{e}^{-\alpha \mathrm{t}}\cos\left(\omega_\mathrm{r}\mathrm{t}\right)\,.$$

The wake potential is related to the longitudinal field E_z by a field integral over the object length. Since the field changes during the traversal, this integration has to follow a particle going with nearly the speed of light through the object and taking the momentary field value

$$V = -\int_{z_1}^{z_2} E_z(z,t)\mathrm{d}z = -f_t\int_{z_1}^{z_2} E_z(z)\mathrm{d}z = -\langle E_z\rangle_t \Delta z\,,$$

with the transit time factor f_t correcting the instantaneous integral over z. We use a wake potential that is positive where the particle loses energy consistent with the sign used for resistors.

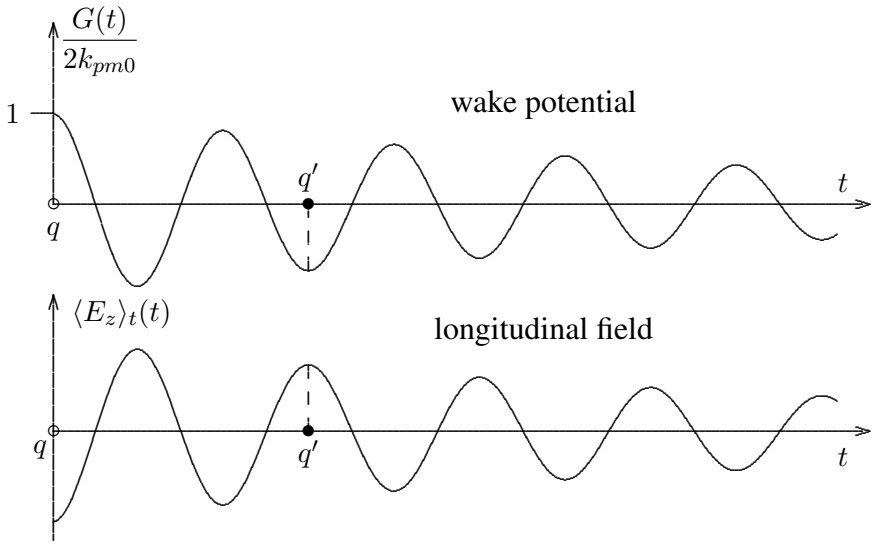

Fig. 65: Wake potential and longitudinal field

6.2.2 Impedance

We now use a *harmonic* excitation of the circuit in Fig. 64 with a current $I = \hat{I}\cos(\omega t)$ which is described by the differential equation

$$\ddot{V} + \frac{\omega_r}{Q}\dot{V} + \omega_r^2 V = -\frac{\omega_r R_s}{Q}\hat{I}\omega\sin(\omega t)\ .$$

The solution of the homogeneous equation is a damped oscillation which disappears after some transient time and we are left with the particular solution of the form $V(t) = A\cos(\omega t) + B\sin(\omega t)$. Inserting this into the differential equation and separating cosine and sine terms gives

$$(\omega_r^2 - \omega^2)A + \frac{\omega_r\omega}{Q}B = 0 \quad \text{and} \quad (\omega_r^2 - \omega^2)B - \frac{\omega_r\omega}{Q}A = -\frac{\omega_r\omega R_s}{Q}\hat{I}\ .$$

The voltage induced by the harmonic excitation of the resonator becomes

$$V(t) = \hat{I}R_s\frac{\cos(\omega t) - Q\frac{\omega_r^2-\omega^2}{\omega_r\omega}\sin(\omega t)}{1 - Q^2\left(\frac{\omega^2-\omega_r^2}{\omega_r\omega}\right)^2}\ .$$

This voltage has a cosine term which is *in phase* with the exciting current. It can absorb energy and is called the *resistive* term. The sine term of the voltage is *out of phase* with the exciting current and does not absorb energy, it is called the *reactive* term. The ratio between the voltage and current is called *impedance*. It is a *function of frequency* ω and has a resistive part $Z_{\rm r}(\omega)$ and a reactive part $Z_{\rm i}(\omega)$

$$Z_{\rm r}(\omega) = R_s\frac{1}{1 + Q^2\left(\frac{\omega_r^2-\omega^2}{\omega_r\omega}\right)^2}\ ,\quad Z_{\rm i}(\omega) = R_s\frac{Q\frac{\omega_r^2-\omega^2}{\omega_r\omega}}{1 + Q^2\left(\frac{\omega_r^2-\omega^2}{\omega_r\omega}\right)^2}\ .$$

The resonance can be excited either by a current $I(t) = \hat{I}\cos(\omega t)$ or $I(t) = \hat{I}\sin(\omega t)$ resulting in the voltages $V(t)$

$$\begin{aligned} I(t) = \hat{I}\cos(\omega t) \ &\rightarrow\ V(t) = \hat{I}\left(Z_{\rm r}(\omega)\cos(\omega t) - Z_{\rm i}(\omega)\sin(\omega t)\right)\ , \\ I(t) = \hat{I}\sin(\omega t) \ &\rightarrow\ V(t) = \hat{I}\left(Z_{\rm r}(\omega)\sin(\omega t) + Z_{\rm i}(\omega)\cos(\omega t)\right)\ . \end{aligned}$$

6.2.3 Complex notation

We used a harmonic excitation of the form

$$I(t) = \hat{I}\cos(\omega t) = \hat{I}\frac{\mathrm{e}^{j\omega t} + \mathrm{e}^{-j\omega t}}{2} \quad \text{with} \quad 0 \le \omega \le \infty \,,$$

using positive frequencies only. A complex notation

$$I(t) = \hat{I}\mathrm{e}^{j\omega t}/2 \quad \text{with} \quad -\infty \le \omega \le \infty$$

involving positive and negative frequencies leads to more compact expressions and is often convenient. The real solution can be obtained after, by taking half the sum of the solutions for $\hat{I}\mathrm{e}^{\pm\omega t}$. We take the differential equation

$$\ddot{V} + \frac{\omega_r}{Q}\dot{V} + \omega_r^2 = \frac{\omega_r R_s}{Q}\dot{I}$$

of the resonator voltage with the excitation $I(t) = \hat{I}\exp(j\omega t)$ and seek a solution of the form $V(t) = V_0\exp(j\omega t)$, where V_0 is in general complex and get

$$-\omega^2 V_0\mathrm{e}^{j\omega t} + j\frac{\omega_r\omega}{Q}V_0\mathrm{e}^{j\omega t} + \omega_r^2 V_0\mathrm{e}^{j\omega t} = j\frac{\omega_r\omega R_s}{Q}\hat{I}\mathrm{e}^{j\omega t} \,.$$

The impedance, defined as the ratio V/I, is given by

$$Z(\omega) = \frac{V_0}{\hat{I}} = R_s\frac{j\frac{\omega_r\omega}{Q}}{\omega_r^2 - \omega^2 + jQ\frac{\omega_r\omega}{Q}} = R_s\frac{1 - jQ\frac{\omega^2-\omega_r^2}{\omega\omega_r}}{1 + Q^2\left(\frac{\omega^2-\omega_r^2}{\omega\omega_r}\right)^2} = Z_\mathrm{r}(\omega) + jZ_\mathrm{i}(\omega)$$

and has a real and an imaginary part. For a large quality factor Q the impedance is only large for $\omega \approx \omega_r$ or $|\omega - \omega_r|/\omega_r = |\Delta\omega|/\omega_r \ll 1$ and can be simplified:

$$Z(\omega) \approx R_s\frac{1 - j2Q\frac{\Delta\omega}{\omega_r}}{1 + 4Q^2\left(\frac{\Delta\omega}{\omega_r}\right)^2} \,.$$

The resonator impedance has some specific properties:

$$\begin{aligned} \omega \;&= \omega_r \;\rightarrow\; Z_\mathrm{r}(\omega_r) \text{ has a maximum while } Z_\mathrm{i}(\omega_r) = 0 \\ |\omega| &< \omega_r \;\rightarrow\; Z_\mathrm{i}(\omega) > 0 \text{ (inductive)} \\ |\omega| &> \omega_r \;\rightarrow\; Z_\mathrm{i}(\omega) < 0 \text{ (capacitive)} \end{aligned} \tag{12}$$

and some properties which apply to any impedance or wake potential:

$$Z_\mathrm{r}(\omega) = Z_\mathrm{r}(-\omega) \;,\;\; Z_\mathrm{i}(\omega) = -Z_\mathrm{i}(-\omega) \,,$$

$$Z(\omega) = \int_{-\infty}^{\infty} G(t)\mathrm{e}^{-j\omega t}\mathrm{d}t \;,\;\; G(t) = \frac{1}{2\pi}\int_{-\infty}^{\infty} Z(\omega)\mathrm{e}^{j\omega t}\mathrm{d}\omega \,, \tag{13}$$

$$t < 0, \;\rightarrow\; G(t) = 0 \text{ no fields before particle arrives} \,. \tag{14}$$

Impedance and Green function are related by a Fourier transform with a factor unity or $1/(2\pi)$ in front of the integral instead of the factor $1/\sqrt{2\pi}$ used elsewhere. Be careful: sometimes one uses $I(t) = \hat{I}\mathrm{e}^{-i\omega t}$ instead of $I(t) = \hat{I}\mathrm{e}^{j\omega t}$, this reverses the sign $Z_\mathrm{i}(\omega)$.

In Fig. 66 the Green functions and impedances are shown for two resonators of different quality factors.

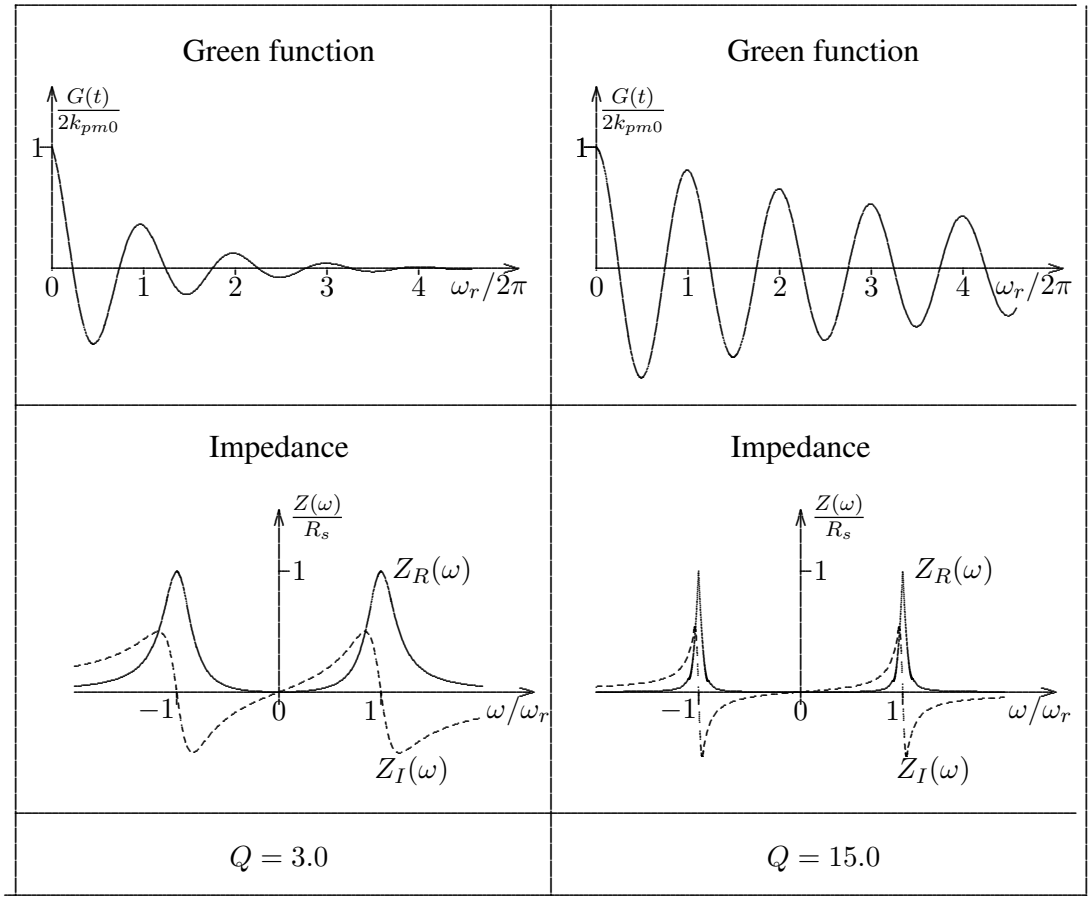

Fig. 66: Green function and impedance of a resonance

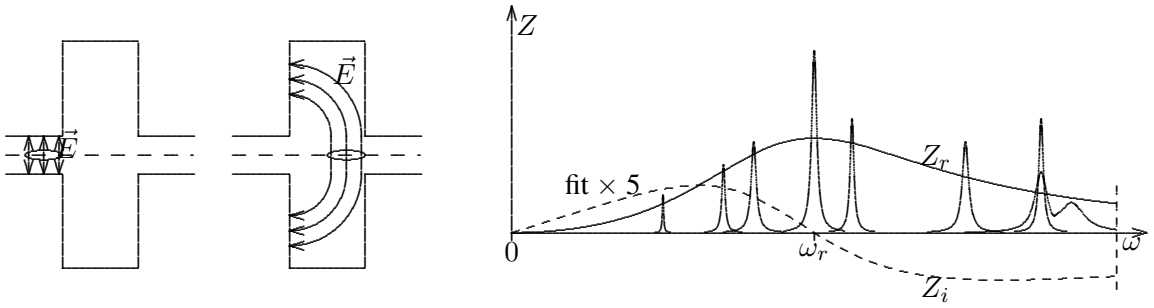

Fig. 67: Aperture changes and typical ring impedance

6.2.4 Typical ring impedance

A ring may have many aperture changes which can form cavity-like objects as shown in Fig. 67 in exaggerated form. They have many resonances, each being approximated by an RLC resonator having a resonant frequency ω_{ri}, shunt impedance R_{si}, and quality factor Q_i. We develop their impedances $Z_i(\omega)$ for small frequencies $\omega < \omega_\mathrm{r}$, where it is inductive

$$Z(\omega) = R_{si}\frac{1 - jQ\frac{\omega^2-\omega_\mathrm{r}^2}{\omega\omega_\mathrm{r}}}{1 + \left(Q\frac{\omega^2-\omega_\mathrm{r}^2}{\omega\omega_\mathrm{r}}\right)^2} \approx j\frac{R_{si}\omega}{Q\omega_\mathrm{r}} + \dots \ .$$

Summing over all aperture changes and their resonances we get the inductance L of a ring at low frequencies $\omega \ll \omega_{ri}$. It turns out that its impedance divided by the mode number $n = \omega/\omega_0$ is a useful

parameter which gives a good description of the ring impedance at low frequencies:

$$\left|\frac{Z}{n}\right|_0 = \sum_k \frac{R_{sk}\omega_0}{Q_k\omega_{rk}} = L\omega_0 = L\frac{\beta c}{R} .$$

It depends on impedance per length and is therefore to some extent independent of the ring size. Older machines, built before about 1975, have typical values $|Z/n| \approx 10\ \Omega$ mainly due to many aperture changes. Once the importance of this was realized, vacuum chambers became much smoother resulting in $|Z/n| \approx 1\ \Omega$ in newer rings.

We can make some estimates for the impedance at higher frequencies. The number of so-called parasitic resonances with shunt impedance R_{sk} increases up to the cut-off frequency (1) where wave propagation in the vacuum chamber becomes possible and the fields are no longer contained in a cavity-like object. At approximately this point the impedance reaches a maximum above which it decreases, Fig. 67.

Sometimes one averages over the many resonances and makes a broad band resonator fit. This is useful to estimate the resistive impedance from some knowledge of the reactive part or to estimate single traversal effects like energy loss or bunch lengthening. However, for multi-traversal instabilities the many narrow resonances are important to provide a memory of induced fields over one revolution and averaging over them would be wrong.

6.2.5 Review of the longitudinal dynamics

In an earlier section we treated the longitudinal focusing by the RF system shown in Fig. 47 in the presence of an energy loss U_s which depends itself on the particle energy

$$U_s = U_{s0} + \frac{\partial U_s}{\partial E}\Delta E .$$

We used the nominal synchrotron frequency ω_{s0} and the damping parameter α_d,

$$\omega_{s0} = \omega_0\sqrt{\frac{\eta_c h e\hat{V}\cos\phi_s}{2\pi\beta^2 E_0}} , \quad \alpha_d = \frac{\omega_0}{4\pi}\frac{\partial U_s}{\partial E}$$

and obtained the solutions

$$\tau = \hat{\tau}\mathrm{e}^{-\alpha_d t}\sin(\omega_s t) , \quad \epsilon = \hat{\epsilon}\mathrm{e}^{-\alpha_d t}\cos(\omega_s t) , \quad \omega_s = \omega_s 0\sqrt{1-\alpha_d^2/\omega_{s0}^2} \approx \omega_{s0} .$$

For the synchrotron oscillation to be damped we need

$$\alpha_d = \frac{1}{2}\frac{\omega_0\eta}{2\pi}\frac{\partial U_s}{\partial E} > 0 .$$

It is self-evident that a loss which increases with energy has a stabilizing effect. In the following we concentrate on a loss U_s created by the interaction between the beam and the impedance of the surroundings.

6.3 Induced voltage and energy loss of a stationary bunch

We consider a circulating bunch of N_b particles with a periodic symmetric current $I_k(t)$ in time domain or as a Fourier series, as shown in Fig. 68:

$$I_k(t) = \sum_{k=-\infty}^{\infty} I(t-kT_0) = I(t) = I_0 + 2\sum I_p\cos(p\omega_0 t) , \quad I_p = \frac{1}{T_0}\int_0^{T_0} I(t)\cos(p\omega_0 t)\mathrm{d}t . \quad (15)$$

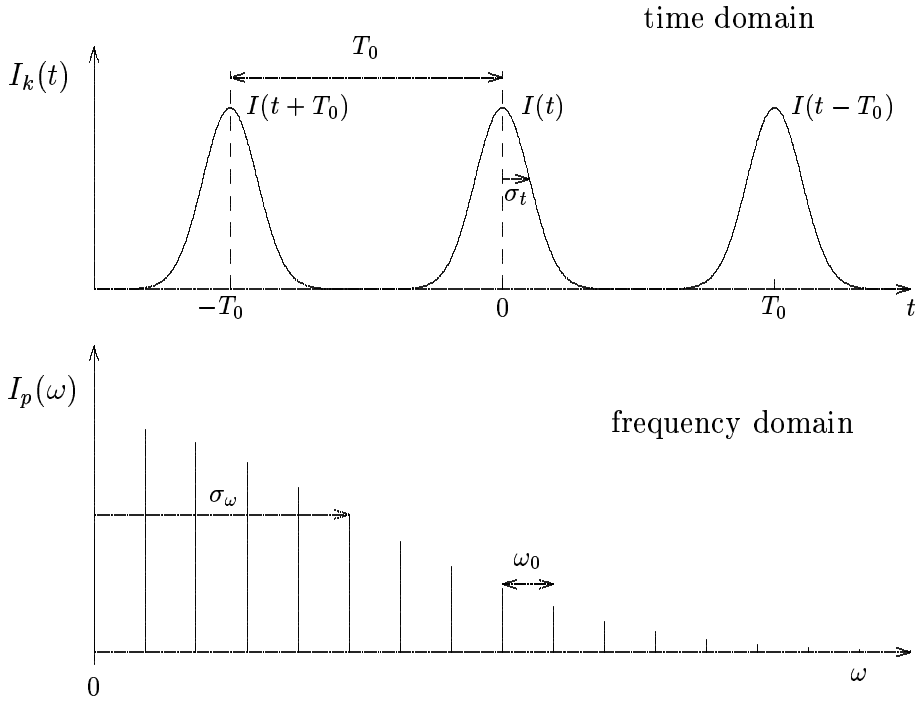

Fig. 68: Circulating single bunch in time and frequency domain

In the impedance $Z(\omega)$ it induces voltage

$$V(t) = \sum_{p=1}^{\infty} I_p \left[Z_{\rm r}(p\omega_0) \cos(p\omega_0 t) - Z_{\rm i}(p\omega_0) \sin(p\omega_0 t) \right]$$

leading to an energy loss per particle and turn

$$U_s = \frac{1}{N_b} \int_0^{T_0} I(t) V(t) {\rm d}t = \frac{2T_0}{N_b} \sum_1^{\infty} I_p^2 Z_{\rm r}(p\omega_0) = \frac{2e}{I_0} \sum_1^{\infty} I_p^2 Z_{\rm r}(p\omega_0)$$

where we used the orthogonality properties of trigonometric functions

$$\int_0^{T_0} \cos(p'\omega_0 t) \sin(p\omega_0 t) {\rm d}t = 0, \;\; I_0 = eN_b/T_0$$
$$\int_0^{T_0} \cos(p'\omega_0 t) \cos(p\omega_0 t) {\rm d}t = \begin{cases} T_0/2 & \text{for } p' = p \\ 0 & \text{for } p' \neq p \end{cases} .$$

The energy loss is only due to the resistive impedance. It is expressed by a sum. For large machines with small revolution frequencies the spacing of the harmonics $p\omega_0$ can be small compared to a typical width of parasitic resonances and the sum may be replaced by an integral

$$U_s = \frac{2T_0}{N_b} \sum_1^{\infty} I_p^2 Z_{\rm r}(p\omega_0) \approx \frac{2}{N_b} \int_0^{\infty} |\tilde{I}^2(\omega)| Z_{\rm r}(\omega) {\rm d}\omega \, .$$

The energy loss of the bunch is a convolution between the power spectrum of the bunch current and the resistive impedance of the ring as illustrated in Fig. 69. It is compensated by the RF system through the synchronous phase angle giving at the bunch centre a voltage per turn $e\hat{V} \sin\phi_s = U_{s0}$.

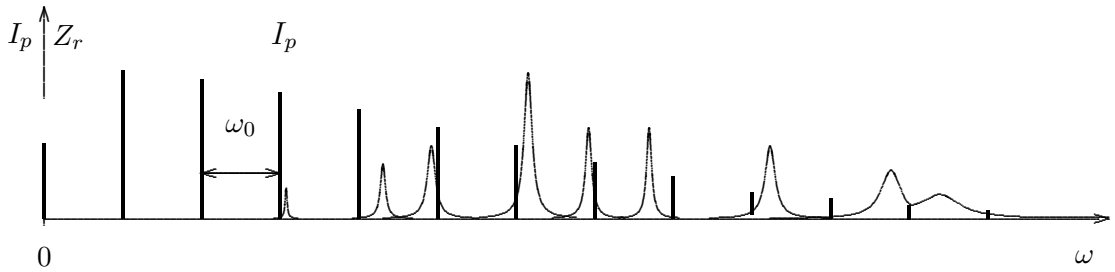

Fig. 69: Convolution of power spectrum of the bunch current and resistive impedance gives energy loss

The loss can be calculated from the known voltage amplitude $\hat{V}$ and the measured phase ϕ_s. Since it is difficult to know the delays occurring in the cables connecting this measurement with the RF cavity and bunch monitors, it is better to determine only the change of synchronous phase with current [21], as in the example experiment shown in Fig. 70 taken at the SLAC damping ring [22].

Measurement errors can occur from warming up of the signal cables at higher bunch intensities leading to a current-dependent delay. Furthermore, in systems with many cavities it is difficult to know the relevant phase. A method developed at DESY [23] avoids this by comparing the distance between two adjacent bunches as a function of the current in the second.

Measuring the energy loss for different bunch lengths helps to get information on the frequency dependence of the impedance, Fig. 71.

6.4 Robinson instability

6.4.1 Qualitative treatment

The interaction of a bunch executing a synchrotron oscillation with a narrow cavity resonance can lead to a growing amplitude, called *Robinson instability* [24]. We shall treat it here in some detail because it can be generalized to describe all multi-turn instabilities in storage rings. In order to gain some understanding of the physics involved, we start with some qualitative treatment and give the quantitative result later.

6.4.2 Modulation of the revolution frequency of an oscillating bunch

We consider a single bunch circulating in a storage ring with revolution frequency ω_0. Its harmonic $p\omega_0$ excites a narrow-band cavity with resonance frequency $\omega_\mathrm{r} \approx p\omega_0$ and impedance $Z(\omega)$ of which we consider only the resistive part Z_r as shown in Fig. 72.

The revolution frequency ω_0 of the circulating bunch depends on its relative energy deviation $\Delta E/E = \epsilon$:

$$\frac{\Delta\omega_0}{\omega_0} = -\frac{\eta_c}{\beta^2}\frac{\Delta E}{E} = -\frac{\eta_c}{\beta^2}\epsilon\ .$$

While the bunch is executing a coherent dipole mode oscillation $\epsilon(t) = \hat{\epsilon}\cos(\omega_s t)$ its revolution frequency is modulated. *Above transition* the revolution frequency ω_0 is *small* when the *energy is high* and ω_0 is *large* when the *energy is small*. If the cavity is tuned to a resonant frequency slightly smaller than the revolution frequency harmonic $\omega_\mathrm{r} < p\omega_0$, as shown in Fig. 72 on the left, the bunch sees a higher impedance and *loses more energy* when it has an *energy excess* and *loses less energy* when it has a *lack of energy*. This leads to a *damping* of the oscillation. If $\omega_\mathrm{r} > p\omega_0$ this is reversed, as shown in Fig. 72 on the right, and leads to an *instability*. Below transition energy the dependence of the revolution frequency on energy deviation is reversed, which changes the stability criterion.

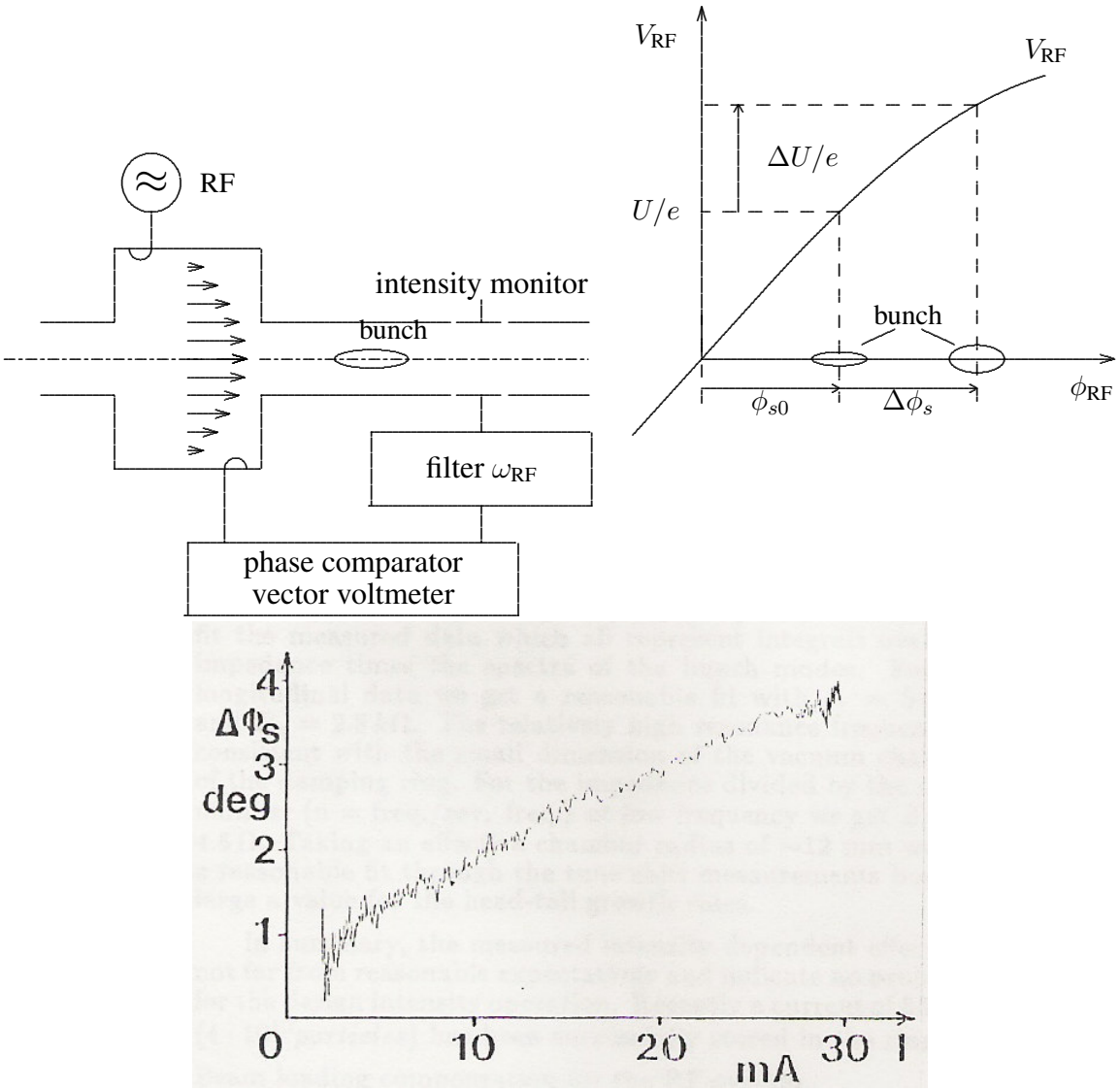

Fig. 70: Measuring energy loss from change of synchronous phase with bunch current

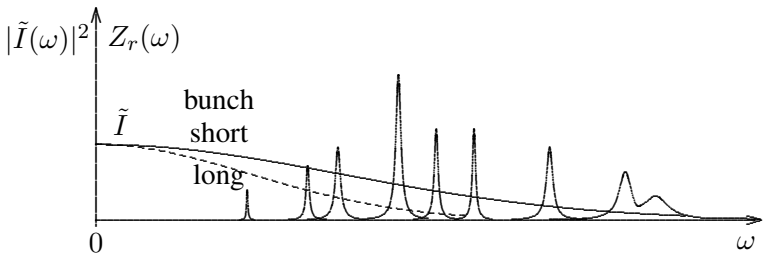

Fig. 71: Frequency dependence of impedance from energy loss for two bunch lengths

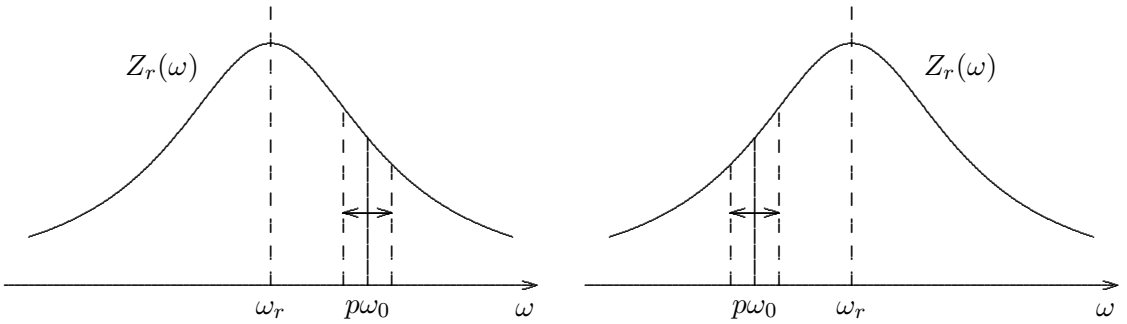

Fig. 72: Qualitative treatment of the Robinson instability

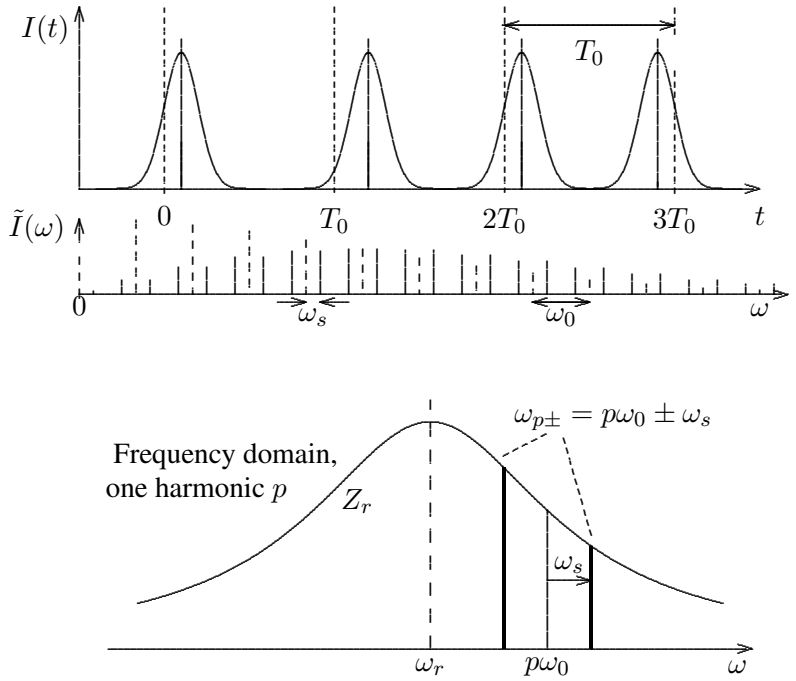

Fig. 73: Oscillating bunch gives a spectrum with sidebands at $\pm\omega_s$ around revolution harmonics $p\omega_0$

6.4.3 Voltage induced by sidebands and stability

The simple picture of energy exchange between the oscillating bunch and the narrow-band impedance and the resulting stability condition illustrates the underlying physics. However, it can not easily be extended to a quantitative treatment. The use of revolution frequency which changes in time represents a mixture of time and frequency domain which is not easily treated by the standard mathematical methods. A bunch executing a synchrotron oscillation is presented in frequency domain by a spectrum consisting of harmonics $p\omega_0$ of the revolution frequency with sidebands spaced by $\pm\omega_s$ around them as shown in Fig. 73.

The oscillating bunch creates frequency components of the current at the carrier $p\omega_0$ with sidebands at $\pm\omega_s$ which excite the cavity resonance. The latter is assumed to be sufficiently narrow such that only one value of p has to be considered. We take as an example a bunch with $Q_s = \omega_s/\omega_0 = 0.25$ and show its oscillation on top of Fig. 74 on two successive turns. This oscillation can be presented as a stationary bunch plus a perturbation. This perturbation induces a voltage in the cavity impedance which will act back on the bunch. It is shown in the centre for $p = 1$ and the frequencies $\omega = (1 \pm Q_s)\omega_0$ corresponding to the upper or lower sideband. After one turn the first one results in a positive field and the lower frequency one in a negative field. At the bottom the bunch motion is presented in the phase-

space coordinates ϵ and τ. Taking the first case $\gamma > \gamma_T$ above transition energy, the bunch has a positive energy deviation after one turn. The field induced by the upper sideband is positive leading to an increase of this energy deviation and therefore to a growing oscillation. The field due to the lower sideband is negative and reduces the energy deviation, leading to damping of the oscillation. Below transition energy $\gamma < \gamma_T$ the bunch rotates in phase-space in the opposite direction which reverses the stability condition. Obviously the special value $Q_s = 0.25$ was chosen to make the stability situation visible after one turn. For a more realistic smaller value for Q_s the oscillation would have to be followed over several turns making the picture more complicated.

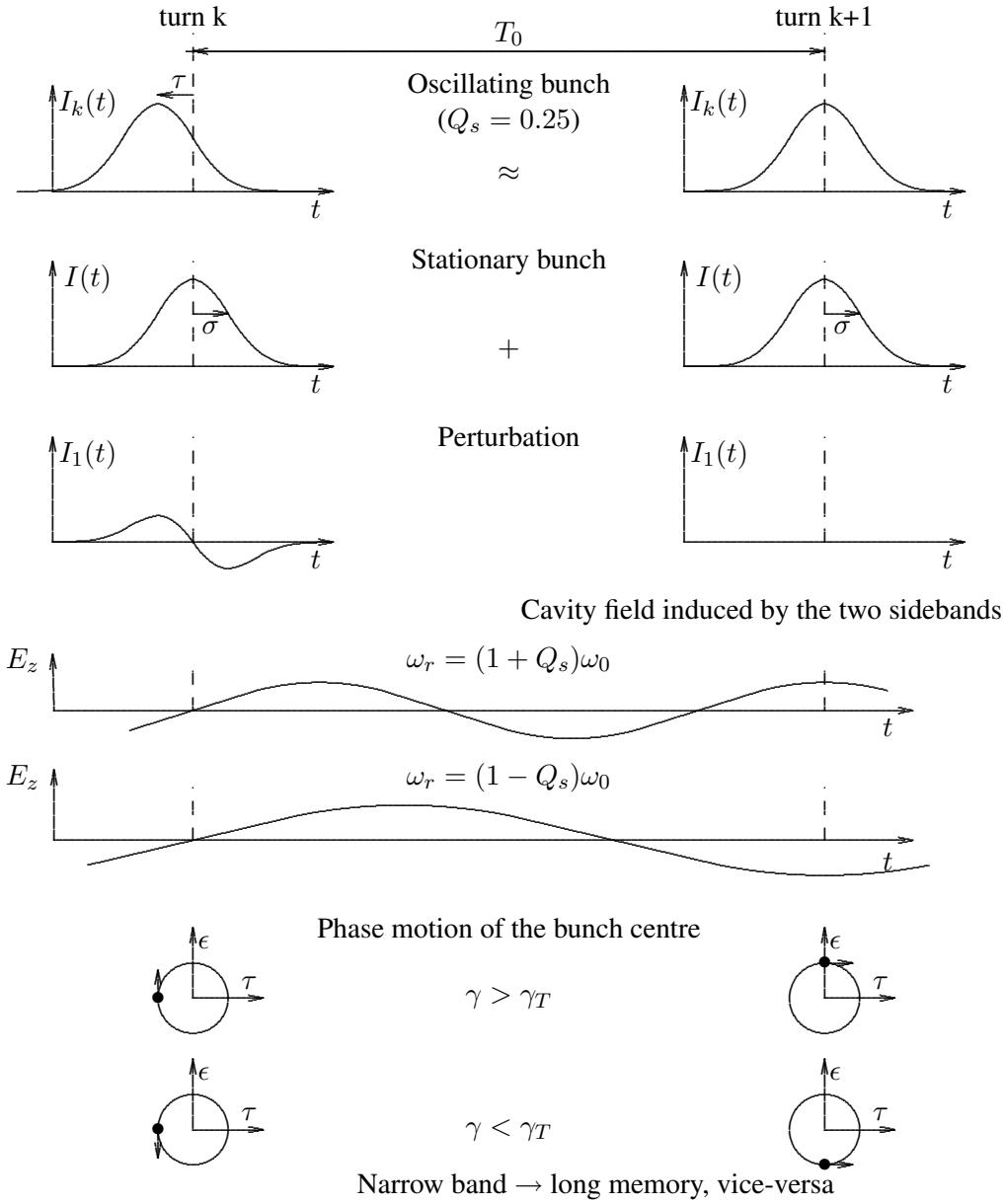

Fig. 74: Effects of the voltages induced by an oscillating bunch at the two sidebands

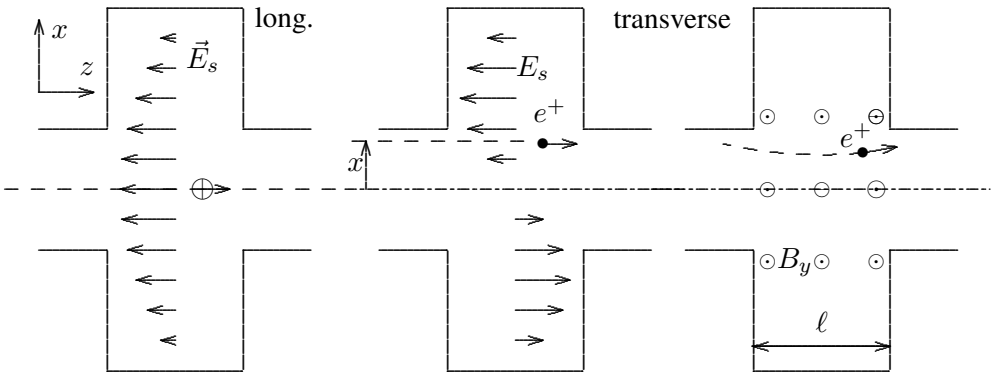

Fig. 75: Longitudinal and transverse impedance

6.4.4 Quantitative expressions for damping rates

Going through the calculation of the induced fields and their effects on the bunch we find an expression for a damped, or growing oscillation of the form

$$\begin{aligned}\epsilon &= \hat{\epsilon}\mathrm{e}^{-a_d t}\cos(\omega_s t),\\ a_d &= \frac{\omega_{s0} p I_p^2 (Z_\mathrm{r}(\omega_{p+}) - Z_\mathrm{r}(\omega_{p-}))}{2 I_0 h \hat{V}\cos\phi_s}\\ \omega_{p\pm} &= \omega_0(p \pm q)\ .\end{aligned}$$

Above transition energy $\gamma > \gamma_T$ and $\cos\phi_s < 0$ we have stability if $Z_\mathrm{r}(\omega_{p-}) > Z_\mathrm{r}(\omega_{p+})$ and vice versa. The damping rate is proportional to the impedance difference at the two sidebands.

One narrow impedance in each ring is the RF cavity which is tuned close to the harmonic number $h\omega_0$, where the current component of the bunch is, according to (15), about equal to the DC value $I_h \approx I_0$ which gives for the damping rate divided by the synchrotron frequency

$$\frac{a_d}{\omega_{s0}} \approx \frac{I_0 (Z_a r(\omega_{p+}) - Z_\mathrm{r}(\omega_{p-}))}{2\hat{V}}\ .$$

It is interesting to note that this ratio is about equal to the beam-induced voltage divided by the applied RF voltage.

In general we have many resonances which can be narrow or broad. To get the growth or damping rate that they create we have to sum over all of them:

$$\frac{a_d}{\omega_{s0}} = \sum_p \frac{p I_p^2 (Z_\mathrm{r}(\omega_{p+}) - Z_\mathrm{r}(\omega_{p-}))}{2 I_0 h \hat{V}\cos\phi_s}\ .$$

6.5 Transverse instabilities

6.5.1 Transverse impedance

Transverse instabilities treat cases in which the effects of the wall can lead to a growing betatron oscillation. While for the longitudinal case we had a simple concept of the wake potential or the impedance in which we found some longitudinal forces induced by the beam current, for the transverse case we seek a similar concept in which we get a transverse force. However, here this force is not induced by the transverse velocity of the particle but by the transverse displacement of the beam current which represents a dipole moment.

This is best explained by some cavity modes shown in Fig. 75. On the left there is the cavity mode we always used for RF acceleration or for longitudinal instabilities and which gives a longitudinal

impedance. A bunch with current I traverses the centre of the cavity and induces a longitudinal field E_z which is approximately homogeneous close to the axis. Its potential is proportional to the bunch current with the longitudinal impedance being the proportionality factor

$$V = -\int E_z \mathrm{d}z = IZ_\mathrm{L} \; .$$

The right side of the figure shows a different oscillation mode in which a bunch current traverses the cavity with a transverse displacement x representing a dipole moment $D = Ix = \hat{D}\cos(\omega t)$, which we assume to have a harmonic time dependence, and induces a longitudinal field, proportional to D through the so far unknown factor k, with a transverse gradient

$$\frac{\partial E_z}{\partial x} = -kIx, \; E_z(x) = -kIx^2 \; .$$

This mode also has a longitudinal impedance which is a function of x

$$Z_\mathrm{L}(x) = -\int E_z \mathrm{d}z/I = -E_z\ell/I = k\ell x^2 \; .$$

Applying Maxwell's equation

$$\dot{\vec{B}} = -\operatorname{curl}\vec{E} \; , \quad \int \dot{\vec{B}}\mathrm{d}\vec{a} = -\oint \vec{E}\mathrm{d}\vec{s}$$

we find the relations

$$\begin{aligned}
\dot{B}_y x\ell = E_z\ell &= -k\ell Dx = -k\ell x\hat{D}\cos(\omega t) \\
\dot{B}_y &= -k\hat{D}\cos(\omega t) \\
B &= -k\hat{D}\sin(\omega t)/\omega \\
\hat{B}_y &= -k\hat{D}/\omega \\
\hat{F} &= -ec\hat{B}_y, \text{ (Lorentz force)} \; .
\end{aligned}$$

We define the transverse impedance

$$Z_\mathrm{T} = -\frac{F_x\ell}{e\hat{D}} = \frac{ck\ell}{\omega} = \frac{cZ_\mathrm{L}}{x^2\omega} = \frac{c}{2\omega}\frac{\mathrm{d}^2 Z_\mathrm{L}}{\mathrm{d}x^2}, \text{ with unit } \left[\frac{\Omega}{\mathrm{m}}\right] \; .$$

We used a special mode to define the transverse impedance and its relation to the second derivative of the longitudinal one of the same mode. In general we have the impedances

longitudinal: integrated longitudinal field/current
transverse: integrated deflection field/dipole moment.

On resonance, E_z is in phase, B_y out of phase with respect to D. We give the general definition for the transverse impedance, using $x = \hat{x}\mathrm{e}^{j\omega t}$

$$Z_\mathrm{T}(\omega) = j\frac{\int \left(\vec{E}(\omega) + [\vec{v}\times\vec{B}(\omega)]\right)_T \mathrm{d}s}{Ix(\omega)} \; .$$

Before, we compared the longitudinal and transverse impedances Z_L and Z_T of the same deflecting mode and found that $Z_\mathrm{T} \propto d^2 Z_\mathrm{L}/dx^2$. This does not have much practical interest but is interesting for

the understanding and the scaling of the two. Instead of concentrating on the same mode it is useful to compare different longitudinal and transverse modes and take some average which gives a semi-empirical relation [25] for a machine with ring radius R and circular vacuum chamber of radius b:

$$Z_{\mathrm{T}}(\omega) \approx \frac{2R}{b^2}\frac{Z_{\mathrm{L}}(\omega)}{\omega/\omega_0} \; .$$

It is interesting to note that the dependence on frequency and radii is different for the two. This relation is often useful to estimate the transverse impedance if the longitudinal one is known or vice versa. From the area available for the induced current in the chamber wall we expect $Z_{\mathrm{L}} \propto 1/b$, and therefore $Z_{\mathrm{T}} \propto 1/b^3$.

6.5.2 Transverse instability of a single rigid bunch, $Q' = 0$

We can understand the physics underlying a transverse instability with the help of Fig. 76. At $t = 0$ a bunch P traverses a transverse impedance (cavity) with an off-set x, excites a field $-E_z$ which converts after $T_r/4$ into a field $-B_y$, then into E_z, and finally into B_y. The magnetic field B_y applies a transverse Lorentz force to the particle. The bunch oscillates with tune Q_x, of fractional part $q_x = 1/4$, seen as sidebands at $\omega_0(p \pm q)$.

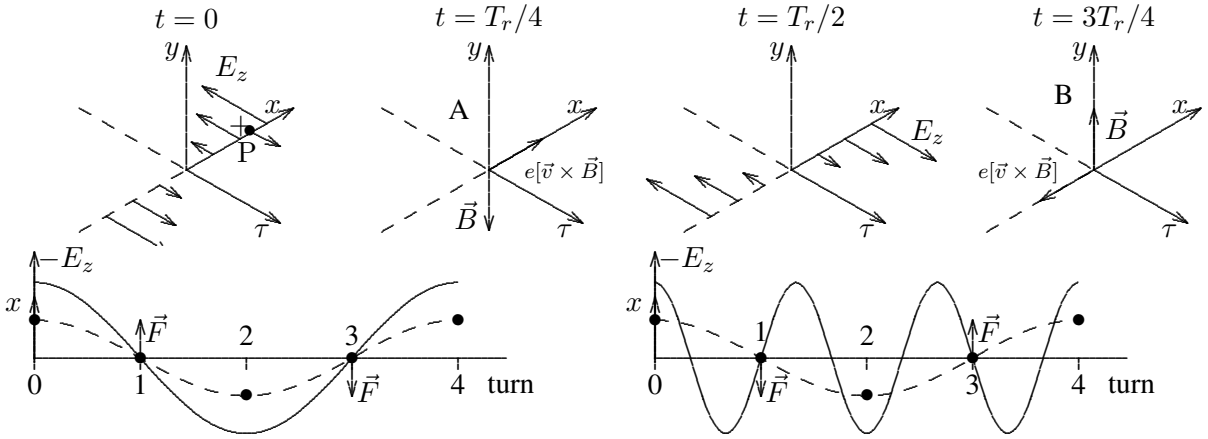

A) Cavity is tuned to the upper sideband:
A bunch traverses it and excites an electric field, in the second turn, at $t = T_r/4$ and situation 'A', this is converted into a magnetic field B_y with Lorentz force in the $+x$ direction and the particle velocity in the opposite, $-x$ direction, this damps the oscillation.

B) Cavity is tuned to the lower sideband:
A bunch traverses it and excites an electric field, in the second turn, at $t = 3T_r/4$ and situation 'B', this is converted into a magnetic field B_y with Lorentz force in the $-x$ direction and the particle velocity in the same, $-x$ direction, this excites the oscillation giving an instability.

Fig. 76: Excitation of a field in a transverse impedance by a dipole moment and its conversion into a deflecting force

A detailed calculation gives the damping rate for the frequencies $\omega_{p\pm} = \omega_0(p \pm q)$

$$x = \hat{x}\mathrm{e}^{-a_d t}\cos(\omega_{p\pm}t) \; , \quad a_d = \frac{e\omega_0\beta_x}{4\pi m_0 c^2 \gamma I_0}\sum_{\omega>0}\left(I_{p+}^2 Z_{Tr}(\omega_{p+}) - I_{p-}^2 Z_{Tr}(\omega_{p-})\right) \; . \qquad (16)$$

6.5.3 Transverse instability of several rigid bunches

A beam with M bunches can oscillate in M independent modes $n = M\Delta\phi/2\pi$ with the phase $\Delta\phi$ between their oscillations as seen simultaneously in a global view, shown in Fig. 77 for four bunches. Seen in a local view by a fixed position monitor, the bunches pass with increasing time delay shown

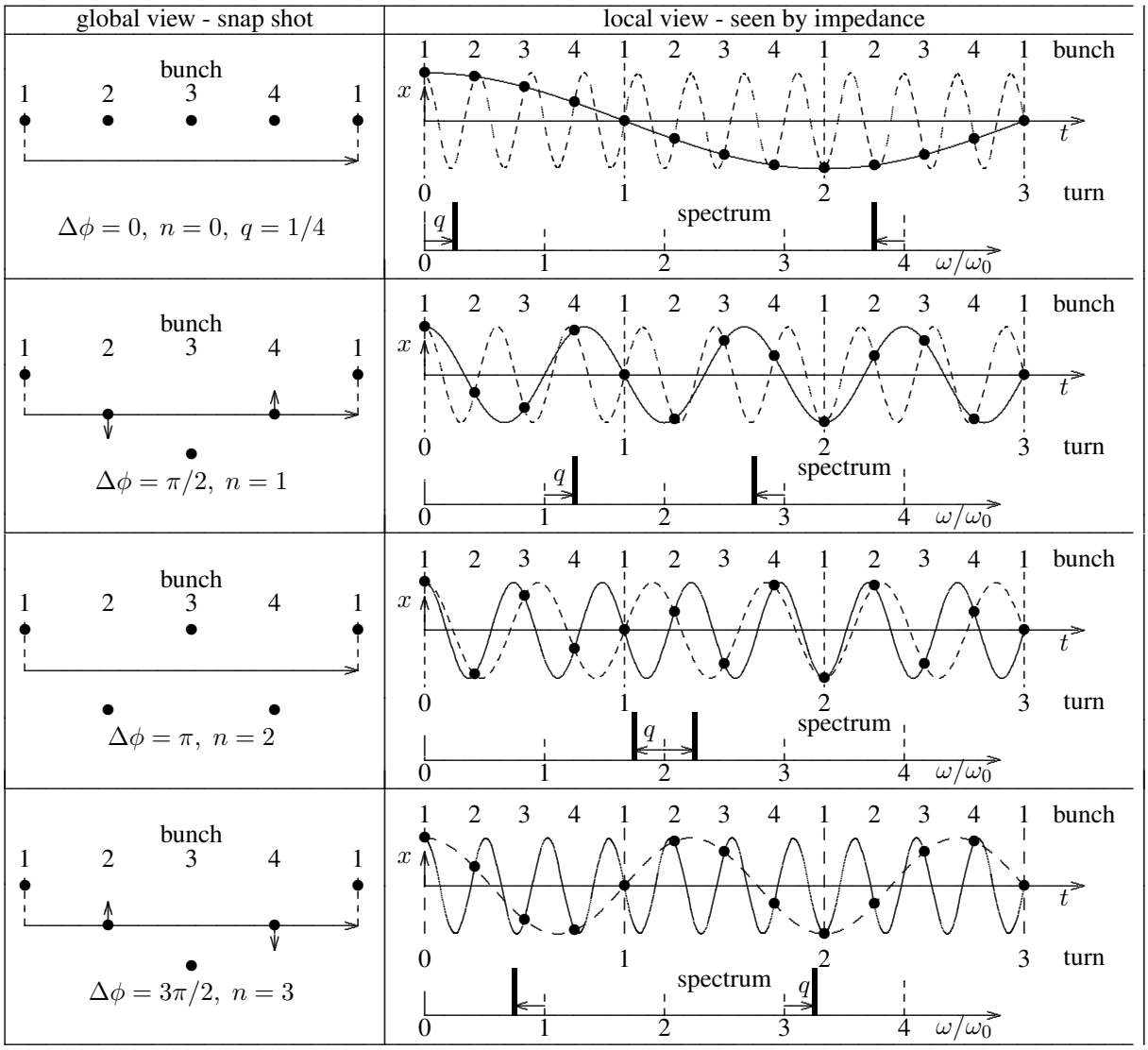

Fig. 77: Modes of oscillation for four bunches

in the figure as bullets being fitted by the upper (solid) and lower (dashed) sideband frequency. Higher frequencies can be fitted as well and the spectrum repeats every $M\omega_0$

$$\omega_{p\pm} = \omega_0(pM \pm (n + q)).$$

Substituting these frequencies in (16) gives the damping rates of each coupled mode n.

The same picture can be applied to longitudinal coupled bunch oscillations by replacing the transverse excursion x by the time or energy excursion τ or ϵ. The stability condition is illustrated in Fig. 78. It is basically the same as for the Robinson instability or the single-bunch transverse case. The damping, or growth rate is proportional to the difference between the impedances at the sidebands corresponding to a particular mode. In the example the mode 3 has a higher impedance at the lower sideband and is unstable.

6.5.4 Non-rigid bunches — head–tail modes, $Q' = 0$

Most position monitors, or relevant impedances, cannot see the transverse beam size given by betatron oscillations. However, the bunch length is within their time resolution and the longitudinal distribution

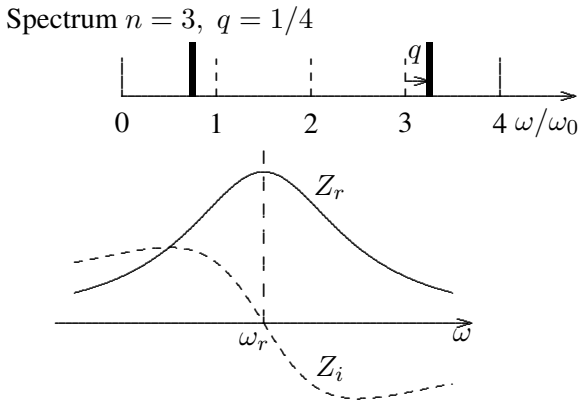

Fig. 78: Stability condition for four bunches

can influence the interaction between the bunch and an impedance. The betatron oscillations of the bunch head and tail can be out of phase with respect to each other. In Fig. 79 a particle distribution in longitudinal phase-space $\psi(\tau,\, \epsilon)$ is shown which rotates with ω_s around a vertical axis. It cannot be observed directly but its projection $\lambda(\tau) = \int \psi(\tau,\, \epsilon)\mathrm{d}\epsilon$ can be seen by an intensity monitor.

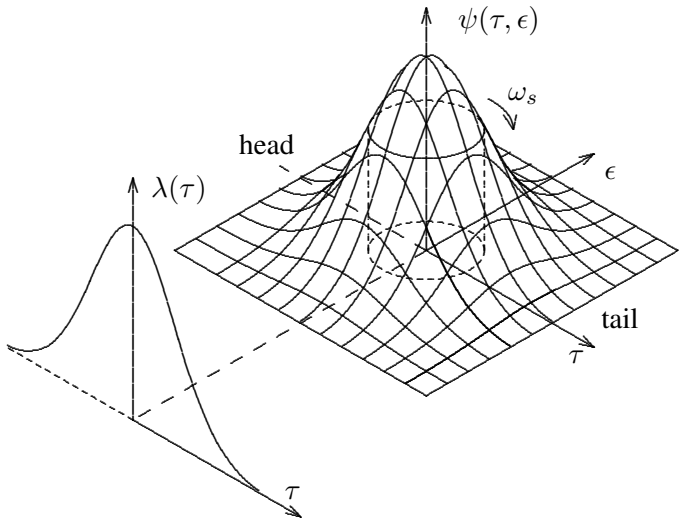

Fig. 79: Longitudinal phase-space distribution

We select a set of particles with a fixed synchrotron oscillation amplitude, lying on the dashed circle, and show them in Fig. 80 as a function of τ, $\epsilon = \Delta E/E$, and vertical betatron position y. The left shows the mode $m = 0$ where all particles oscillate in phase while for the mode $m = 1$ on the right, head and tail oscillate with opposite phase. So far we assumed that the chromaticity vanishes $Q' = \mathrm{d}Q/\mathrm{d}\epsilon = 0$ and the betatron frequency is independent of the excursion ΔE and does not change during a synchrotron oscillation.

6.5.5 Head–tail mode $m = 0$ for $Q' \neq 0$

For a finite chromaticity $Q' = dQ/(dp/p) \neq 0$ the synchrotron oscillation in ΔE affects the transverse motion. For $\gamma > \gamma_T$ a particle has excess energy moving from head to tail and a lack going from tail to head. For $Q' > 0$, the phase advances in the first, lags in the second step and vice versa for $Q' < 0$ or $\gamma < \gamma_T$. In Fig. 81 the particle motion is shown for $T_\beta = T_s/8,\ Q' = 0$, and $Q' < 0$ in four steps of $T_\beta/8$.

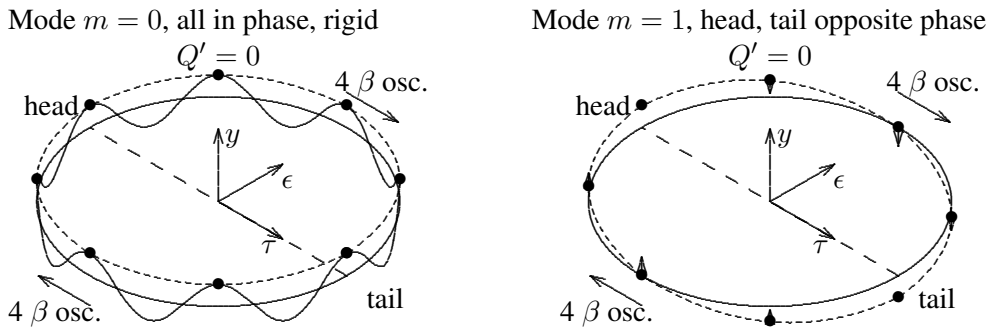

Fig. 80: Simultaneous synchrotron oscillation in τ, ϵ, and betatron oscillation in y

6.5.6 Head–tail instability

The head–tail represents a combined oscillation in synchrotron and betatron space. In the presence of a transverse impedance this can lead to an instability which we explain in a qualitative way with Fig. 82. We replace the bunch by two particles • and ∘ which move between head and tail by a synchrotron oscillation. We also introduce a transverse impedance which is excited by the dipole moment of the displaced particle at the head. It creates a force which increases with distance as in Fig. 76 and applies a transverse force at the tail as shown at the bottom of the figure.

Synchrotron oscillation: The particle being early at the head has the nominal energy but sees, according to Fig. 47, a large voltage, and gains at first energy resulting in a longer revolution time T_0 which moves it towards the later tail. In the second part it will see a smaller RF voltage resulting in the nominal energy at the arrival at the tail at the time $T_s/2$. Afterwards the energy loss dominates resulting in a shorter revolution time catching up the delay and arriving at the early head after a full synchrotron oscillation T_s with nominal energy.

Betatron oscillation: In parallel with the synchrotron oscillation the particles execute a vertical betatron oscillation as shown on top of Fig. 81. This transverse motion is shown in Fig. 82 in phase-space $(y,\, \dot{y})$ for the particle at the head and the particle at the tail. To keep the figure simple we assume a nominal betatron frequency being an even multiple n of the synchrotron frequency. We start with $Q' = 0$ and a pure displacement $(y,\, 0)$ for the particle • resulting with the same transverse coordinates at the tail after time $T_s/2$ and $n/2$ betatron oscillation.

The case of a negative chromaticity is shown on the top half of Fig. 82 where the betatron frequency is reduced during the first half of the synchrotron oscillation making the particle arrive at the tail with a lag in betatron phase resulting in a positive velocity $\dot{y} > 0$. The deflecting force of the impedance is also positive and increases the particle velocity, resulting in an instability. During the return towards the head, the particle • has a lower energy and higher betatron frequency, catches up in betatron phase, and arrives at the head with the original displacement $(y,\, 0)$. During this whole cycle the motion of the other particle ∘ has the opposite synchrotron phase.

The lower half of the figure gives the situation for a positive chromaticity. Here, the particle at the tail has a negative velocity $\dot{z}$ which gets diminished by a positive force resulting in stability.

Below transition energy the synchrotron motion rotates in phase-space in the opposite direction, this reverses the stability conditions.

This qualitative discussion of the head–tail instability contains many assumptions: integer number of betatron oscillation during a synchrotron period, having just two particles, considering the effect of the force only at the tail and not during the whole motion and others. However, it can give the basic physics and the importance of the betatron phase shift by the chromaticity during a synchrotron motion.

A quantitative treatment is more complicated but gives an interesting result. A bunch making a head–tail oscillation at finite chromaticity has a wave-like wiggle with frequency ω_ξ as shown in Fig. 81.

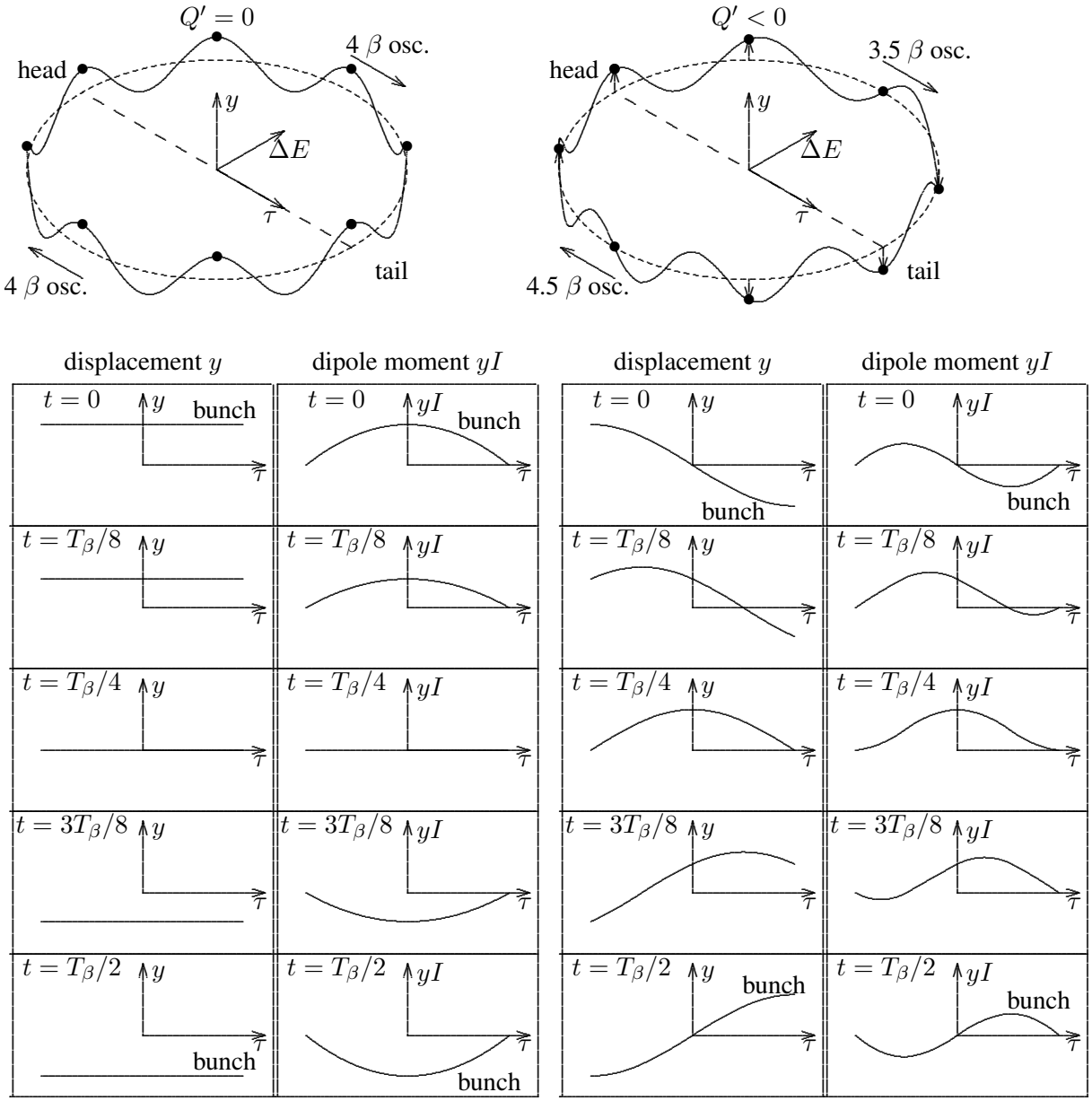

Fig. 81: Head–tail mode $m = 0$ for vanishing and finite chromaticity

This modifies the spectrum by shifting the envelope of the sidebands, shown on top of Fig. 83 with positive and negative frequencies, and on the bottom, converted to positive frequencies only. A bunch oscillating in a head–tail mode still contains the same frequency lines but their envelope is shifted resulting in different sizes of upper and lower sidebands and the current components I_p^+ and I_p^+ they represent [26]. In the Robinson instability the damping rate was given by a difference between impedances $Z_{\rm r}^{\pm}$ times the current components. This is still the case but now the current components are different

$$I_{p\xi\pm} = \frac{\omega_0}{\sqrt{2\pi}} \tilde{I}(\omega_{p\pm} + \omega_\xi) \ , \quad \omega_{p\pm} = \omega_0 \left(p \pm q\right) \ , \quad \frac{\omega_\xi}{\omega_0} = \frac{Q'}{\eta_c}$$

while the impedances can still be about the same. These currents replace the ones in (16) giving for the damping rate of a single bunch

$$a_d = \frac{e\omega_0\beta_x}{4\pi m_0 c^2 \gamma I_0} \sum_{\omega>0} \left(I_{p\xi+}^2 Z_{Tr}(\omega_{p\xi+}) - I_{p\xi-}^2 Z_{Tr}(\omega_{p-}) \right) \ , \quad \omega_{p\pm} = \omega_0(p \pm q) \ . \tag{17}$$

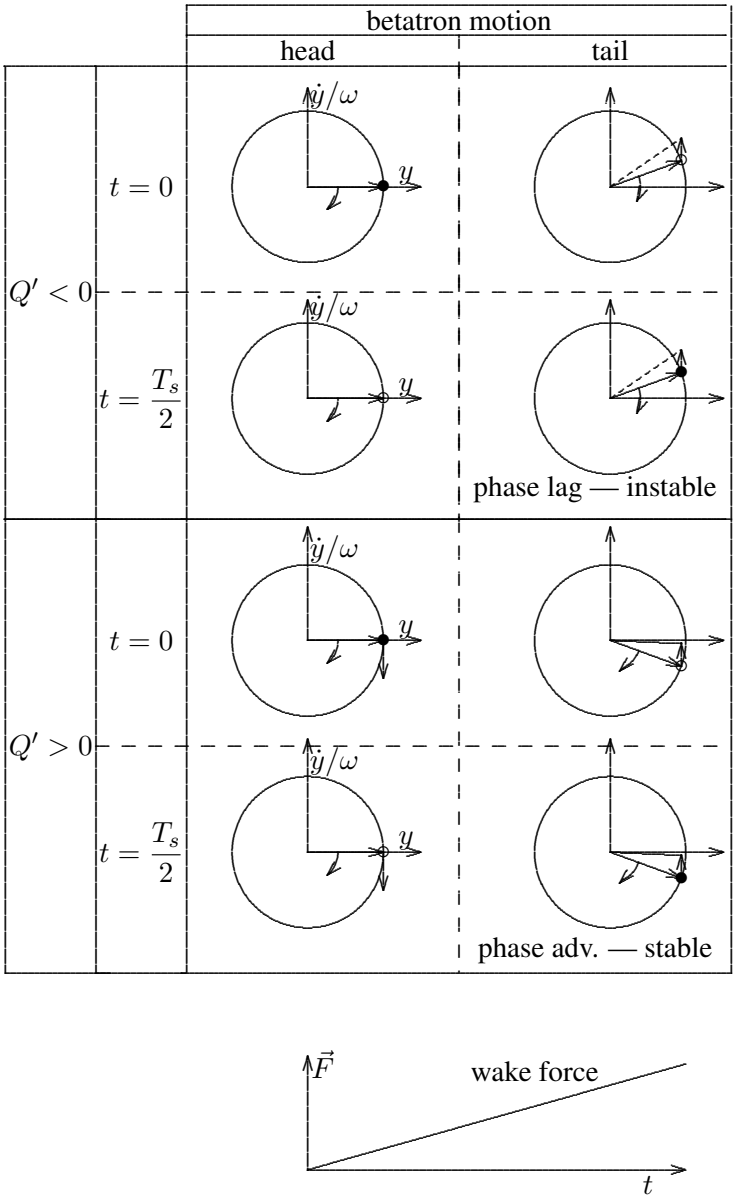

Fig. 82: Mechanism of the head–tail instability

For the head–tail instability we do not need a difference in impedance between the sidebands since we have one in the current components. In other words, instabilities can also get driven by wide-band impedances with little memory over one turn.

6.6 Summary of stability conditions

In Table 3 we summarize the stability conditions for the treated cases. For the head–tail a condition is imposed on the chromaticity while for the multi-turn instabilities the impedance difference $Z_{\rm r}(\omega_{p+}) - Z_{\rm r}(\omega_{p-})$ between the upper and lower sideband is important.

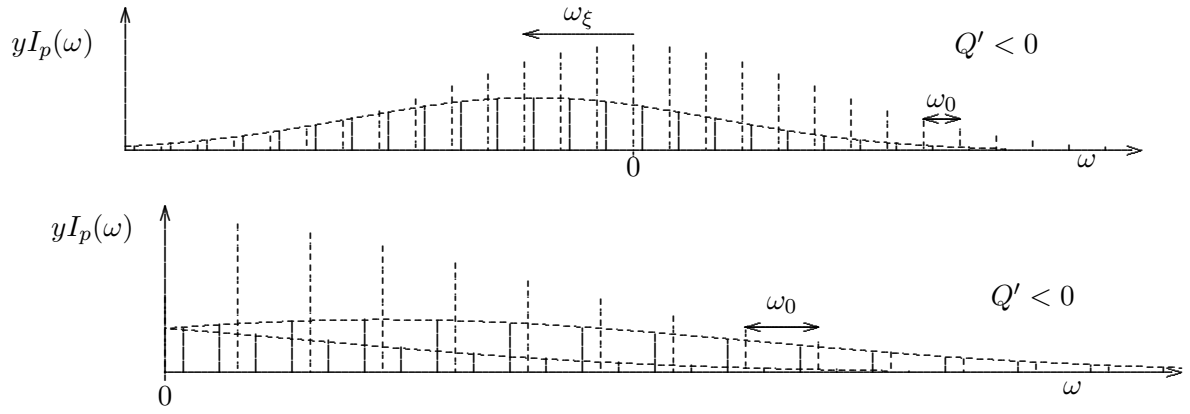

Fig. 83: Head–tail mode spectrum shifted by the chromatic frequency

Table 3: Stability criteria

	above transition	below transition
longitudinal, stability	$Z_{\mathrm{r}}^{+} < Z_{\mathrm{r}}^{-}$	$Z_{\mathrm{r}}^{+} > Z_{\mathrm{r}}^{-}$
transverse $Q' = 0$, stability	$Z_{\mathrm{Tr}}^{+} > Z_{\mathrm{Tr}}^{-}$	$Z_{\mathrm{Tr}}^{+} > Z_{\mathrm{Tr}}^{-}$
transverse head–tail, stability	$Q' > 0$	$Q' < 0$

6.7 Observation of instabilities

6.7.1 Finding the cause of instability

Instabilities are analysed in order to cure them. The first indication of an instability is often a loss of beam or an intensity limitation during accumulation. As a first step one has to find out if a longitudinal or a transverse effect is the cause. This sounds trivial but the occurrence of an oscillation in one plane can obscure the other plane. Carefully approaching the threshold of an instability and observing the oscillations when first visible, can help. Next we like to find out if it is a multi-turn effect; this can be done by changing the bunch spacing.

6.7.2 Analysis of coupled-bunch instabilities

A multi-turn instability is driven by a narrow-band impedance and we like to find its resonant frequency. This situation is made difficult by the fact that the spectrum repeats every multiple of the basic bunch frequency.

For coupled-bunch oscillations it helps to find the mode number n which can narrow down the driving frequency. An example is given in Fig. 84 where longitudinally oscillating bunches are shown on a mountain-range display [27]. On top many oscillations are superimposed on each trace to see the growing amplitude and to determine the growth rate. On the bottom only one turn is taken per trace to compare the oscillation phase and to determine the coupled mode number n.

It is also possible to find this mode number in frequency domain by looking at the spectrum oscillating bunches and determine the position of the sidebands. Such an example is shown in Fig. 85 where the spectrum of a coupled-bunch betatron oscillations was observed with a position monitor. Since the beam was not well centred the revolution harmonics are also visible but some sidebands appear between them.

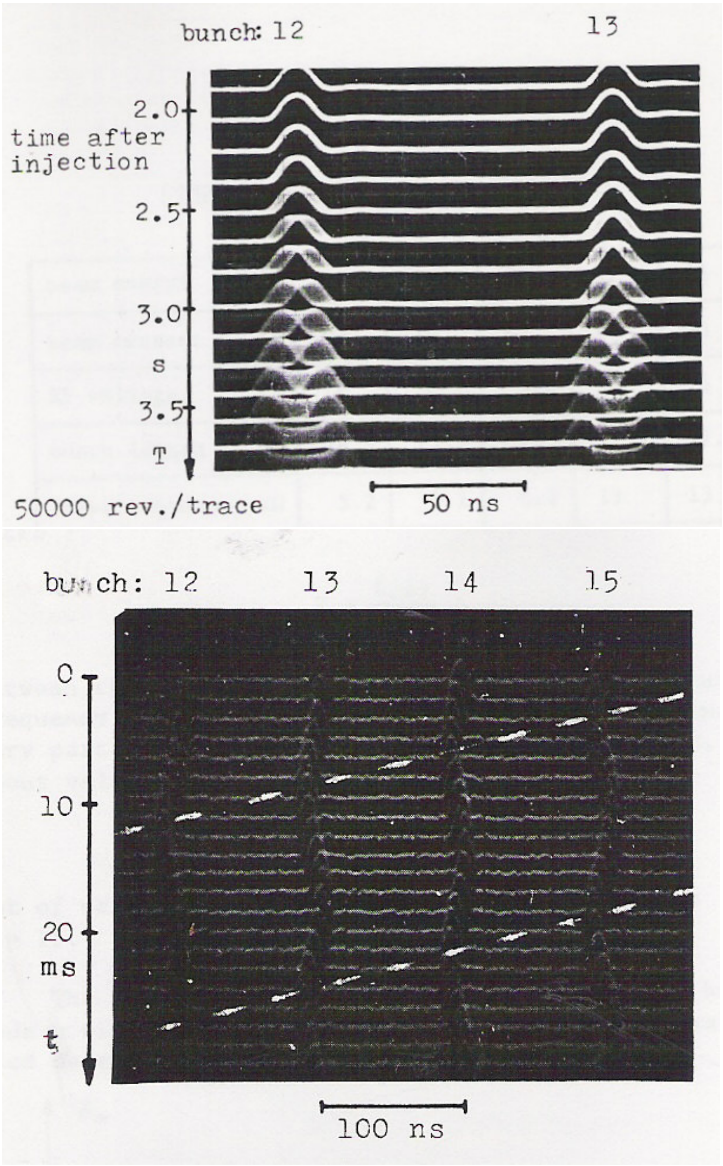

Fig. 84: Longitudinal coupled-bunch oscillation; top: many turns superimposed on each trace gives growth rate; bottom: show oscillation each turn, get phase between bunches

6.7.3 Head–tail mode and instability

The head–tail mode oscillation of relatively long bunches can be observed directly with a fast position monitor. Such a measurement [26] taken for a vanishing and a finite chromaticity at the CERN Booster is shown in Fig. 86. Several traces, corresponding to one turn each, show the instantaneous dipole moment.

In Fig. 87 a complete measurement of a head–tail instability is presented [28]. On the right, two mountain-range displays show bunches during the instability occurrence. The top shows the intensity which is reduced abruptly when the bunch gets lost. On the display at the bottom the growing dipole moment can be see during the instability. Both pictures indicate that it is not a coupled-bunch mode since each bunch oscillates independently at different times. The top picture on the left shows the shift of the envelope spectrum by the chromatic frequency. On the bottom a filtered position monitor signal in a logarithmic display indicates the exponential growth up to the beam loss.

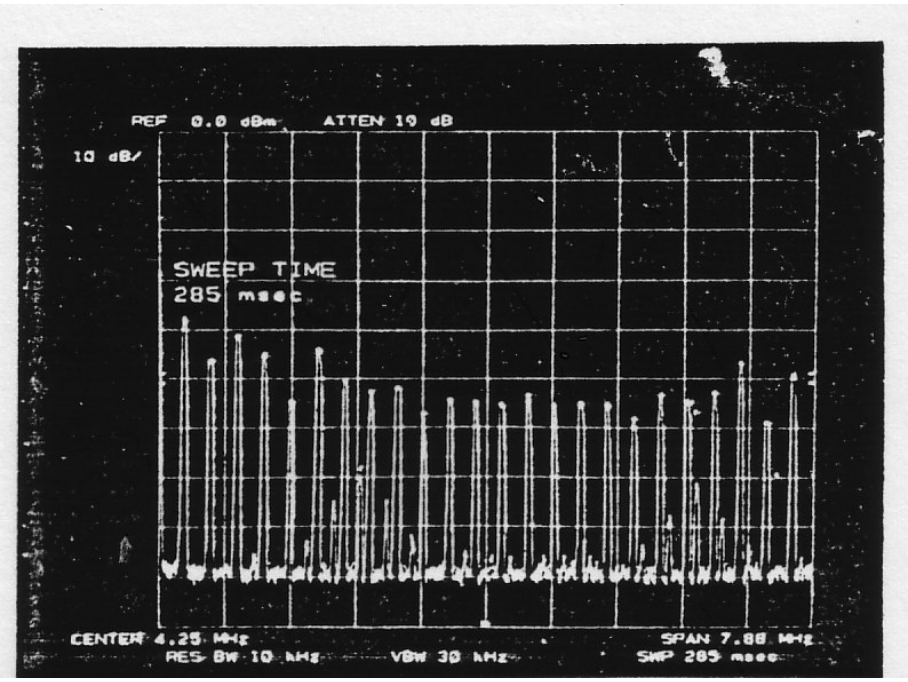

Fig. 85: Spectrum of coupled-bunch betatron oscillation shows selected sidebands between revolution harmonics

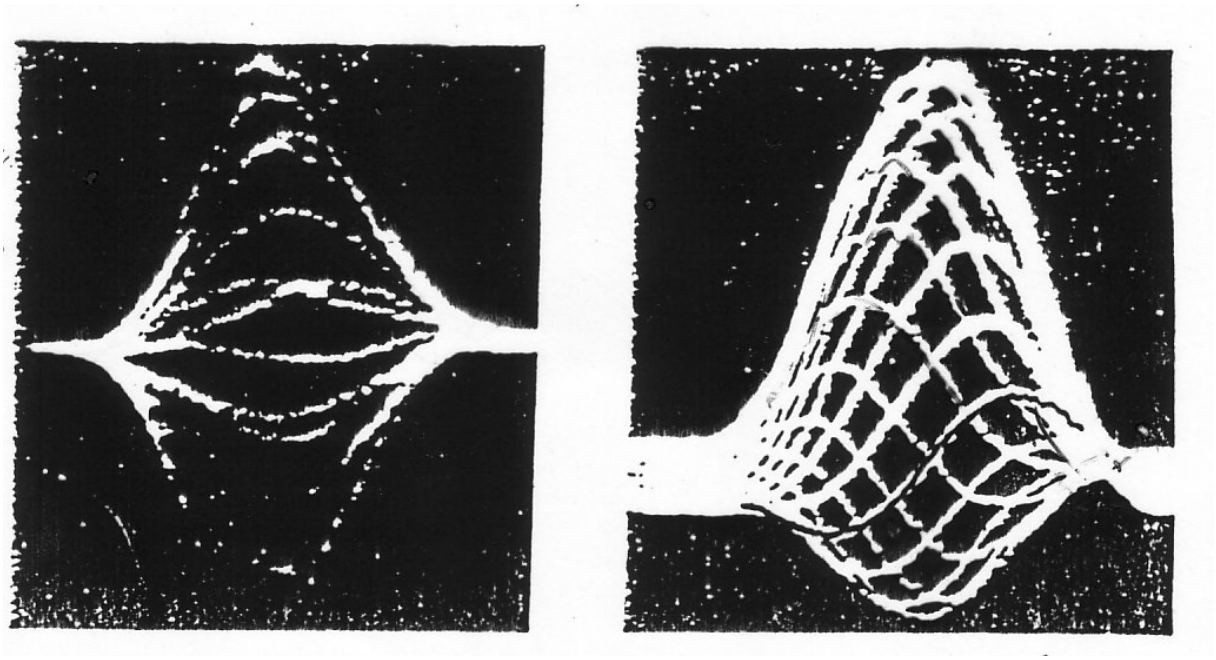

$Q' = 0$ $Q' > 0$

Fig. 86: Head–tail mode $m = 0$ for vanishing (left) and finite (right) chromaticity

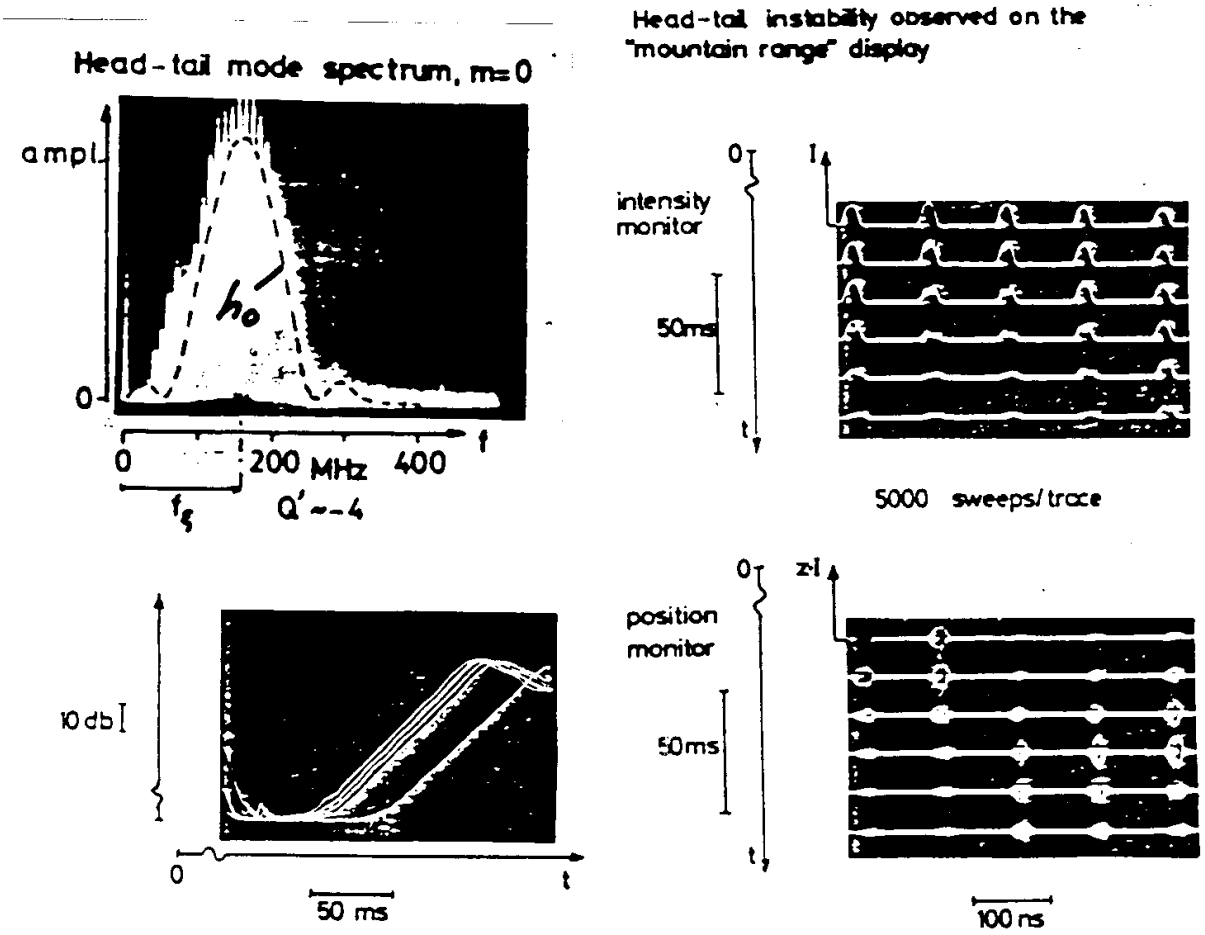

Fig. 87: Observed head–tail instability on a mountain-range display; on the right, a shifted spectrum, on the left an exponential growth of the dipole moment signal displayed on a logarithmic scale

References

[1] E. Durand, Electrostatique, Tome II (Masson, Paris, 1966), p. 207.

[2] A. Tucci, private communication (1981).

[3] B. Zotter, unpublished note (1979).

[4] CAS CERN Accelerator School, Digital Signal Processing, Sigtuna, Sweden, 2007, CERN-2008-003, ed. D. Brandt.

[5] A. Hofmann, Diagnostics with synchrotron radiation, CAS CERN Accelerator School, Synchrotron Radiation and Free Electron Lasers, Brunnen, Switzerland, 2003, CERN-2005-012, ed. D. Brandt.

[6] J. Safranek and M.J. Lee, Calibration of the X-ray ring quadrupoles, BPMs and orbit correctors using the measured orbit response matrix, Workshop on Orbit Correction and Analysis, Upton, NY, USA, 1993, AIP Conf. Proc., Vol. 315, 1994, 128–136.

[7] P.J. Bryant, P. Galbraith, J.P. Gourber, G. Guignard, and K. Takikawa, Measurement of the excitation of the coupling resonance $Q_h - Q_v = 9$, IEEE Trans. Nucl. Sci. NS32 (1977) 1440.

[8] P.L. Morton, J.-L. Pellegrini, T. Raubenheimer, L. Rivkin, M. Ross, R.D. Ruth, and W.L. Spence, A diagnostic for dynamic aperture, IEEE Trans. Nucl. Sci. NS32 (1985) 2291.

[9] A. Burns, P. Castro, G. Morpurgo, and R. Schmidt, Betatron function measurement at LEP using the BOM 1000 turns facility, 1993 IEEE Particle Accelerator Conference, Washington D.C., eds. C.W. Leemann and J.J. Bisognano (IEEE, Piscataway, 1993), p. 2103.

[10] A. Hofmann, Kinetic theory, CAS CERN Accelerator School, Fifth Advanced Accelerator Physics Course, Rhodes, Greece, 1993, CERN 95-06, p. 259, ed. D. Brandt.

[11] D. Neuffer, Longitudinal motion of high current ion beams, IEEE Trans. Nucl. Sci. NS26 (1979) 3031.

[12] A. Hofmann and F. Pedersen, Bunches with local elliptic energy distribution, IEEE Trans. Nucl. Sci. NS26 (1979) 3526.

[13] A. Piwinski, private communication.

[14] A.A. Sokolov and I.M. Ternov, Sov. Phys. Dokl. 8 (1964) 1203.

[15] V.N. Baier and Y.F. Orlov, Sov. Phys. Dokl. 19 (1966) 1145.

[16] A. Müller, private communication

[17] D. Brandt, P. Castro, K. Cornelis, A. Hofmann, G. Morpurgo, G.L Sabbi, and A. Verdier, Measurement of chromatic effects in LEP, 1995 IEEE Particle Accelerator Conference, Dallas, TX, USA (IEEE, Piscataway, 1996), p. 2841.

[18] H. Wiedemann, Particle Accelerator Physics I (Springer, Berlin, 1993), p. 260.

[19] R. Assmann et al., The energy calibration in LEP in the 1993 scan, Z. Phys. C 66 (1995) 567.

[20] B. Zotter and S Kheifets, Impedances and wakes in high-energy particle accelerators, (World Scientific, Singapore, 1997).

[21] M.A. Allen, J.M. Paterson, J.R. Rees, and P.B. Wilson, Beam energy loss to parasitic modes in SPEAR II, IEEE Trans. Nucl. Sci. NS30 (1975) 1838.

[22] L. Rivkin et al., Accelerator physics measurements at the damping ring, IEEE Trans. Nucl. Sci. NS32 (1985) 2626.

[23] R.D. Kohaupt, Single beam instabilities in PETRA, IEEE Trans. Nucl. Sci. NS26 (1979) 3480.

[24] K.W. Robinson, Stability of beam in radio frequency systems, Cambridge Electron Accelerator report, CEAL-1010 (1964).

[25] W. Schnell, CERN Internal Note.

[26] J. Gareyte and F. Sacherer, Head–tail instabilities in the CERN PS and booster, Proc. 9th Int. Conf. on High Energy Accelerators HEACC, 1974, SLAC, Stanford, CA, USA (AEC, Washington D.C., 1974), p. 341.

[27] P. Bramham, S. Hansen, A. Hofmann, K. Hübner, and E. Peschardt, Investigation and cures of longitudinal bunched beam instabilities in the ISR, 9th Int. Conf. on High Energy Accelerators, HEACC, 1974, SLAC, Stanford, CA, USA (AEC, Washington D.C., 1974), p. 339.

[28] A. Hofmann, Diagnostics and cures for beam instabilities, 11th Int. Conf. on High Energy Accelerators, CERN, 1980, ed. W.S. Newman (Experientia, Suppl. 40), p. 540.